TEMPORAL VARIABILITY AND BIO-PHYSICAL COUPLING IN THE PELAGIC FAUNA OF MONTEREY BAY

Samuel Stetson Urmy

A thesis
submitted in partial fulfillment of the
requirements for the degree of

Master of Science

University of Washington

2012

Committee:
John K. Horne
Daniel E. Schindler
Christian E. Torgersen

Program Authorized to Offer Degree:
Aquatic and Fishery Sciences

University of Washington

ABSTRACT

TEMPORAL VARIABILITY AND BIO-PHYSICAL COUPLING IN THE PELAGIC FAUNA OF MONTEREY BAY

Samuel Stetson Urmy

Chair of the Supervisory Committee:
Professor John K. Horne
School of Aquatic and Fishery Sciences

Temporal variability is an important feature of aquatic ecosystems that is often difficult to measure. To this end, a stationary, upward-facing scientific echosounder was used to record the vertical distribution of pelagic fauna in Monterey Bay, California, for 18 months. To characterize these distributions, we developed and tested a suite of metrics quantifying the distribution of biomass in the water column. These metrics recorded a strong seasonal cycle, with total backscatter reaching a minimum during the spring upwelling season and a maximum in the fall and winter. Variability was greatest at long time scales and displayed a power spectrum similar to that of a turbulent fluid, with discrete peaks at 12- and 24-hour periods, corresponding to the semidiurnal tide and diel vertical migration. Pelagic animals also responded to short-term oceanographic variability, moving up in the water column and decreasing in abundance in the days following upwelling events. At longer lags, consistent with reproduction of small zooplankton (38 days), their abundance increased. Primary production appeared to propagate down the water column at rates consistent with sinking marine snow. Animal density throughout the water column was positively correlated at 0-2 day lags with sea level. Active acoustics are a useful addition to ocean observatories, and the metrics presented here provide a useful and objective set of descriptors for stationary acoustic data. Such data provides insight into pelagic ecosystem dynamics unavailable with other sampling methods, and has great potential for future research.

Contents

List of Figures iii

List of Tables v

1 Introduction 1
- 1.1 Temporal variability in the ocean . . . 1
- 1.2 Ocean observatories and stationary acoustics . . . 2
- 1.3 Instrumentation . . . 4
- 1.4 Thesis objectives and organization . . . 6

2 Acoustic Metrics and Temporal Variability of Pelagic Fauna 9
- 2.1 Introduction . . . 9
- 2.2 Methods . . . 10
- 2.3 Results . . . 18
- 2.4 Discussion . . . 26

3 Response of Micronekton to Environmental Variability 31
- 3.1 Introduction . . . 31
- 3.2 Methods . . . 33
- 3.3 Results . . . 37
- 3.4 Discussion . . . 43

4 Summary and Conclusions 51
- 4.1 Summary . . . 51
- 4.2 Significance . . . 52

A Echograms 55

References 72

List of Figures

1.1 Stommel diagram of zooplankton variability 2
1.2 Map of Monterey Bay 5

2.1 Representative echogram with corresponding metrics 14
2.2 Sensitivity of layer-detection algorithm 19
2.3 Sensitivity of metrics to acoustic threshold 21
2.4 Principal component analysis of metric time series 22
2.5 Metric time series for entire deployment 23
2.6 Fourier power spectra of metric time series 25
2.7 Wavelet transforms of the metric time series 27

3.1 Map of Monterey Bay sea-surface temperatures 34
3.2 Oceanographic and acoustic time series 38
3.3 Cross-correlation of oceanographic series 39
3.4 Oceanographic-acoustic cross-correlation 40
3.5 Cross-wavelet analysis of acoustic and environmental series 41
3.6 Cross-correlation of acoustic and environmental series 42
3.7 Depth-dependent cross-wavelet coherence 44

List of Tables

2.1 Metric quantities and formulas 13
2.2 Summary of seasonal models 24

3.1 Epipelagic backscatter model 43

ACKNOWLEDGEMENTS

This thesis would not have been possible without support from a number of sources and people. Kongsberg Maritime loaned the echosounder used in this study, and its transfiguration into the DEIMOS package was made possible by the expertise of Dick Kreisberg and David Barbee. Funding was provided by the University of Washington School of Aquatic and Fishery Sciences. I am especially grateful to the Victor and Tamara Loosanoff Endowed Fellowship, the Claire L. and Evelyn S. Egtvedt Fellowship, and the H. Mason Keeler Endowment for Excellence for their financial support.

Thanks are also due to the Monterey Bay Aquarium Research Institute for hosting DEIMOS at the MARS observatory, and in to the crews of the R/V *Point Lobos* and ROV *Ventana*. I am deeply grateful to Bruce Robison for inviting me to join the Midwater Ecology Expedition aboard the R/V *Western Flyer* in August 2010, giving me a chance to see animals in the flesh that until then had only been smudges on echograms.

This project owes its conception to my advisor, John Horne, who has been exceptionally supportive through the whole process. My committee, Christian Torgerson and Daniel Schindler, were also very helpful in discussing this work with me, helping to develop my ideas and focus my questions. My lab mates and fellow grad students have kept me honest, stimulated, and entertained during my time at SAFS. Finally, to my family—you have believed in, listened to, put up with, and supported me at every step along the way. Thank you.

1.

INTRODUCTION

1.1 Temporal variability in the ocean

Ocean ecosystems are variable across a wide range of spatial and temporal scales. This variability is generated by a multitude of processes, physical and biological, interacting across an equally-wide range of scales, and our understanding of these processes is largely predicated on the scales at which we are able to observe them. The successful design and interpretation of experiments requires the explicit consideration of the spatial and temporal scale of observations (Stommel 1963, Haury et al. 1978, Steele 1978). Selection of sampling scales in poorly understood systems is a perennial challenge in experimental design, survey planning, and ecological management (Horne and Schneider 1995, Simmonds and Fryer 1996, Wilson 2006). This is especially true in the ocean, where quantities and animals of interest are remote, difficult to sample, and located in a medium inhospitable to humans and our instruments. The converse of this difficulty is the power of scale itself as a descriptor. Characteristic scales of variability, if present, can offer insight into the driving factors behind even complex systems (Holling 1992).

Traditional ship-based sampling has revealed much but is constrained by its discrete nature, the confounding of space and time by a moving platform, and the relatively short duration of any single survey. Persistent shortcomings in our understanding of oceanic biology may stem from the lack of methods for observing its largest habitat—the pelagic zone—at high temporal resolutions. Despite its importance, temporal variability has not always been clearly defined, and its scale is considered less frequently than that of spatial variability (Gaston and McArdle

1994, Schneider 2009, p. 23). In an attempt to attempt to fill this observational gap, this study used the Deep Echo Integrating Marine Observatory System (DEIMOS), an active acoustic observing instrument deployed for 18 months on the continental slope off central California.

The fact that variability in the ocean occurs across a wide range of scales has been recognized in both physical (Stommel 1963) and biological (Haury et al. 1978) oceanography for many years. Figure 1.1 shows a Stommel diagram of hypothesized zooplankton variability drawn by Haury et al. (1978). The diagram portrays variability as a function of spatial and temporal scale, and identifies regions of variability related to physical and corresponding biological processes. From this schematic, it is apparent that not all processes can be resolved using the same sampling resolution. It is interesting to overlay the range of spatial and temporal scales sampled by an acoustic observing instrument such as DEIMOS (Figure 1.1). This domain encompasses several of the processes identified by Haury et al., as well as scales that have been relatively undersampled, particulary those at high temporal resolutions. The sampling scale of DEIMOS is also unusual for its high temporal scope, i.e. the ratio of range over resolution (Schneider 2009). The high sampling resolution and scope suggest that observations from DEIMOS may resolve patterns and processes that other sampling methods do not.

1.2 Ocean observatories and stationary acoustics

Ever since the *Challenger* expedition in 1872, the most common approach to describing and quantifying the marine environment has been ship-based, mobile surveys. An alternative approach is that of marine observatories—typically stationary platforms, on the surface or bottom, providing an attachment point, power, or communications link to scientific instrument packages. Observatories can provide a longer data series than a ship, and do not confound observations in space with time like a moving vessel. Ocean observatories compliment ship-based research, and are poised to play an increasing role in marine science. By sampling multiple variables over long periods in one location, observatories will offer new insights into a variety of ocean processes.

All ocean observatories measure physical quantities—at the very least, temperature and salinity—but fewer are equipped to monitor biological quantities, espe-

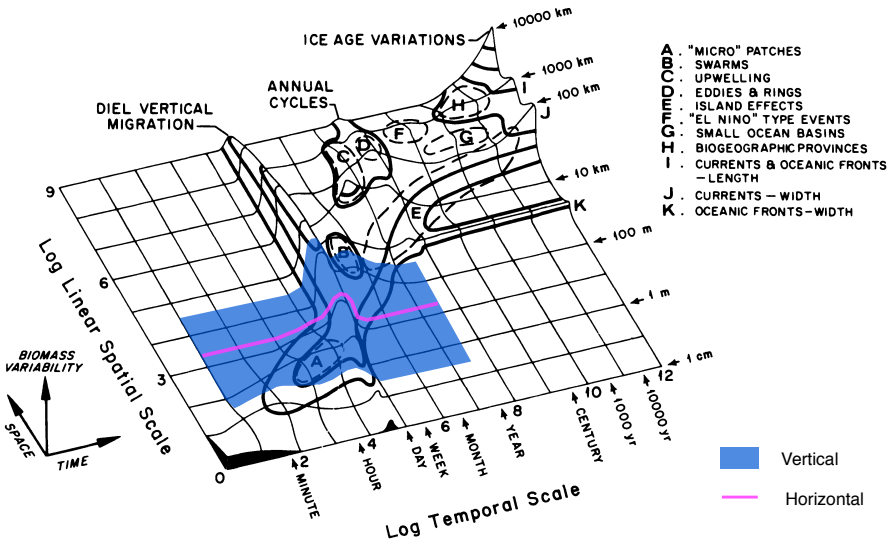

Figure 1.1: Stommel diagram of zooplankton variability, from Haury et al. (1978). Height of the surface represents the magnitude of biomass variability as a function of spatial and temporal scale. Colored regions show scales observed by DEIMOS: blue for the vertical dimension, and purple horizontal.

cially at the mid and upper trophic levels. Active sonar is one technology capable of detecting and measuring biological phenomena from an ocean observatory. Usually deployed on ships in conjunction with net sampling, scientific echosounders are also well suited for use in ocean observatories, providing a synoptic view of fish and zooplankton through the water column with high resolution in both space and time. Taxonomic resolution is coarse, especially in long-term deployments, due to difficulties in identifying species acoustically (Horne 2000). When used as a proxy for biomass, as satellite ocean color is for primary productivity, acoustic backscatter can illuminate patterns and dynamics in the pelagic zone through time.

To date, there have been few bottom-mounted and moored echosounders, with most of these shallow water or short-term deployments. Observatories are therefore a new application for acoustics, and the methods and metrics for describing and analyzing acoustic data in this context are not well developed. Most stationary acoustic work to date has been in near-shore and inland waters (Arrhenius et al. 2000, Čech and Kubečka 2002, Prchalová et al. 2003, Jurvelius and Marjomaeki 2004, Mehner 2006) or fjords (Didrikas and Hansson 2008, Kaartvedt et al. 2009), and di-

rected towards observations of fish behavior. Trevorrow (2005) described fish and zooplankton distributions with relatively shallow (< 50 m) acoustic moorings at two locations in the northeast Pacific, one offshore and one coastal, using echo amplitude statistics and target-strength models to determine the size classes of observed organisms. In the Santa Barbara Basin off Southern California, Osgood and Checkley (1997) deployed a moored ADCP to observe deep aggregations of diapausing copepods. In Monterey Bay, upward-facing acoustics have been used to investigate thin layers of zooplankton (McManus et al. 2005) as well as schooling sardines and anchovies (Kaltenberg et al. 2010). Both of these studies were conducted near shore in the northern bight of the Bay.

A few studies have taken a more general approach, using active acoustics to characterize the aggregate state and variability of the pelagic ecosystem over multiple months and years. Flagg et al. (1994) used acoustic Doppler current profilers (ADCPs) to record currents and biological scattering, in conjunction with chlorophyll-a measurements, over 15 months in the Mid-Atlantic Bight. Cochrane (1994) used an ADCP to measure the temporal variability of euphausiid (*Meganyctiphanes norvegivca*) concentrations over 49 days on the Scotian shelf. An echosounder package was deployed for a year on the Mid-Atlantic Ridge as part of the MAR-ECO cruise in 2004 (Bergstad and Godø 2003). Brierley et al. (2006) used an acoustic mooring to monitor changes in the abundance of Antarctic krill (*Euphausia superba*) over three months at South Georgia Island in the Southern Ocean. Radenac et al. (2010) analyzed ADCP data from the TAO/TRITON array in the equatorial Pacific, linking patterns in the acoustic backscatter with environmental forcing. ADCPs are widely deployed on oceanographic moorings, but quantitative interpretation of their backscatter data is limited by difficulties with their calibration (Brierley et al. 1998).

1.3 Instrumentation

DEIMOS was connected to the Monterey Accelerated Research System (MARS) , a cabled observatory node operated by the Monterey Bay Aquarium Research Institute (MBARI) in Moss Landing. MARS is located at 36°42.7481' North, 122°11.2139' West, approximately 35 km west of Moss Landing, near the 900 m isobath. It is connected to land by a 52 km cable (Figure 1.2, http://www.mbari.org/MARS/).

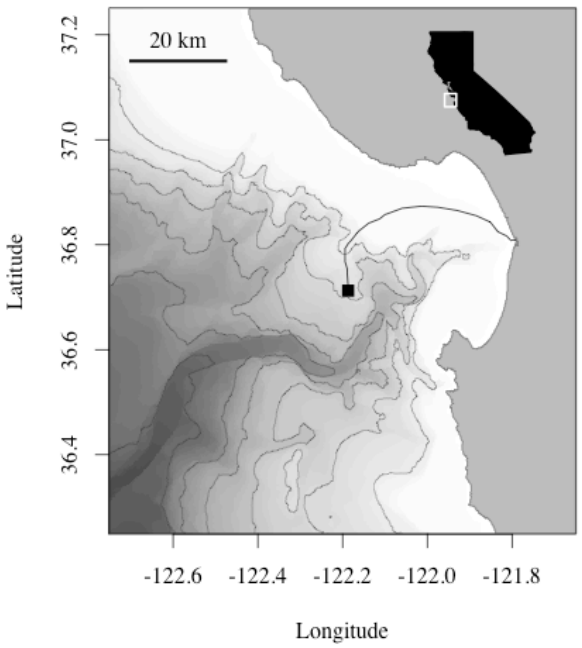

Figure 1.2: Monterey Bay, with MARS node (black square) and cable (black line). Isobaths are at 500 m intervals. Inset shows location on California coast. Bathymetry from Carnigan et al. (2009).

MARS was constructed by MBARI as a test bed for the Ocean Observatories Initiative , a program of the National Science Foundation's Division of Ocean Sciences. The initiative is beginning construction of a network of ocean observatory nodes to be located off both U.S. coasts. MARS is both a proof-of-concept and test bed for new instrument packages. The MARS observatory provides power and high-speed data connectivity to as many as eight instruments, allowing them to be deployed indefinitely, collect data continuously at high rates, and be controlled and remotely monitored in real time. MARS is accessed and serviced by MBARI's research vessel *Point Lobos* and the ROV *Ventana*. Dives are conducted semi-regularly to service the node and connected instruments.

An active acoustic observing package, DEIMOS was built around a Simrad EK60 38 kHz scientific echosounder. It transmitted an acoustic pulse upward and recorded the reflected sound (i.e. backscatter) every five seconds, compiling a depth-time record of the vertical distribution of pelagic fauna. All components used in the construction were commercially available off-the-shelf. DEIMOS was tested in-water

for one month in Puget Sound, WA in 2008 and deployed in Monterey Bay during the last week of February 2009 by the ROV *Ventana* from the R/V *Point Lobos*. DEIMOS was recovered on August 18 2010, again by the *Ventana* and *Point Lobos*. In that time, it recorded variability in pelagic backscatter from seasonal changes in the structure of scattering layers to predator-prey dynamics at the scale of minutes.

1.3.1 Monterey Bay and the California Current

Monterey Bay is a large open embayment in the central California coast. It is primarily shallow (depth < 100 m), but is bisected by the Monterey Submarine Canyon, which brings deep water habitat into the middle of the bay and close to shore. Located in the eastern-boundary California Current, the Bay's oceanographic and biological seasons are determined chiefly by the presence of episodic wind-driven upwelling from spring to fall, and its absence during the winter (Huyer 1983). The pelagic community of Monterey Bay is invertebrate-dominated, including copepods, euphausiids, ctenophores, hydromedusae, siphonophores, and chaetognaths (Bigelow and Leslie 1930, Colebrook 1977). Small pelagic fish (Pacific sardine, *Sardinops sagax* and anchovy, *Engraulis mordax*) and squid are also abundant, and are the targets of commercial fisheries (Cailliet et al. 1979). Larger fish, pinnipeds, and cetaceans top the food web (Croll et al. 2005). The California Current is representative of eastern boundary current ecosystems; driven by upwelling, they are among the most productive marine ecosystems (Pauly and Christensen 1995). Monterey Bay is also a major site of scientific investigation by several research institutes located around its rim, and a rich body of literature is available on many aspects of the bay's oceanography and biology spanning multiple decades.

Many of the important dynamics, such as wind-driven upwelling and primary productivity, have been studied for many years in Monterey Bay and the California Current (Skogsberg 1936, Skogsberg and Phelps 1946, Broenkow and Smethie 1978, Rosenfeld et al. 1994, Liang and Robinson 2009). The California Cooperative Oceanic Fisheries Investgations (CalCOFI) has conducted annual surveys off the coast of California since 1950, and the inhabitants of the pelagic zone are well known. In addition, MBARI's ROV program has collected data on many mesopelagic organisms too fragile to be sampled with nets (Robison 2004). Some of these, such as physonect siphonophores, may be important predators on zooplank-

ton and micronekton as well as strong acoustic scatterers, due to their gas-filled pneumatophore (Robison et al. 1998). Data sets such as CalCOFI's have allowed the study of variability and bio-physical coupling in phytoplankton, zooplankton, and fish at interannual and decadal time scales (Schrader 1981, Brinton and Townsend 2003, Rebstock 2003, Collins et al. 2003, Lavaniegos and Ohman 2003, 2007), while *in situ* and remote sensors have been used to monitor the Bay's physical oceanography and primary production on seasonal and shorter time scales (Service et al. 1998, Clarke and Dottori 2008, Liang and Robinson 2009).

Even though Monterey Bay and the California Current have been studied extensively, it has not been possible to monitor mid and upper trophic levels at similar resolutions over extended periods. There is an observational gap between high-frequency, high-resolution oceanographic data and the longer term, lower resolution biological data. The unusual spatiotemporal scale of DEIMOS's data offers a unique opportunity to bridge this gap, though the difficulties of ground-truthing and acoustic species identification remain (Horne 2000). In this sense, Monterey Bay is an advantageous location for collecting long-term acoustic data, since in the absence of coincident direct sampling, biological interpretation of acoustic data is limited by prior knowledge of the system and its constituents.

1.4 Thesis objectives and organization

This study has two objectives. First, it aims to describe temporal patterns in the vertical distribution of pelagic animals. This objective presents several challenges. The most basic stem from the sheer abundance of data, which includes complex patterns in both the vertical and temporal dimensions. My analytic approach developed a set of summary metrics to parsimoniously describe the vertical distribution of acoustic backscatter. The metric suite includes measures of abundance, density, occupancy, location, dispersion, and aggregation. I also developed an image-analysis-based algorithm for detecting and counting the number of distinct scattering layers present in an echogram. All metrics were tested for their sensitivity to the parameters used in their calculation. These metrics were then calculated through the entire deployment and used to quantify temporal variability in the vertical distribution of animals in Monterey Bay's pelagic zone. In the description of pattern, I relied mainly on frequency-domain approaches, including Fourier and wavelet

transforms, which enabled simultaneous measurement of variability across a wide range of temporal scales. The development of the metrics, their testing, and use in quantifying temporal patterns are described in Chapter 2.

The second objective of this thesis was to quantify the response of pelagic fauna to environmental variability, especially at the shorter time scales difficult to observe with traditional sampling methods. These time scales encompass processes such as wind-driven upwelling, known to be of great importance in the California Current, but difficult to observe below the surface of the water or at trophic levels above primary producers. I compared metrics derived from the acoustic record to physical and biological time series measured at the M1 data buoy, operated by MBARI and located near DEIMOS, and at the Monterey tide gauge, maintained by the National Oceanographic and Atmospheric Administration (NOAA). These comparisons were made using cross-correlation and cross-wavelet statistics, with an example application using a multivariate time series model. I also split the water column into several discrete zones, based on biological reasoning and persistent features of the echograms, in an attempt to measure bio-physical coupling as a function of depth. These analyses are detailed in Chapter 3. Chapter 4 provides a summary of the previous two chapters and addresses the significance of the work in a broader context. Finally, the complete acoustic dataset is reproduced as reduced-scale echograms in Appendix A.

2.

ACOUSTIC METRICS AND TEMPORAL VARIABILITY OF PELAGIC FAUNA

2.1 Introduction

Aquatic ecosystems display dynamic behavior across a wide range of temporal and spatial scales, with physical and biological processes occurring both quickly and slowly over short and long distances (Stommel 1963, Haury et al. 1978, Steele 1978). Understanding these processes depends on understanding their variability. Temporal variability has been measured less frequently than spatial variability, especially in aquatic ecosystems. Long-term, high-resolution measurements are common for physical variables, but biologists have typically had to be content with time series that are either short with high resolution, or long with a low sampling frequency. In an incompletely understood system, the scope (i.e. resolution over extent) of observations determines their power to detect patterns present at multiple scales (Schneider 2009). If true, the relative scarcity of high-scope biological time series may represent a significant gap in our ecological knowledge.

The constraints of a ship-based sampling approach include the difficulty of collecting high-scope time series, and the confounding of space and time when traversing a study area. Ocean observatories are an alternative approach complementing ship-based research, and are poised to play an increasing role in marine biology

At the time of submission of this thesis, a version of this chapter had been published as: Urmy, S., J. Horne, and D. Barbee, 2012. Measuring the vertical distributional variability of pelagic fauna in Monterey Bay. *ICES Journal of Marine Science* 69, 184-196.

(Horne 2005). Active acoustics are a useful addition to observatory systems, providing a synoptic view of fish and zooplankton through the water column with high resolution in both space and time, but with their own constraints.

Taxonomic resolution is coarse in long-term active acoustic deployments, owing to the expense and difficulty of concurrent direct sampling, and the difficulty of acoustic species discrimination (Horne 2000), though backscatter can be used as a proxy for biomass density (Foote 1983, Benoit-Bird and Au 2002). The quantity and complexity of data yielded by a continuously-operating acoustic package present challenges of their own, and there is a need for efficient, objective, and meaningful methods to describe patterns within it.

The objectives of this chapter were twofold. The first was to develop methods to characterize the distribution of animals in the water column. To this end, a suite of summary metrics was developed to measure characteristics and features of the vertical density distribution. The second objective was to use these metrics to quantify temporal variability in Monterey Bay through time and across temporal scales, identifying dominant modes of variability and significant changes in the ecosystem.

2.2 Methods

2.2.1 Instrument and Data

The MARS observatory node, operated by the Monterey Bay Aquarium Research Institute (MBARI), is located at 36°42.75′ N 122° 11.21′ W near 900 m depth on the continental slope north of the Canyon (Figure 1.2). MARS is connected to shore by a 52 km cable, providing continuous power and communications for up to eight scientific instruments. The node consists of a $3.7 \times 4.6 \times 1.2$ m trawl-resistant metal frame housing an electronics assembly, which regulates power and transmits data to shore. Instruments are deployed and recovered by remotely operated vehicles (ROVs) off MBARI vessels.

DEIMOS was built around a Simrad EK60 38 kHz scientific echosounder. The 38DD transducer had a beam width of 7° between half-power points and was oil-filled, allowing operation at depths up to 1500 m. The transceiver and other electronics, including a power supply and switch with an IP-addressable relay, allowing the system to be reset remotely, were housed in a borosilicate glass pressure

sphere. All components were mounted on a galvanized steel frame. The echosounder sampled the water column at a frequency of 0.2 Hz, using a pulse length of 1.024 ms. Transmitted power was restricted to 825 W to conform to sound pressure levels specified in the US Marine Mammal Protection Act and Endangered Species Act . DEIMOS was deployed at 875 m depth from February 27, 2009, to August 18, 2010.

Over the approximately 18-month deployment, data collection was interrupted several times, due to problems with software, communications, and the power supply. The longest of these interruptions occurred from May 18 to August 14, 2009, when a reduced load on the 48 V power supply following the recovery of another instrument package at the MARS node increased electrical noise, saturating DEIMOS's receiver and rendering the data unusable. Three other multi-day outages occurred. An unnoticed software crash halted data collection from September 3-13, 2009, and electrical noise in the power supply again stopped data collection from March 23-April 7, 2010. On July 22, 2010, burrowing rodents gnawed through MARS's cable on shore, cutting off communication with the node until August 3, when repair of the cable was completed . In January 2010, an automated script was put in place to monitor data acquisition, sending an alert email if no new data had been collected in 10 minutes.

DEIMOS was calibrated *in situ* using a 38.1 mm tungsten carbide reference-sphere following procedures outlined in Foote et al. (1987). On June 24, 2010, the ROV Ventana put the calibration apparatus in place. The sphere was held 12 m above the transducer face, anchored by two small lead weights on either side of the transducer and suspended from a syntactic foam float five meters above. All calibration components were connected by monofilament line. The sphere moved through the acoustic beam with the currents, and completed beam coverage in 3-4 days. The calibration sphere was left in place for eight weeks and removed August 17, one day before DEIMOS was recovered. In that period, we conducted nine calibrations. For each calibration, beam angle corrections were calculated using Simrad's LOBE program, while gain and area-backscattering coefficient (s_a) corrections were calculated by integrating all on-axis target detections using Echoview software (v. 4.9, Myriax Pty. Ltd. 2010). Before beginning analysis, we corrected all raw acoustic data using the mean values of these calibration parameters.

Acoustic data files were processed using Echoview. Initial processing removed noise interference (e.g. electrical fluctuations, passing ships) and identified data

gaps. The top 10 m and bottom 7 m of the water column were excluded from analysis to avoid integrating turbulence and bubbles from breaking waves or echoes in the acoustic near-field. Background noise was estimated and subtracted using methods reported in DeRobertis and Higginbottom (2007). DeRobertis and Higginbottom recommend collecting data at least 600 m below the bottom (in our case, above the surface) for unbiased noise estimates. Though we only collected data to approximately 300 m above the surface, we did not find any difference between the estimates from their algorithm and standard estimates using passive listening data (Nunnallee 1990). We did not apply a signal-to-noise ratio (SNR) threshold to the final de-noised data, since during extended periods of slightly higher background noise, the mean volume backscattering values were biased low by eliminating pixels with a low SNR. After elimination of bad data regions and noise subtraction, acoustic data were exported from Echoview in 5 sec by 0.5 m time-depth matrices of mean volume backscattering strength (S_v, MacLennan et al. 2002) for further analysis.

2.2.2 *Metric Selection and Testing*

To parsimoniously describe this large dataset, we developed a suite of metrics to characterize the vertical distribution of acoustic backscatter through time. Acoustic backscatter is interpreted as a proxy for the density of aquatic organisms (Foote, 1983). Metrics were derived from backscatter, as well as indices used to describe the spatial structure and variance of animal population densities (Bez and Rivoirard 2001, Woillez et al. 2007, Burgos and Horne 2008). These metrics quantified the vertical distribution of pelagic animals including total abundance, mean density, occupied area, mean location, spread, evenness, aggregation, and the number of backscattering layers present (Table 2.1). In the descriptions below, volume and area backscattering strengths (S_v and S_a) are the logarithmic forms of the volume and area backscattering coefficients s_v and sa (i.e., $S_v = 10\log_{10}(s_v)$). Note these two metrics have different reference units: S_a is measured in dB re. 1 m^{-1}, while S_v is measured in dB re. 1 m^2 m^{-2}. Where the context is clear, both will hereafter be abbreviated to "dB." All calculations were performed using linear units.

Depth-integrated backscatter, a proxy of total biomass in the water column, was measured using the area backscattering strength S_a, the integral of volumetric

Table 2.1: Metrics for description of the vertical distribtion of pelagic biomass, estimated by acoustic backscatter. In all formulas, z represents depth, and $s_v(z)$ the volume backscattering coefficient at depth z. H is the total water column depth. Numbers in the "reference" column refer to (1) MacLennan et al. 2002, (2) Bez and Rivoirard 2001, and (3) Woillez et al. 2007.

Quantity	Metric	Symbol	Formula	Units	Reference
Density	Mean volume backscattering strength	S_v	$10\log_{10}\left(\frac{\int s_v(z)\,dz}{H}\right)$	dB re. 1 m^{-1}	1
Abundance	Area backscattering strength	S_a	$10\log_{10}\left(\int s_v(z)\,dz\right)$	dB re. 1 m^2 m^{-2}	1
Location	Center of mass	CM	$\frac{\int z\,s_v(z)\,dz}{\int s_v(z)\,dz}$	m	2, 3
Dispersion	Inertia	I	$\frac{\int (CM-z)^2\,s_v(z)\,dz}{\int s_v(z)\,dz}$	m^{-2}	2, 3
Occupied area	Proportion occupied	P_{occ}	$\frac{\int z \vert s_v(z) > s_{v,thresh}\,dz}{H}$	–	2, 3
Evenness	Equivalent area	EA	$\frac{\left(\int s_v(z)\,dz\right)^2}{\int s_v(z)^2\,dz}$	m	2, 3
Aggregation	Index of Aggregation	IA	$\frac{\int s_v(z)^2\,dz}{\left(\int s_v(z)\,dz\right)^2}$	m^{-1}	2, 3
Layer structure	Number of layers	N_{layers}	See explanation in text	#	

backscatter (s_v) over the entire water column expressed as a decibel value (MacLennan et al. 2002). Mean density was measured using the mean volume backscattering strength S_v. Occupancy was calculated as the proportion (P_{occ}) of the water column with S_v above -90 dB. Mean location was measured using the center of "mass" *CM*, the average of all depths sampled weighted by their respective s_v values. Bez and Rivoirard's (2001) inertia *I* measures dispersion or spread as the sum of squared distances from the center of mass, weighted by the s_v at each distance and normalized by the total s_a. Evenness was measured by the equivalent area *EA*, calculated as the squared integral of s_v over depth (i.e., s_a^2) divided by the depth integral of s_v^2. Values represent the area that would be occupied if all data cells contained the mean density (Woillez et al. 2007). This quantity can alternatively be expressed as its reciprocal, the Index of Aggregation *IA*, which is high when small areas are much denser than the rest of the distribution. Metrics were calculated from the processed data using Python scripts with the SciPy module for efficient array operations (Jones et al. 2001–2012). Applying these spatial statistics in one dimension (i.e., depth) for each ping yielded time series summarizing each quantity of interest over the entire deployment. Figure 2.1 shows a representative echogram over two days (2-4 March 2009), with the corresponding metric time series. The metrics track diel vertical migration, including the formation and dissolution of layers, as well as the passage of aggregations near the surface.

The final metric in our suite, the number of scattering layers present , used an image-analysis approach. We defined "layers" as local backscatter maxima in the vertical direction, and used the slope of backscatter intensity with depth to identify them. The echogram was first smoothed by convolution with a Gaussian kernel to eliminate small-scale variability. We then estimated the first and second derivatives of S_v in the vertical direction on the smoothed echogram, by taking the first and second differences along the vertical axis. Layers were then defined as locations where the absolute value of the first derivative was close to zero, and the second derivative was negative. The first of these conditions selected areas where S_v did not change much with depth, meaning the tops of ridges (i.e. layers) and the bottoms of the troughs between them. The second condition, a negative second derivative, ensured that only areas at the tops of ridges would be selected. Before counting the layers, two additional filtering operations were performed. The first was a convolution with a median filter, replacing each pixel's value with the me-

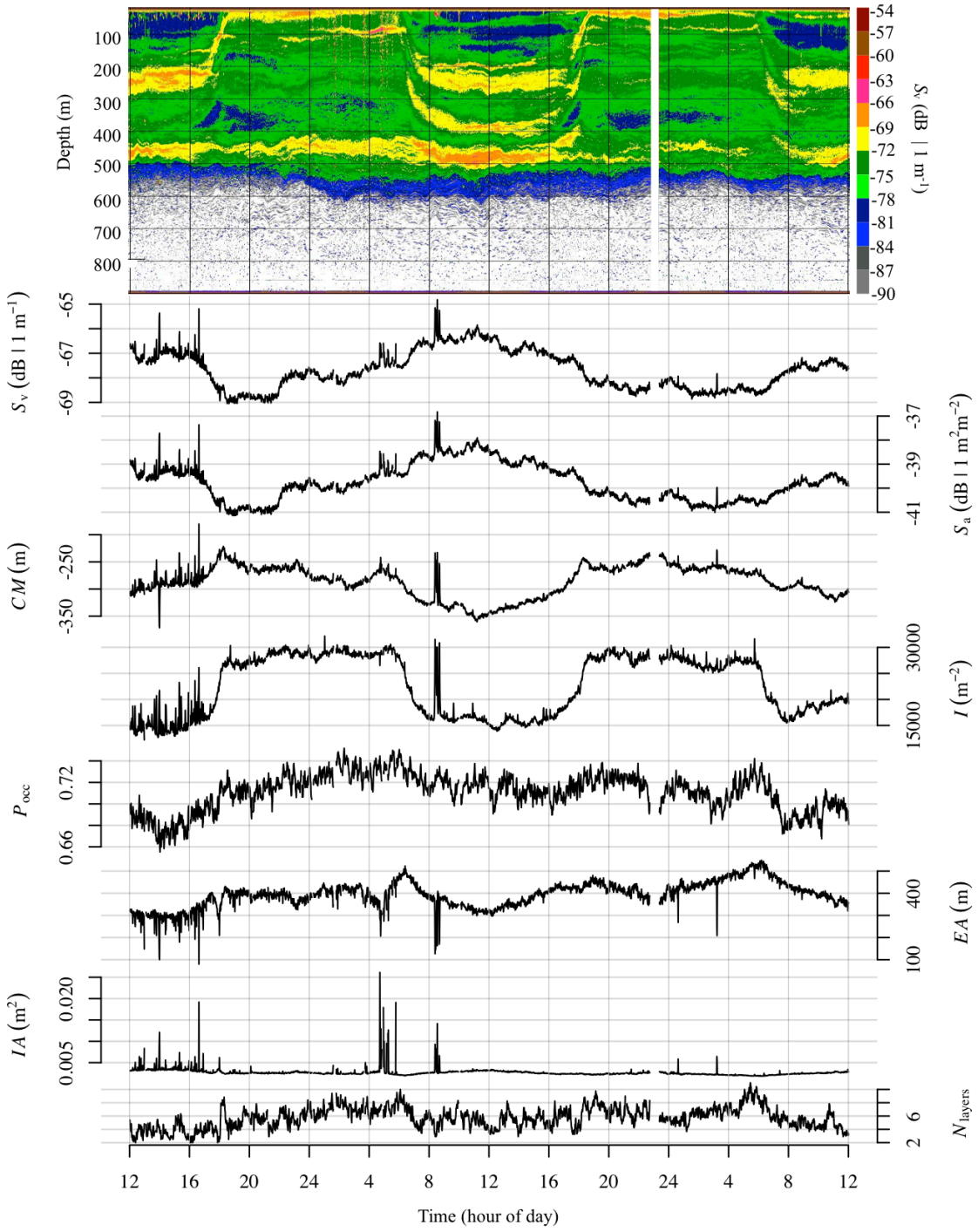

Figure 2.1: Echogram of March 2-4, 2009, with corresponding metrics plotted below. From top to bottom, metrics are mean volume backscattering strength, S_v, area backscattering strength S_a, center of mass CM, inertia I, proportion occupied P_{occ}, equivalent area EA, index of aggregation IA, and number of layers, N_{layers}. Refer to methods and 2.1 for calculation and details.

dian of all cells in its neighborhood. This operation ensured that pixels meeting the two slope-based conditions would not be counted as layers if they were isolated in "non-layer" regions. The second was a convolution with a dilation filter, replacing each pixel with the maximum value in its neighborhood. This operation eliminated isolated "non-layer" pixels within "layer" regions. It was then possible to count the number of transitions between "layer" and "non-layer" in each ping. This number, divided by two, yielded the number of layers present in the water column.

The number of layers detected will depend in part on the parameter values: the acoustic threshold, the slope threshold defining where the derivative is close to zero, and the widths of the three filtering windows. To select appropriate values for these parameters, we visually inspected "type" echograms from different times of the year. When two people compared the number of layers identified by eye, the greatest difference between their counts was one layer, and in all cases less than ten layers were identified visually. We selected initial values for the algorithm's parameters by starting with the smallest possible filter widths and incrementally widening them until the algorithm appeared to give results agreeing with the number of layers identified by eye. Based on this heuristic approach, we selected initial parameter values of 19×19 pixels (9.5 m $\times$ 95 sec) for the standard deviation of the Gaussian filter, 0.2 dB m^{-1} for the slope threshold, and 19×19 pixels for the median and dilation filters.

To test the response of the layer detection algorithm to different combinations of input parameters, we conducted a Monte Carlo-based global sensitivity analysis. Input parameters were randomly selected using a Latin hypercube sampling (LHS) design (McKay et al. 1979) . In an LHS design, the possible range of each parameter is divided into n strata, sized according to the probability density, and one value is selected randomly from each of these intervals. In each iteration, one of these n values is drawn randomly for each parameter. The number of iterations in the Monte Carlo run is equal to the number of strata. LHS sampling has the advantage of ensuring that all portions of each input parameter's range are tested simultaneously, without requiring the testing of all permutations of all parameters. Complete coverage of the multidimensional parameter space is not guaranteed in a single run, so multiple runs must be conducted. Rose (1982) found that an LHS design with 200 runs produced stable results; this number is used here. Each parameter's range was divided into 10 equal strata, with ranges spanning the practical width of each

parameter's values. The three convolution filters could have widths between 1 and 31 pixels, representing smoothing operations ranging from no smoothing to the approximate width of the layer features we visually identified. The slope threshold, controlling which areas of the echogram were designated as "flat" (and hence candidates for inclusion in layers), could take values from 0 to 0.15 dB m^{-1}. Based on informal testing, values above 0.15 dB m^{-1} included regions of the echogram that were sloped. The range of the acoustic threshold was set from -100 to -65 dB.

To ensure applicability of our results to the entire data set, we divided the acoustic record into 30 equal strata and randomly selected one data file from each stratum to repeat the Monte Carlo runs. Each file contained acoustic data from a period of about three hours. Within each file, we randomly selected 30 pings (i.e. individual profiles of the water column) in which to count layers after application of the detection algorithm. Testing data from all periods of the deployment let us compare variability due to parameter adjustments with variability due to changes in the layer structure over time. The other metrics underwent Monte Carlo sensitivity testing analogous to that used on the layer-detection algorithm, though there was only one parameter to adjust, the acoustic threshold, making an LHC design unnecessary.

2.2.3 *Pattern Description*

For computational convenience and to ensure even spacing in time, all metric series were averaged into 1-hour bins. A principal component analysis (PCA) assessed the degree of colinearity among metrics. Since metrics do not share the same units, they were transformed to have zero mean and unit variance before conducting the PCA. All metrics displayed an annual trend, which we removed by fitting sinusoids with one- and half-year periods to the data using ordinary least squares. All further analysis was performed on the residuals from these fits.

We used Fourier and wavelet transforms to characterize variability in the detrended metric series as a function of temporal scale. Wavelet transforms decompose a series across time and frequency simultaneously, allowing the analysis of series that are non-stationary or contain frequency components at some times and not others. This is accomplished by convolving the series with a localized waveform (the wavelet), which is stretched or compressed to different scales, analogous

to periods in Fourier analysis. The product is a two-dimensional image, mapping variability in the series as a function of time and scale. Wavelets offer the advantage over Fourier transforms of being able to locate transient frequency components in time. They also offer advantages over the short-time Fourier transform (STFT), in that their resolution is not fixed (Kaiser 1994), allowing good time resolution for high-frequency events and good frequency resolution for low-frequency events.

Because both Fourier and wavelet transforms require gap-free series with evenly-spaced observations, a gap-filling scheme was used to fill periods of missing data. We used the stochastic interpolation method described in Percival et al. (2008). This algorithm uses the autocorrelation structure of the observed data to interpolate the expected value of missing observations between points on either side of the gap. It then adds an appropriately-autocorrelated stochastic noise component. The simulated data in the gap can be regarded as a realization of one section of the process that produced the rest of the time series, and the gap-filled series can then be used to calculate any subsequent statistics requiring continuous observations. By generating many realizations of the stochastic component, calculating the desired statistic each time, and then taking the mean of all calculated statistics, confidence in the results is increased. This method uses the best linear predictor of the missing values, given the observations on either side of the gap and the autocorrelation structure of the series. It also preserves the periodic and stochastic characteristics of the rest of the series.

To carry out this gap-filling procedure, an autocovariance function (ACVF) for the series is necessary. Percival et al. (2008) used theoretical ACVFs calculated from autoregressive (AR) and fractionally differenced (FD) models (cf. Brockwell and Davis 2002, Hosking 1981) they had fit to their time series. Based on preliminary examination, our data showed both periodic behavior and long-range autocorrelation, meaning that reasonably low-order AR and FD models would be poor fits to the data. Rather than try to build a complicated time series model, we took a non-parametric approach and used the sample ACVF. A total of 500 realizations of the gap-filling process were generated, with the Fourier and wavelet spectrum of each realization calculated as described below. The mean of these 500 spectra was then used as the final value for each transform.

Power spectra were calculated for the gap-filled series using the fast Fourier transform (FFT, Cooley and Tukey 1965), and normalized by a factor of $N^{-1}\sigma^{-2}$

(where N is the length of the series and σ^2 is its variance). The final spectrum, averaged over all 500 gap-filling realizations, was smoothed with a modified Daniell kernel of width 15 (Daniell 1946). Regression curves were fit to the unsmoothed final spectrum to model the dependence of variability on frequency.

Wavelet spectra of the metric series were calculated using continuous wavelet transforms (CWT), following procedures described in Torrence and Compo (1998). The CWT is a highly redundant (i.e., non-orthogonal) transform, though this redundancy gives it fine resolution in time and scale (Torrence and Compo 1998, Cornish et al. 2006). There are a number of continuous wavelet functions available, each with different properties. We used the Morlet wavelet with a frequency of 6, which has been used in geophysical and ecological analyses (Goupillaud et al. 1984, Ménard et al. 2007, Keitt 2008) and offers a good compromise between time and frequency resolution (Torrence and Compo 1998). The wavelet spectra were tested for significance at the 0.95 level against the theoretical spectrum of a first-order autoregressive process fit to each series (Torrence and Compo 1998).

2.3 Results

2.3.1 Metric Sensitivity and Characteristics

The layer-detection algorithm proved relatively insensitive to the choice of parameters near the initial, visually-selected values (Figure 2.2). The average number of layers detected decreased gradually from 10.6 to 3.1 as the acoustic threshold was raised from -100 to -65 dB. This result reflected the exclusion of weaker scattering layers below a higher threshold. As the slope threshold was raised from 0 to 0.08 dB m^{-1}, the mean number of layers detected increased from 0.9 to 8.0, and then remained relatively flat through the maximum threshold tested, 0.3 dB m^{-1}. The algorithm was most sensitive to the widths of the convolution filters used, in particular the Gaussian smoothing filter and the median filter. Mean number of layers increased from 0.4 to 10.5 as the standard deviation of the Gaussian filter was increased from 1 to 8 pixels. The mean number of layers then decreased to 5.6 as the filter was widened to the maximum value tested, a standard deviation of 30 pixels. When the median filter was at its narrowest, the mean number of layers detected was 16.9, decreasing as the filtering window was widened. Once the median filter

was wider than 13 pixels, the mean number of layers remained relatively constant between 4.7 and 6.8. The number of layers was less sensitive to the dilation filter, decreasing approximately linearly from 8 to 3 as the filter was widened from 1 to 33 pixels. For all three filters, narrower widths gave less predictable behavior. At their lowest values, some layer counts as high as 50 or 60 layers were observed, far outside the range of values identified visually. At wider widths (> 10-12 pixels), the coefficients of variation (CV) for all three were relatively steady with values < 1. Looking at the number of layers across all parameter combinations as a function of the time of year, a clear seasonal pattern in the mean number was visible, matching the pattern identified visually.

The remaining metrics displayed different degrees of sensitivity to the choice of acoustic threshold (Figure 2.3). The *CM* and *I* were insensitive to the threshold, though their CVs increased and decreased, respectively, as the threshold was raised. *EA* and P_{occ} both decreased as the threshold was raised. Total water column S_a decreased very slightly when the threshold was raised above -70 dB. At the same time, the mean S_v increased, reflecting the exclusion of less-dense areas with low backscatter values. This masking of low-density areas was also reflected in the *IA*, which increased when the threshold was raised above -70 dB.

The PCA of the metric series showed a moderate degree of colinearity among them (Figure 2.4). The first component accounted for 62.0% of the total variance, with the second and third components accounting for 17.2 and 8.6%. When summed, the first 4 principal components accounted for 95% of the variance. P_{occ}, N_{layers}, and *I* were all correlated, and aligned with the first component. The *CM* was aligned negatively with the first component. The *IA* and *EA* were anti-correlated with each other, with loadings orthogonal to those of S_a and S_v, which were strongly collinear.

2.3.2 *Pattern description*

Collectively, the eight metrics captured a seasonal cycle in the vertical density distribution of Monterey Bay's pelagic fauna (Figure 2.5). Total integrated backscatter reached a minimum (S_a < □55 dB) in May of both years of the deployment, with the water column largely empty (P_{occ} < 0.1). Biomass was concentrated near the surface (*CM* > -200 m). By late summer, S_a had increased to approximately -40 dB

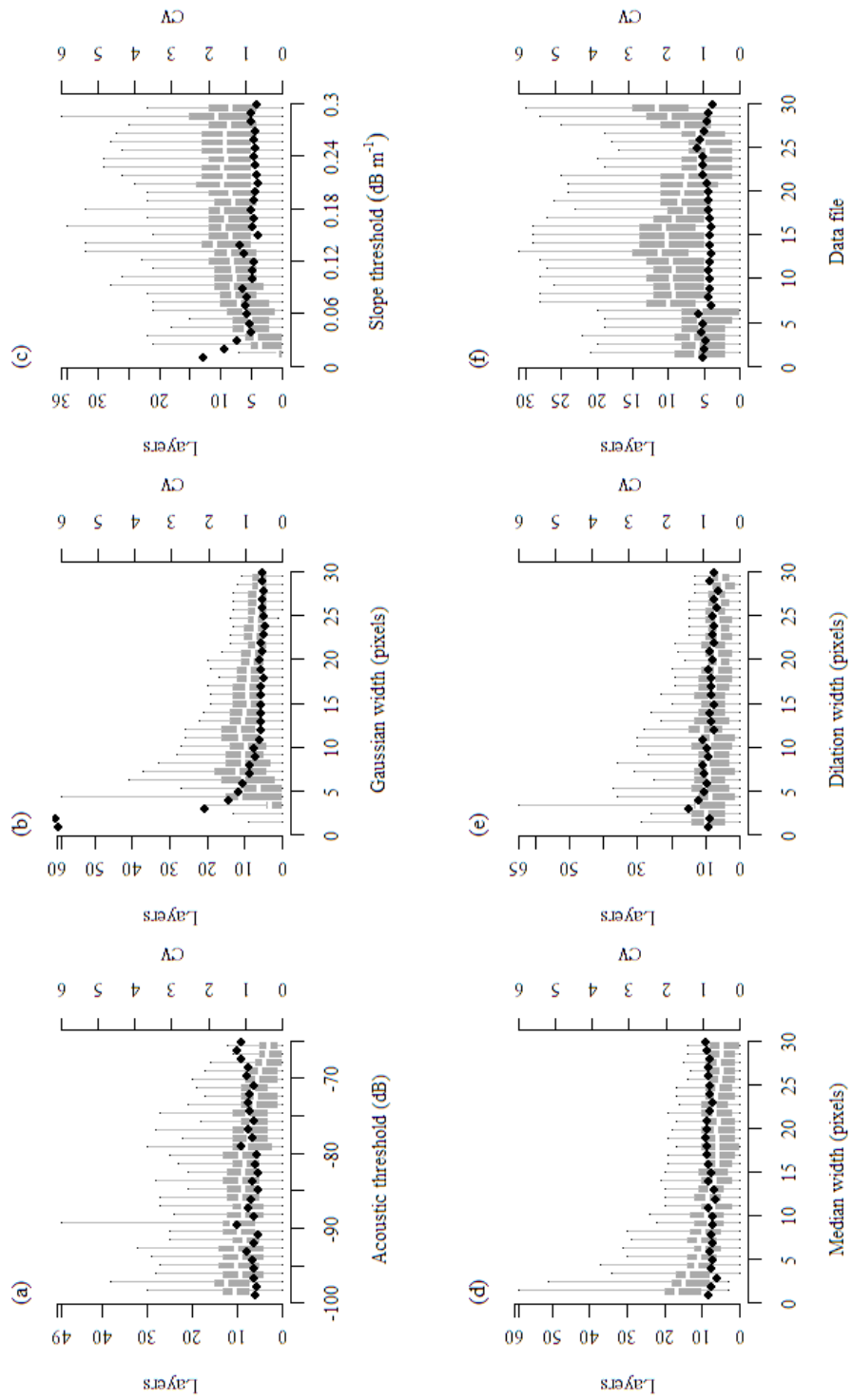

Figure 2.2: Sensitivity of layer-detection algorithm to choice of parameters. Box-and-whisker plots show mean, interquartile, and 95th percentiles of number of layers counted at each parameter value (left axis). Black points show coefficient of variation at each parameter value (right axis). Subplots show response of the algorithm with different values of (a) acoustic threshold, (b) width of Gaussian smoothing filter, (c) zero-slope threshold, (d) width of median smoothing filter, (e) width of dilation filter, and (f) data file (i.e. data subset) on which the algorithm was tested.

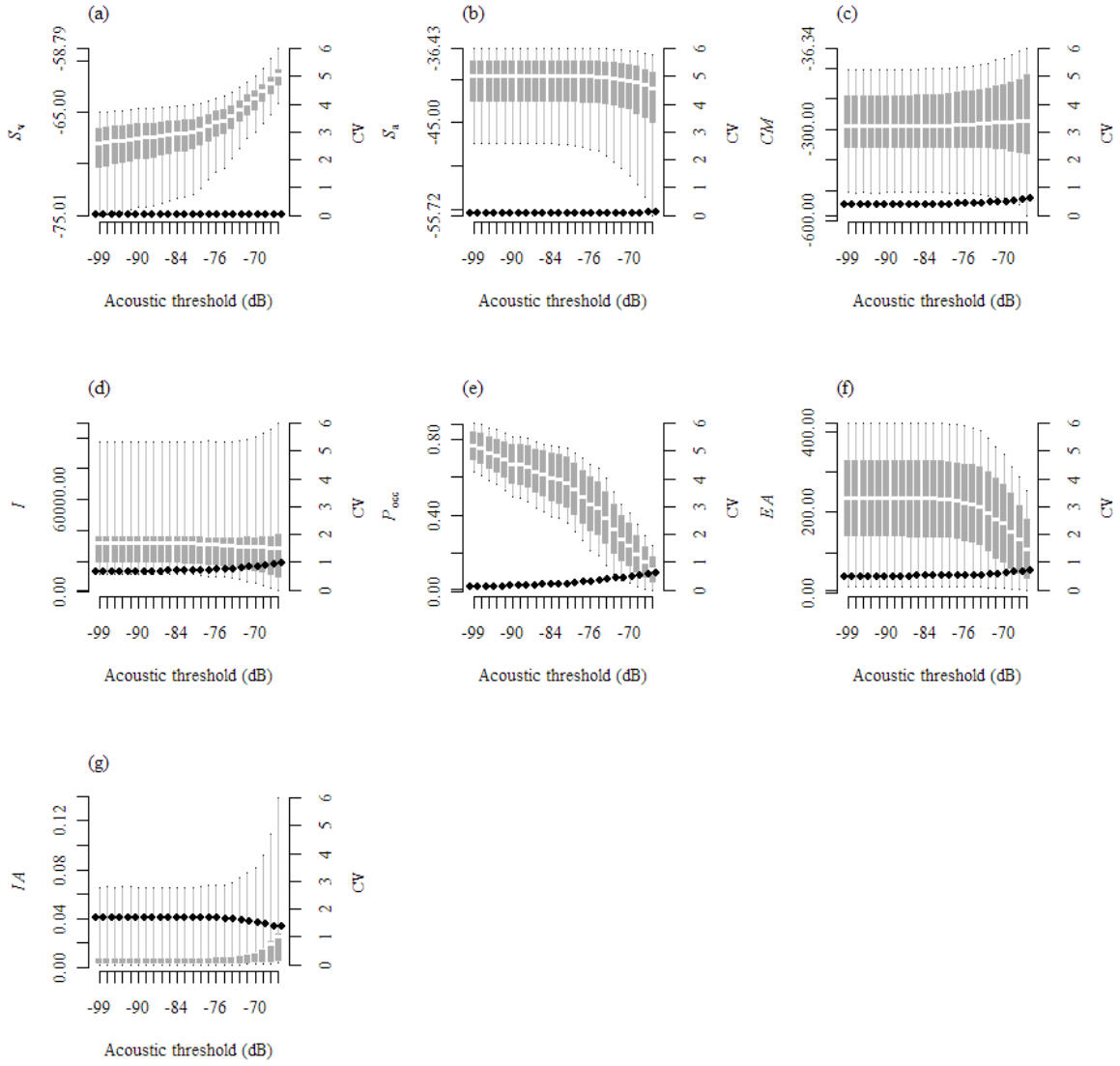

Figure 2.3: Sensitivity of metrics to choice of acoustic threshold. Box-and-whisker plots show mean, interquartile, and 95th percentiles of metric values (left axis). Black points show coefficient of variation at each acoustic threshold (right axis). (a) Mean volume backscattering strength, S_v, (b) area backscattering strength, S_a, (c) center of mass, *CM*, (d) inertia, *I*, (e) proportion occupied, P_{occ}, (f) equivalent area, *EA*, (g) index of aggregation, *IA*.

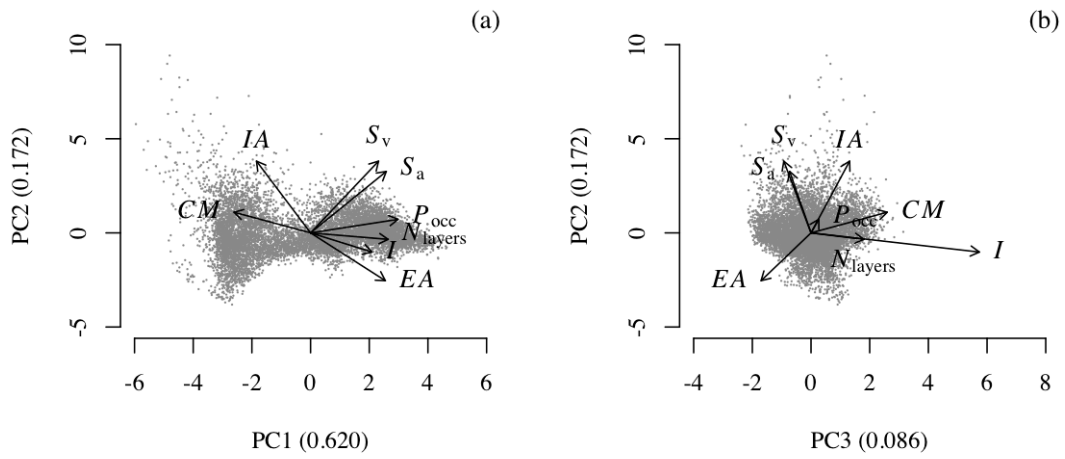

Figure 2.4: Principal component analysis of metric time series. (a) Biplot, showing values of first two principal components (points) and loadings of metrics along these two components (labeled). (b) Same as in (a), showing second and third principal components. Numbers in parentheses on axis labels show proportion of variance explained by the corresponding component.

due to the appearance of a large, non-migrating scattering layer between -400 and -600 m. The presence of this deep layer lowered the *CM* to -500 m and raised the occupancy to 0.7. Over the fall and winter, the deep layer gradually thinned, causing the occupied proportion of the water column to decline and the *CM* to rise. Total backscatter and mean density (S_a and S_v) remained high during this period, due to the presence of a dense scattering layer near the surface. By spring 2010, the vertical distribution was similar to that seen the previous year, with S_a 14 dB below its winter peak and concentrated high in the water column (i.e. *CM* near -100 m). From its lowest point in May 2010, S_a climbed rapidly through June and July, coinciding with the reappearance of the deep scattering layer. There was typically a distinct boundary at the bottom of the lowest scattering layer, below which only low densities of individual targets were observed. This boundary moved upwards in late winter and spring to a depth of approximately 400 m before moving down again in the summer, reaching depths of over 700 m in early September 2009 and late August 2010.

This seasonal cycle accounted for large proportions of the variability in all met-

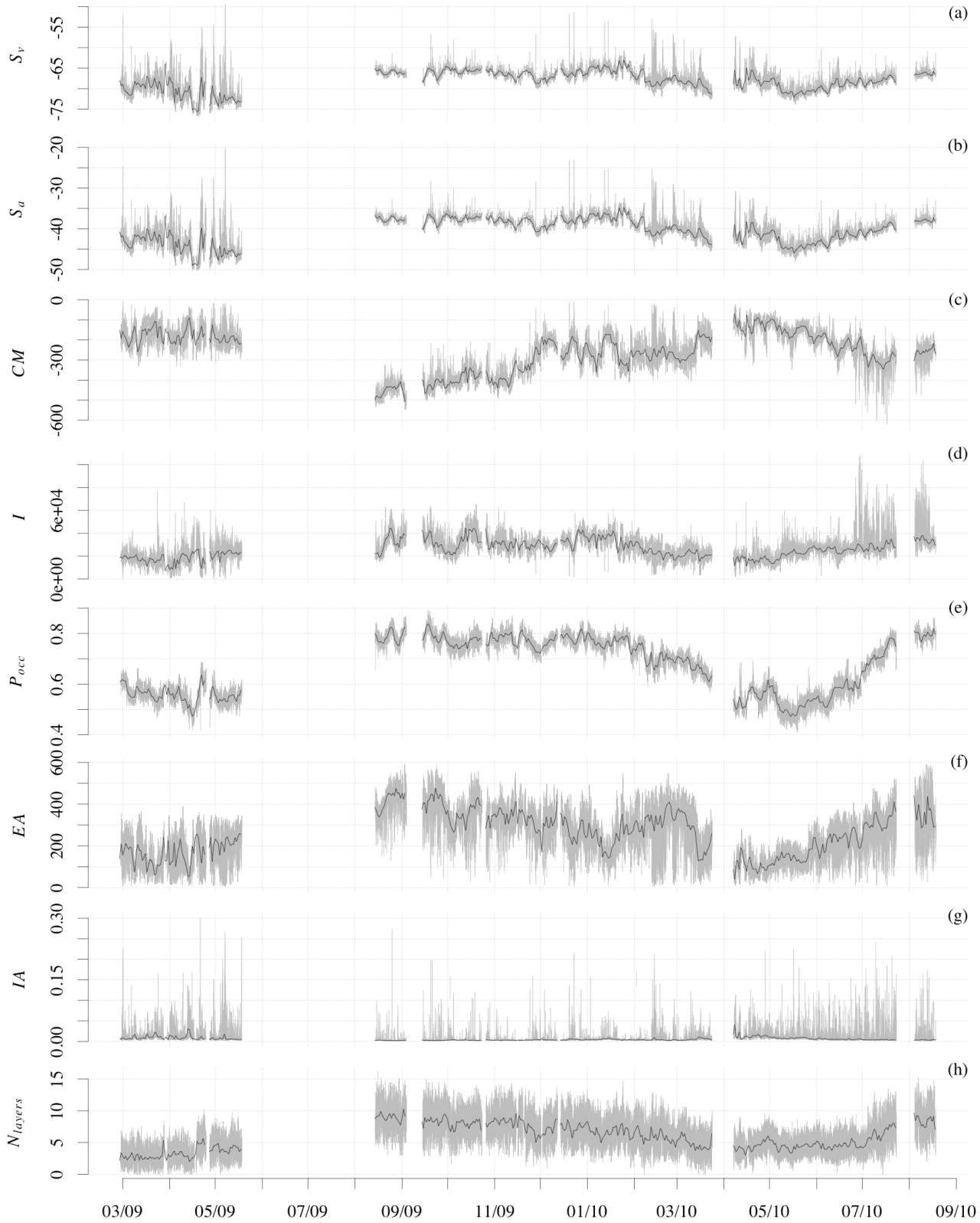

Figure 2.5: Metric time series for entire deployment (27 February, 2009, to 18 August 2010). Grey line shows values binned at 1-minute intervals; black line shows daily averages. (a) Mean volume backscattering strength, S_v, (b) area backscattering strength, S_a, (c) center of mass, CM, (d) inertia, I, (e) proportion occupied, P_{occ}, (f) equivalent area, EA, (g) index of aggregation, IA, (h) number of layers, N_{layers}. Refer to methods and Table 2.1 for calculation and details.

rics. Regressions of metric values on annual and twice-annual sinusoids (Table 2.2) were all significant ($p \ll 0.001$). Adjusted R^2 values indicated that these sinusoids accounted for between 24.6% (IA) and 87.7% (P_{occ}) of the total variability. All other series had R^2 values in between 0.474 and 0.688. Even after de-seasonalizing the series, they remained positively autocorrelated to lags between 4 and 27 days.

Variability was also present on sub-annual time scales. The Fourier and Wavelet power spectra of the de-seasonalized series had most of their energy concentrated at low frequencies (i.e. long periods/scales), with the energy appearing to decrease roughly as a power of the frequency. Power-law fits on the Fourier spectra had exponent values ranging from -1.732 to -0.8399, with R^2 values between 0.18 and 0.31 (Figure 2.6). This energy was not distributed equally through time, as shown by the wavelet spectra (Figure 2.7) . Significant energy at scales between 60 and 130 days was present during the spring of 2010 in all metrics except the index of aggregation, which reflected large changes in animal density distributions from March through June. A strong frequency component at the 30-40 day scale in S_v, S_a, and P_{occ} occurred in April 2010. Local peaks in the wavelet power were also present for most metrics at scales between 4 and 30 days, though they rarely rose to statistical significance.

Diel vertical migration (DVM) of scattering layers was observed nearly year-round, though it was not uniform through time. The power spectra of all metrics except IA had significant peaks at the 24-hour period, as well as near the 12-hour period in the CM, P_{occ}, and I spectra (Figure 2.6). Significant peaks near 12 and 24 hours were also seen in the wavelet spectra of these series, particularly during February and March in the CM and I. The strong daily oscillation in the metrics at these times is attributed to the presence of several layers migrating to the surface from depths over 300 m. The non-migrating component of the deep layer was mostly absent at these times. Significant variability was also observed in the wavelet spectra at time scales below 12 hours, predominantly during the winter for CM, EA, I, P_{occ}, and N_{layers}, and in S_a and S_v during their spring minima. During February and March of both years, dense aggregations were present near the surface during daytime, typically passing through the beam in several minutes, and registering as sharp spikes in S_a, S_v, CM, and IA.

Table 2.2: Summary of seasonal models fit to metric time series. Seasonal cycles were estimated as the sum of sinusoids with periods of one year and one-half year Table shows analysis of variance and estimated maximum and minimum values of the fitted seasonal model, with the corresponding dates.

		ANOVA					
Metric	Source	MS	$F_{4,9390}$	p	R^2	Max	Min
S_v	model	7.787×10^3	2.693×10^4	$\ll 0.001$	0.534	-70.8	-65.9
	error	2.89				Sep 10	May 5
S_a	model	1.467×10^4	4.597×10^3	$\ll 0.001$	0.662	-37.5	-44.2
	error	3.19				Sep 9	May 5
CM	model	1.681×10^7	5.167×10^3	$\ll 0.001$	0.687	-154.8	-421.5
	error	3.253×10^3				May 7	Sep 14
I	model	8.299×10^{10}	2.118×10^3	$\ll 0.001$	0.471	33,581.6	17,222.6
	error	3.918×10^7				Dec 11	Apr 11
P_{occ}	model	24.25	1.683×10^4	$\ll 0.001$	0.878	0.796	0.519
	error	1.440×10^{-3}				Sep 9	May 4
EA	model	1.627×10^7	2.976×10^3	$\ll 0.001$	0.559	408.4	145.5
	error	5.469×10^3				Sep 3	May 1
IA	model	1.651×10^{-2}	7.690×10^2	$\ll 0.001$	0.246	0.0099	0.0024
	error	2.147×10^{-5}				Apr 19	Aug 17
N_{layers}	model	7.489×10^3	3.632×10^3	$\ll 0.001$	0.607	8.57	3.56
	error	2.062				Sep 17	Apr 21

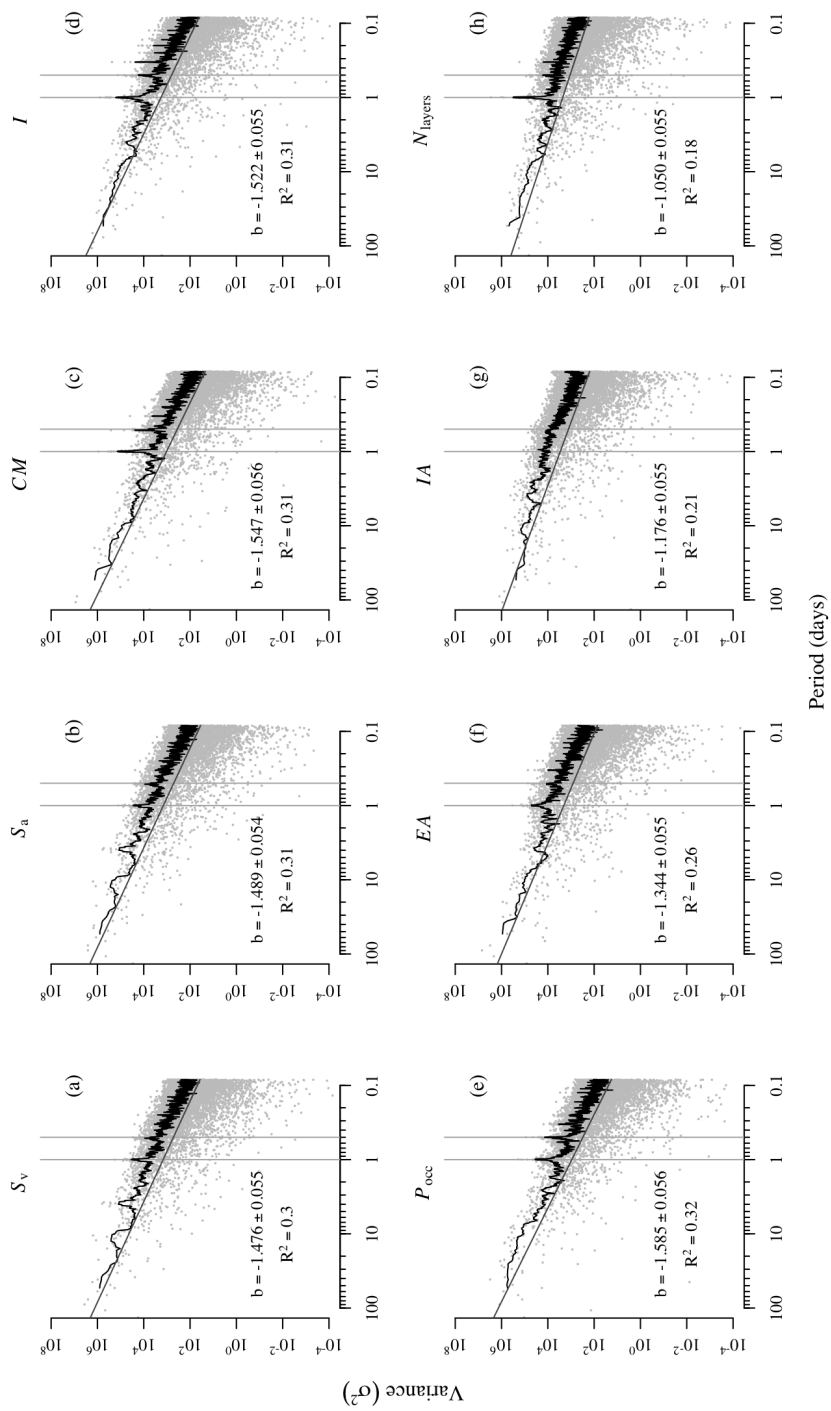

Figure 2.6: Fourier power spectra of the metrics: variance in each time series plotted as a function of frequency (log axes). Subplots are labeled as in Figure 2.5. Grey points show the raw spectra, while the black lines show the spectrum after smoothing with a 15-point modified Daniell kernel. Regression lines show power-law distributions fit to the raw spectra, with their exponents (i.e., the slope of the line on the log-log plot) and R2 values displayed as well. Vertical lines are plotted at 24- and 12-hour periods (left and right lines, respectively).

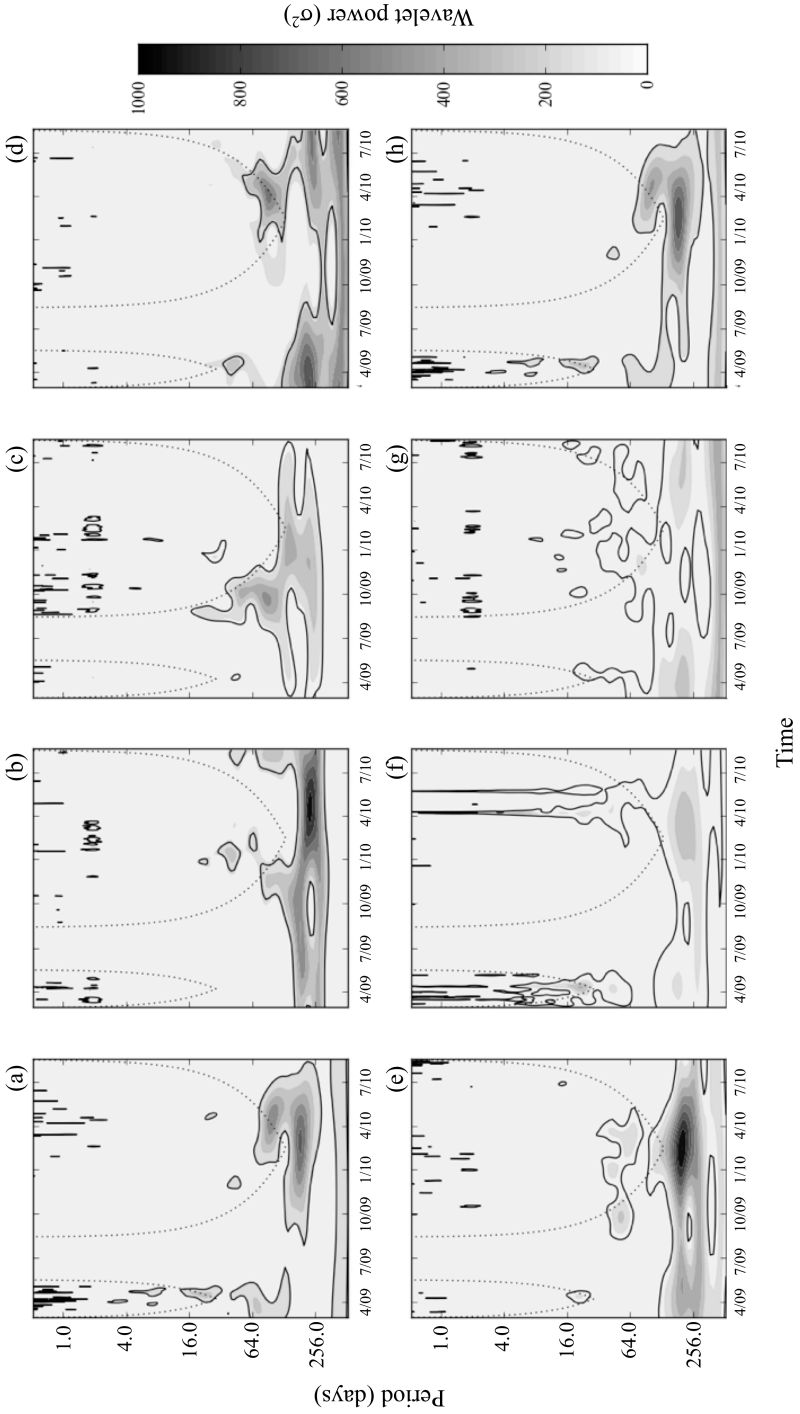

Figure 2.7: Wavelet transforms of the metric time series, plotting the variability in the series as a function of time and temporal scale. Shading indicates magnitude of the wavelet power, normalized by 1 / ?2. The thick black contour line encloses regions significant at the 95% level. Dotted lines indicate the "cone of influence:" wavelet coefficients below these lines may be reduced in magnitude by edge effects.

2.4 Discussion

The seasonal cycle observed in density distributions of animals in the water column coincided with the seasonal oceanographic cycle of Monterey Bay and the California Current. The spring backscattering minima occurred just before the "typical" peak of upwelling in June, when cool, nutrient-rich water shoals closest to the surface, with subsequent peaks in chlorophyll and primary production (Pennington and Chavez 2000). Within 3 months of its minimum, backscatter had increased an order of magnitude, with a much greater proportion of the water column occupied. This agrees with previous observations in Monterey Bay that peak zooplankton biomass lags primary production by 2-3 months (Robison et al. 1998, Croll et al. 2005). This lag is due either to the growth of these populations following the increase in food availability, or to aggregation at the upwelling front, which is located offshore early in the season but collapses shoreward in late summer (Abbot and Barksdale 1991, Robison et al. 1998, Croll et al. 2005). Interestingly, the total biomass (represented by total acoustic backscatter S_a) remained high through the winter and peaked in January, when primary production is typically close to zero (Pennington and Chavez 2000).

Seasonal movements of the boundary between the mostly-occupied upper water column and the mostly-empty lower water column also appeared consistent with the known seasonal cycle. This boundary occurred between -400 and -700 m, consistent with the upper edge of the oxygen minimum zone (OMZ) in Monterey Bay. The OMZ, usually defined as the depth zone with dissolved oxygen concentrations below 0.5 mg ml^{-1}, is located between approximately -500 and -1000 m, and moves upwards during the upwelling season (Lynn et al. 1982, Silguero and Robison 2000, Robison et al. 2010). Physiological constraints imposed by low oxygen concentrations contribute to the structure of ecological communities in the meso- and bathypelagic depth zones (Robison 2004).

Characteristics of the frequency spectra suggested that fluid turbulence influences the temporal variability of pelagic fauna. The spectrogram slopes of *CM*, *I*, P_{occ}, S_v, and S_a all fall near the theoretical value of -5/3 for diffusive turbulent mixing (Platt and Denman 1975, Kolmogorov 1941), and power-law distributions provided good fits to these empirical spectra. These observations indicate that the total abundance, mean vertical location, and dispersion of animals in the water column

vary as the velocities of passively-drifting particles. In contrast, the variance of *IA* and N_{layers} decays more slowly with increasing frequency. The temporal variability of these metrics, both measuring aggregation, is not consistent with passive-particle variability, suggesting that midwater animal assemblages are mobile and choose to aggregate independent of fluid motions. This finding is consistent with other observations of mobile aquatic organisms' distributions (Horne and Schneider 1994).

Considerable variability was also present at short time scales. In particular, there were significant frequency components in all metrics but the *IA* with a period of 24 hours, corresponding to the diel cycle. Significant variability at a near-12-hour period was also present in the *CM* and P_{occ} indices, likely due to movements of animals by tidal currents . Diel variability was more pronounced in location and dispersion metrics than in those indexing total abundance and density. This contrast is expected if DVM is primarily vertical. The fact that S_a and S_v displayed energy peaks at the 24-hour period indicates some cyclic variability in total abundance and density at this temporal scale. Variability at this scale could be due to changes in acoustic target strength as animals change orientation during DVM (Foote and Ona 1987, Simard et al. 2009), or to a horizontal component in the diel migration cycle (e.g, Benoit-Bird and Au 2004).

Because we did not conduct direct sampling, we cannot positively identify the organisms observed from DEIMOS. Monterey Bay has been sampled for a number of decades, and we can infer species compositions from published literature. Barham (1956), in the first acoustic study of the Bay's ecology, identified the main constituents of acoustic backscatter layers as myctophid fish (*Diaphus theta* and *Lampanyctus leucopsarus*), and to a lesser extent mesopelagic shrimp (*Sergestes similis*) and Pacific krill (*Euphausia pacifica*). Later studies, including visual observations from remotely-operated vehicles (ROVs), have shown that layers are mixed-composition (Robison 2004, Robison et al. 2010), and as much as a quarter of the pelagic biomass is gelatinous (Robison, 2004). Of particular note are organisms such as the siphonophore *Nanomia bijuga*, a common gelatinous predator that is also a strong acoustic target due to its gas-filled pneumatophore (Barham 1963, Holliday and Pieper 1980, Robison et al. 1998). ROV observations show that *Nanomia* undergoes a seasonal cycle in abundance lagging primary productivity by about 3 months, with peak densities occurring near 500 m depth (Robison et al. 1998). Single targets in the region below the backscattering layers are likely macrourids

and other fish (Yeh and Drazen 2011). Future studies using stationary acoustics would benefit from the addition of direct sampling, as well as additional acoustic frequencies, allowing better discrimination of different types of scattering organisms (Horne 2000).

Vertically applied spatial metrics other than S_v and S_a are relatively uncommon in fisheries acoustics. A more typical approach would be to divide the water column into layers of interest and track the mean density or total backscatter within each of these layers. This was the approach taken by Flagg et al. (1994) and Cochrane (1994) to add detail to the basic backscattering statistics. Burgos and Horne (2008) rigorously investigated a wide range of metrics to characterize walleye Pollock (*Theragra chalcogramma*) aggregations in the Bering Sea, arriving at a similar set to that used in this paper. The suite of metrics presented here effectively captures the vertical density distribution, rendering a large dataset into tractable form, and provides a flexible set of tools to quantify variability in the ecosystem.

While the metrics do not measure compositional variability (i.e. changes in the abundance of different taxa) they do provide a powerful, high-scope view of aggregate variability (i.e. changes in the overall abundance or density; cf. Micheli 1999). As demonstrated by the PCA, considerable colinearity exists between metrics—as would be expected, given the mathematical relationships between them (Bez and Rivoirard 2001, Woillez et al. 2007). Because they are calculated over the entire water column, they can integrate distinct features. For instance, the signature of diel variability due to vertical migration in the upper water column was damped in the metrics by the presence of the deep non-migratory layer. The *CM* and *I* indices both assume a single center, but the vertical density distribution was typically multi-modal, with several distinct layers. Depending on the process or region of interest, the metrics could be constrained to specific regions in the water column.

The metrics presented in this study effectively described animal density in the water column, and are capable of measuring periodic variability (such as DVM), long-term shifts (such as interranual changes), and transient events such as the occurrence of dense aggregations. These phenomena are important when characterizing ecosystems, and could be used to detect potential changes associated with climatic trends. Metrics used in this study could be extended and applied in two or three spatial dimensions as succinct descriptors of density distributions through

time. The metrics are well-suited to pattern description in high-scope data series: they are objective, simple to calculate, retain full resolution in the indexing dimension (i.e. time), and provide a description of the vertical density distribution with a minimum of assumptions. Other applications potentially include unsupervised monitoring of a data stream or as preliminary indicators of data quality.

Long-term, continuous sonar records can be used to address ecological questions, offering a powerful tool to monitor an ecosystem at multiple trophic levels (Koslow 2009). Diel vertical migration is an obvious process to investigate with stationary acoustics, but appropriately-located acoustic instruments could also be used to observe the timing of horizontal migrations, either on short (diel) time scales (Benoit-Bird and Au, 2004) or longer scales for more mobile organisms (Kaltenberg et al. 2010). When combined with oceanographic observations, stationary acoustics facilitates investigation of bio-physical coupling through the water column across temporal scales. Stationary acoustics could also be used to complement ship-based surveys for resource management if methods for temporally-based stock assessment are developed (cf. Brierley et al. 2006).

This study has developed and tested a suite of metrics for characterizing vertical distributions of pelagic fauna in large acoustic datasets such as those from acoustic observatories. Applying the metrics to data from an 18-month deployment of an upward-looking echosounder in Monterey Bay illustrated their ability to capture cyclical changes at seasonal and daily scales, and to quantify the distribution of variability across a wide range of temporal scales. Variability in the pelagic fauna of Monterey Bay is largest over long periods, particularly during the pronounced drop in S_a during the spring upwelling season. It is hoped that these metrics will prove a useful tool in future deployments of active acoustics at ocean observatories.

3.

RESPONSE OF MICRONEKTON TO ENVIRONMENTAL VARIABILITY

3.1 Introduction

Animals in the ocean's pelagic zone must survive in a fluid ecosystem that varies in space and time. The physical and chemical properties of seawater determine, directly or indirectly, the habitat of all marine life. These properties vary over a wide range of spatial and temporal scales (Stommel 1963), and in turn, the abundance and density of pelagic animals vary across a similarly wide range of scales (Haury et al. 1978). This biological variability is generated by a variety of mechanisms, including animal behavior, ecological interactions, and population dynamics. It is also generated and influenced by physical variability. Because the ocean's physical medium varies at the same range of scales as its biological processes (Steele 1978) and can strongly affect them, understanding the links between ocean physics and biology has long been recognized as central challenge in oceanography and marine ecology. The physics of the ocean affect its biology directly and indirectly. Direct effects include the transport, aggregation, and dispersal of organisms by fluid motion. Indirect effects include, for example, the upwelling or mixing of nutrients into the photic zone, fertilizing a phytoplankton bloom. Such physically-mediated blooms in turn fuel the rest of the pelagic food web, supporting secondary production and attracting larger animals, such as fish, birds, and marine mammals.

In order to reach these predators at the upper trophic levels, production must first pass through the broad assemblage of animals at the middle trophic levels. This

group includes shrimp, krill, myctophids, squid, and others, and is sometimes referred to collectively as "micronekton" (Brodeur and Yamamura 2005). This group cannot swim strongly against currents, but many species within it undergo diel vertical migrations (DVM) of up to several hundred meters to feed at the surface at night. They are thus important carriers of energy and nutrients, both down the water column, by migration and excretion, and up the food chain, through predation. Their distribution and abundance are also affected directly and indirectly by physical variability: directly, due to their relatively weak swimming ability, and indirectly, due to the potentially ephemeral nature of the pelagic production they feed on.

Because the ocean is variable at all scales, measurements that are not high-scope (i.e., with high resolution over a long extent, Schneider 2009) may not be able to resolve important patterns of variability. Measurements of temporal variability in the density of aquatic organisms are less common than measurements of their spatial variability. Moored instruments and satellites provide long-term, high-resolution estimates of many physical, and a few biological, variables, but measurements of animal density with similar scope have been relatively few. This dearth of high-scope time series for animal density may represent a significant gap in our understanding. The goal of this study was to gain a clearer picture of the direct and indirect influences of physical ocean processes on the mid-trophic levels in outer Monterey Bay, California, by quantifying the relationships between long-term, high-resolution time series of physical and biological variables.

Monterey Bay is located in the California Current, one of the world's major eastern-boundary currents. As with other eastern-boundary currents, Ekman pumping driven by seasonal equatorward-flowing winds brings nutrient-rich water to the surface near the coast, fueling a highly productive ecosystem. Though limited in area, upwelling systems support a disproportionate amount of global fisheries landings (Pauly and Christensen 1995) and attract large predators from great distances (Block et al. 2011). The seasonal cycle of upwelling and productivity in the California Current is generally consistent (Pennington and Chavez 2000), but within a given year upwelling is irregular, supplying nutrients to the food web in episodic pulses. Upwelling is also spatially variable. Mesoscale squirts, jets, eddies, and coastal waves all introduce variability into the movement of water (Keister and Strub 2008). The response of phytoplankton to environmental variability has been

investigated in a number of studies over the years at both interannual (McGowan et al. 2003), seasonal (Bolin and Abbot 1963, Service et al. 1998), and sub-seasonal time scales (Service et al. 1998, Legaard and Thomas 2008). The environment's effects on the mid-trophic levels of the California Current have also been studied, though not to the same extent as with phytoplankton. Most of this work has been conducted at seasonal and interrannual time scales (Brinton and Townsend 2003, Jahncke et al. 2008). Sampling at these time scales illuminates seasonal population changes, as well as longer-term changes such as those associated with El Niño and decadal climate shifts, but does not resolve dynamics at shorter temporal scales relevant to animal feeding, reproduction, and movement.

We were interested in the response of Monterey Bay's pelagic fauna to sub-seasonal oceanographic variability, including upwelling events and their associated phytoplankton blooms. We used a bottom-mounted scientific echosounder to estimate animal biomass through the water column, and used wind, temperature, and fluorescence data from a nearby data buoy as proxies of upwelling. In addition, we examined sea level, measured at a tide gauge in Monterey, to investigate possible links between sea-surface topographic features and animal biomass (e.g. Clarke and Dottori 2008). We used a time-series analytic approach to detect and characterize biological responses to environmental forcing, considering both direct, kinematic responses, and indirect, biological responses (i.e., growth and reproduction following periods of increased primary production). Backscatter was expected to increase at some time lag following upwelling events, due to a combination of aggregation, somatic, and population growth. In addition, we examined how these responses varied as a function of depth. The response of animals at depth to increased productivity at the surface was expected to be delayed and damped when compared to the response of surface animals. Finally, we used biological reasoning and knowledge of Monterey Bay's pelagic fauna to speculate on the processes generating the observed physical-biological relationships.

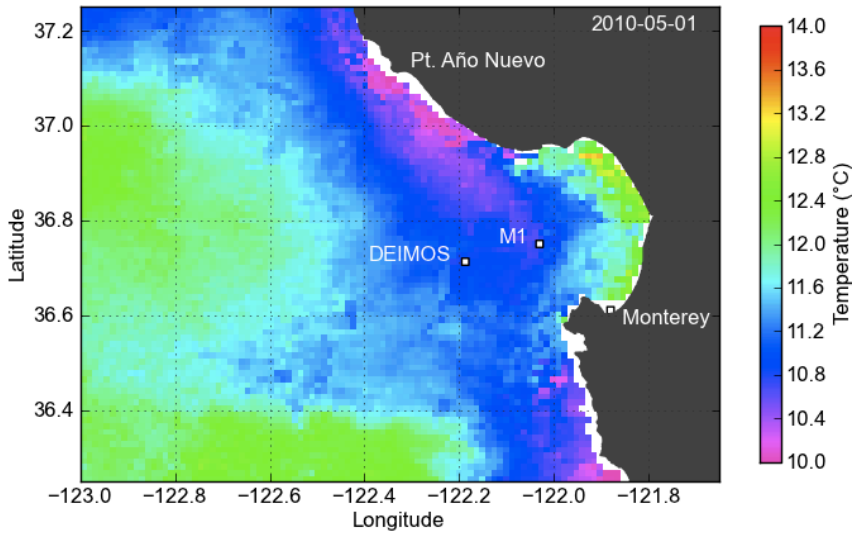

Figure 3.1: Monterey Bay, showing location of instruments and a typical pattern of sea-surface temperature during the upwelling season (AVHRR 3-day composite, 1 May, 2010). A band of cold, upwelled water is located along the coast, with warmer water offshore and inside the Bay. The coldest waters are near Point Año Nuevo and Point Sur.

3.2 Methods

3.2.1 Study location

Monterey Bay is a large, open embayment in the central California coast. The Bay's bathymetry is mostly shallow (< 100 m), but is bisected by the Monterey Submarine Canyon, which brings deep-water habitat close to shore and may facilitate nutrient supply to the photic zone through tidal mixing or the breaking of internal waves (Ryan et al. 2005). The Bay's oceanographic seasons mirror those of the larger California Current , with wind-driven upwelling in the spring and early summer, a warm water "oceanic period" in the late summer and fall, and a winter downwelling or "Davidson current" period (Skogsberg and Phelps 1946, Pennington and Chavez 2000). Point Año Nuevo, to the north of the Bay, is the source of a persistent upwelling plume that typically trails south across the mouth of the Bay (Rosenfeld et al. 1994, Figure 3.1). Mean circulation within the bay is counterclockwise, with enhanced productivity in the "upwelling shadows" near shore (Graham et al. 1992).

3.2.2 Acoustic Data

Animal density was estimated through the water column using a bottom-mounted echosounder. The Deep Echo Integrating Marine Observatory System (DEIMOS) is an acoustic package built around a 38 kHz scientific echosounder (Horne et al. 2010). It was deployed at 875 m depth from February 27, 2009 to August 18, 2010 at the Monterey Accelerated Research System (MARS), a cabled observatory node, located at 36° 42.748' N, 122° 11.214' W on Smooth Ridge, to the north of the Canyon. MARS is maintained and operated by the Monterey Bay Aquarium Research Institute (MBARI), and provides continuous power and communications for scientific instruments. DEIMOS sampled continuously at 0.2 Hz with a 0.5 m vertical resolution through the full water column. DEIMOS was calibrated *in situ* using a standard target (Foote et al. 1987) hung from a float above the transducer during the final 7 weeks of the deployment. We were not able to take direct samples to identify sound-scattering organisms, and therefore used acoustic area backscatter (s_a, MacLennan et al. 2002) as a proxy of animal biomass. This is a reasonable assumption for both single species (Foote 1983) and mixed communities (Benoit-Bird and Au 2002).

Acoustic data were processed using Echoview software (version 4.8, Myriax Pty. Ltd. 2010). Background noise was estimated and subtracted using the methods described in De Robertis and Higginbottom (2007). An acoustic threshold was applied to eliminate returns with volume-scattering strengths below -90 dB, the approximate target strength of an individual krill at 38 kHz (Demer and Conti 2003). All echograms were visually inspected, and regions with external noise (e.g. ship or ROV noise) were excluded from further analysis. Also excluded were the regions within 7 m of the bottom, to eliminate targets in the acoustic near field, and within 10 m of the surface, to avoid integrating bubbles from breaking waves. The mean depth of backscatter was measured using the acoustic center of mass (*CM*, Chapter 2). We also integrated acoustic backscatter in three depth zones, based on biological reasoning and persistent features of the echogram. We defined the euphotic zone from 0-50 m, representing the area where most primary production takes place (Pennington and Chavez, 2000). The epipelagic zone was defined from 50-300 m, where scattering layers consistently underwent DVM to the surface. The mesopelagic zone encompassed the water column from 300-875 m, where vertical migration was limited and a large, non-migrating layer was present nearly year-

round above a region of low backscatter with sparse single targets.

3.2.3 Oceanographic Data

Time series of wind velocity, sea-surface temperature (SST), and fluorescence, a proxy for chlorophyll, were measured at MBARI's M1 data buoy, located 15 km ENE of DEIMOS at 36° 45′ N, 122° 1.8′ W (Chavez et al. 1997, Figure 3.1). Service et al. (1998) found that wind velocity at M1 was highly correlated (R^2 = 0.78) with wind velocity at MBARI's M2 mooring, 18 km WSW of DEIMOS. The strong correlation held during our study period (R^2 = 0.73), indicating that winds at M1 are representative of those at DEIMOS, located approximately midway between M1 and M2. Daily satellite measurements of SST and log chlorophyll-a at DEIMOS and M1, from Level-3 AVHRR and MODIS-Aqua imagery, were also correlated (R^2 = 0.86 and 0.37), giving us confidence that SST and fluorescence at M1 are representative of these quantities over DEIMOS.

Ekman transport of water offshore, an estimate of wind-driven upwelling, was calculated from wind measurements at M1 following Bakun (1973). The offshore Ekman transport was estimated as $M_E = \tau_a / f$, where τ_a is the alongshore component of the wind stress and f is the Coriolis acceleration, equal to 8.326×10^{-5} s^{-1} at latitude 36° 45′ N. Wind stress was calculated as $\boldsymbol{\tau} = \rho C_d |\mathbf{u}| \mathbf{u}$, where $\mathbf{u}$ is wind velocity, ρ is the density of air (assumed constant at 1.22 kg m^{-3}), and C_d is a non-dimensional drag coefficient, taken to be 0.0013 (Bakun 1973, Schwing et al. 1996). Alongshore wind stress was defined as the component parallel to 150°, with positive stresses towards the southeast. Sea level was measured by the National Oceanographic and Atmospheric Administration (NOAA) tide gauge in Monterey (http://tidesandcurrents.noaa.gov/geo.shtml?location=monterey) tides, and low-pass filtered with a 25-hour moving average to remove the effects of diurnal and semidiurnal tides.

3.2.4 Analysis

Prior to analysis, values in all time series were averaged in one-day bins. Since we were interested in sub-seasonal dynamics, the seasonal cycle was estimated and removed by fitting sinusoids with periods of 6 and 12 months to the data by least squares. All further analysis used the residuals from these fits. Gaps were present

in all series but the SSH, due to technical problems interrupting data acquisition and scheduled instrument maintenance. Where gap-free series were necessary for statistical analyses, we filled missing values using a stochastic gap-filling procedure (Percival et al. 2008). Briefly, the empirical autocorrelation function (ACF) of the series was used to predict the missing values conditional on the values to either side of each gap. The ACF was then used to simulate a realization of a random process with the same autocorrelation structure as the rest of the series on top of the predicted values. The desired analysis was conducted for 500 of these simulations, and the mean value used.

Correlations between time series were investigated as a function of time lag h using cross-correlation functions (CCFs). We considered only the half of the CCF where the oceanographic variable led the acoustic variable, since our questions focused on the influence of oceanography on micronekton. This is consistent with "bottom-up" forcing, from physics to primary production and consumption, usually assumed to operate through lower trophic levels (cf. Micheli et al. 1999). Assuming an uncorrelated white-noise null hypothesis, CCFs were considered significant if their absolute value was greater than $z_{0.975}/\sqrt{n}$, where $z_{0.975}$ is the 0.975 quantile of the standard normal distribution and n is the number of observations in each time series (Brockwell and Davis 2002). We calculated CCFs of wind stress with fluorescence and temperature to check the time lag of phytoplankton blooms behind upwelling events. We then calculated the CCFs of s_a (whole-water-column and 3 depth zones) and the *CM* with upwelling, temperature, and fluorescence.

Cross-correlation analysis assumes that the two time series are jointly stationary, which may not hold for series including transient features such as upwelling events. To address the possibility of non-stationary bio-physical coupling, we used continuous cross-wavelet analysis (Torrence and Compo 1998, Maraun and Kurths 2004). In univariate wavelet analysis, a time series is convolved with a localized waveform, the wavelet, scaled to different frequencies. The product is the wavelet spectrum, an array of complex wavelet coefficients, $W(s,\ t)$, as a function of scale s and time t. The wavelet power, representing the variability in the time series at time t and scale s, is given by $|W(s,\ t)|^2$. If W_1 and W_2 are the wavelet transforms of two time series, the cross-wavelet coherence is $|W_1\ W_2^*|\ /\ (W_1^2\ W_2^2)^{1/2}$, where * denotes the complex conjugate. The wavelet coherence ranges from 0 to 1, and represents the correlation of the two series as a function of time and scale. Before calculat-

ing the coherence, the nominator and denominator must be smoothed separately; if not smoothed, they equal each other and the coherence is equal to 1 everywhere (Maraun and Kurths 2004). We used a 7×15 pixel (time $\times$ scale) moving-average window.

A fourth-order derivative-of-Gaussian (DOG) or Mexican hat wavelet was used for our analyses. The DOG wavelet is localized in time with a large central peak, making it appropriate for aperiodic events such as upwelling. The cross-wavelet power was tested for significance at the 95% level using a Monte Carlo approach. We tabulated the wavelet coherencies for 1000 simulated realizations of the time series, generated by taking Fourier transforms, randomizing the phase, and then back-transforming. The wavelet coherence was considered significant where its value was greater than 95% of the simulated coherence spectra. Wavelet coherencies were calculated between the four environmental series and s_a, both overall and in each of the three depth zones.

As a test of the predictive power of the bio-physical relationships, we built a statistical model for backscatter in the top 300 m of the water column, representing prey available to surface-diving and epipelagic predators. We regressed the logarithmic form of area backscatter (S_a) on the values of the four environmental variables at their best-correlated lag below 30 days, selecting significant covariates using a backwards-deletion procedure. An autoregressive (AR) model accounted for autocorrelation in the residuals. We computed the corrected Akaike information criterion (AICc, Hurvich and Tsai 1989) for AR models using from 0 to 15 AR terms, selecting the model with the lowest score. This procedure optimizes the tradeoff between a model's goodness-of-fit and the number of parameters estimated (Akaike 1974). Parameters were fitted by maximum likelihood, using a state-space representation of the AR process (Jones 1980). Residuals were tested for autocorrelation using the Ljung-Box test (Ljung and Box 1978).

3.3 Results

3.3.1 Oceanography and primary productivity

Weather and oceanography followed a typical annual cycle for Monterey Bay (Figure 3.2). Northwesterly winds and alongshore wind stress were strongest in the

early spring, co-occurring with low sea-surface temperatures and high fluorescence. The sea-surface height anomaly was lowest in April and May. Over shorter time scales, fluorescence was negatively correlated with SST, with the highest correlation found at a lag of 3 days (Figure 3.3). These results are similar to those of Service et al. (1998), who found that the lagged correlation between fluorescence and temperature peaked at 4 days. Fluorescence displayed a characteristic scale of variability between 10 and 20 days, representing the average time between upwelling events and corresponding phytoplankton blooms. Sea level also showed semi-periodic fluctuations with a period of approximately 20 days. These fluctuations were somewhat correlated ($\rho = -0.45$) with alongshore wind stress at lags of 1 day (Figure 3.3).

3.3.2 *Bio-physical coupling in micronekton*

The seasonal cycle of backscatter was out of phase with that of primary production. Backscatter was lowest in May of both years of the deployment, coinciding with the lowest temperatures and highest fluorescence. Backscatter was highest in the fall and winter, peaking in September. This observation agrees with previous measurements in Monterey Bay, from an ADCP on the M1 mooring (Croll et al. 2005). During its spring minima, backscatter moved up in the water column, with its center of mass near 150 m.

The density of pelagic fauna was also related to oceanographic variability at sub-seasonal time scales. Total backscatter had weak but significant negative correlations with indicators of upwelling (alongshore wind stress, below-average SST and above-average fluorescence) at lags less than 20 days (Figure 3.4). The correlation of backscatter with fluorescence reached a positive maximum of 0.12 at a 48 day lag. The strongest effect of upwelling on the distribution of micronekton occurred in the *CM*, which was negatively correlated with SST at lags from 0 to 85 days. The minimum correlation (ρ = -0.23) occurred at 14-15-day lags. The *CM* was also negatively correlated with fluorescence at lags between 0 and 18 days, though not as strongly as with temperature. These correlations indicated that the total abundance of micronekton decreased slightly over one to three weeks following upwelling events, while moving up in the water column.

Micronekton abundance was best correlated with sea level. Cross-correlation of total backscatter with sea level was highest (ρ = 0.31) at a lag of 1 day and had

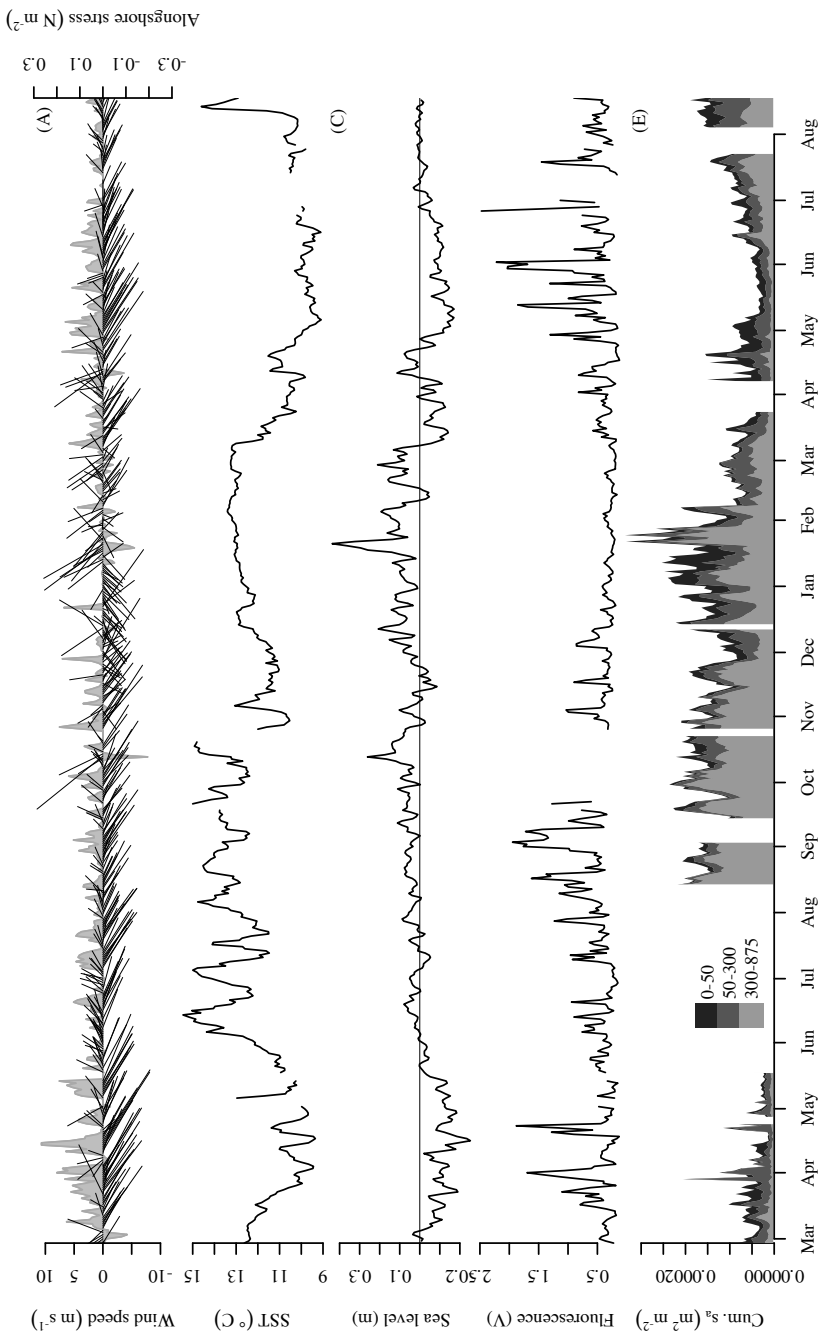

Figure 3.2: Oceanographic and biological time series from 27 February, 2009, to 18 August, 2010. A) Wind. Vectors show direction and magnitude (left axis), grey area shows alongshore wind stress (right axis). B) Shows sea-surface temperatures, C) shows fluorescence, and D) sea level anomaly. E) Acoustic backscatter, divided into surface (0-50 m), epipelagic (50-300 m), and mesopelagic (300-875 m) zones.

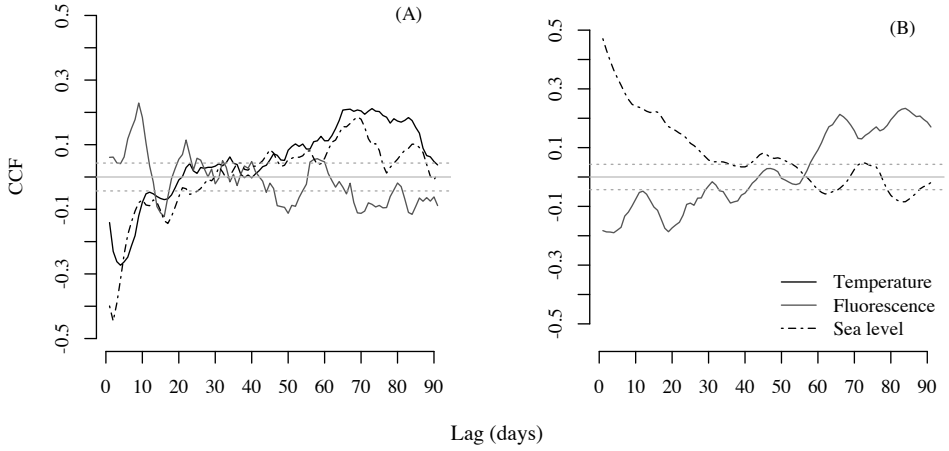

Figure 3.3: Cross-correlations between environmental series. A) Lagged correlations of SST, sea level, and fluorescence with alongshore wind stress. B) Lagged correlations of sea level and fluorescence with temperature.

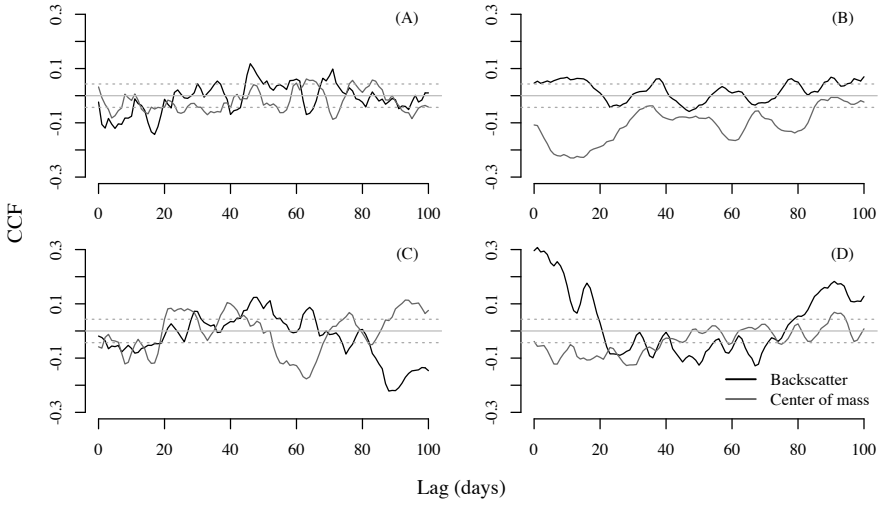

Figure 3.4: Cross-correlations between acoustic and environmental series. Each plot shows lagged correlation of total backscatter (black line) and its mean location in the water column (the center of mass, blue line) with A) alongshore wind stress, B) SST, C) Fluorescence, and D) sea level.

a second peak (ρ = 0.18) at 16 days. The center of mass was negatively correlated with sea level at lags from 0 to 38 days. Together, these correlations indicated that above-average sea levels were associated with increased backscatter deeper in the water column at short lags.

Wavelet coherencies between backscatter and environmental variables were consistent with cross-correlation results. All cross-spectra showed intermittent regions of significant coherence at the shortest scales, from 2-8 days (Figure 3.5). There was also an intermittent band of significant coherence at scales between 8 and 32 days, which was more distinct in the cross-spectra of backscatter with wind stress and with fluorescence. Coherence in this band was also present in the cross-spectra with temperature and sea level, but was spread across a wider range of scales and was not as well separated from the short-term coherence. This "mesoscale" band corresponded to variability approximately at the same scale as upwelling and sea level fluctuations. At longer scales, above approximately 64 days, backscatter was significantly coherent with wind, temperature, and sea level, though not with fluorescence.

The response of pelagic fauna to environmental variability also varied as a function of depth (Figure 3.6). There was no obvious relationship of backscatter in the three zones to wind stress. The surface (0-50 m) and epipelagic (50-300 m) zones were negatively correlated with SST at lags from 5-25 and 2-31 days, while the mesopelagic (300-875 m) zone was positively correlated with SST across a similar range of time lags. This result appears to reflect the concentration, noted above, of animals in the upper water column following the surface expression of cool, upwelled water. The response of micronekton to fluorescence also varied with depth. At lags between 30 and 70 days, we observed the hypothesized depth-dependent bio-physical coupling. At a lag of 38 days, correlation between fluorescence and surface backscatter peaked (ρ = 0.097), followed by the epipelagic zone (ρ = 0.130) at a 48 day lag, and then the mesopelagic zone (ρ = 0.155) at a 64 day lag.

When considered by depth zone, sea level had a strong influence on the distribution of backscatter. All depth zones had significant positive correlations with sea level at lags below 10 days. The strongest of these relationships was in the mesopelagic, which had its peak correlation (ρ = 0.265) at a 6-day lag, with a secondary peak at 16 days. The surface zone had a similar correlation structure, but weaker, with a maximum (ρ = 0.137) at 4 days.

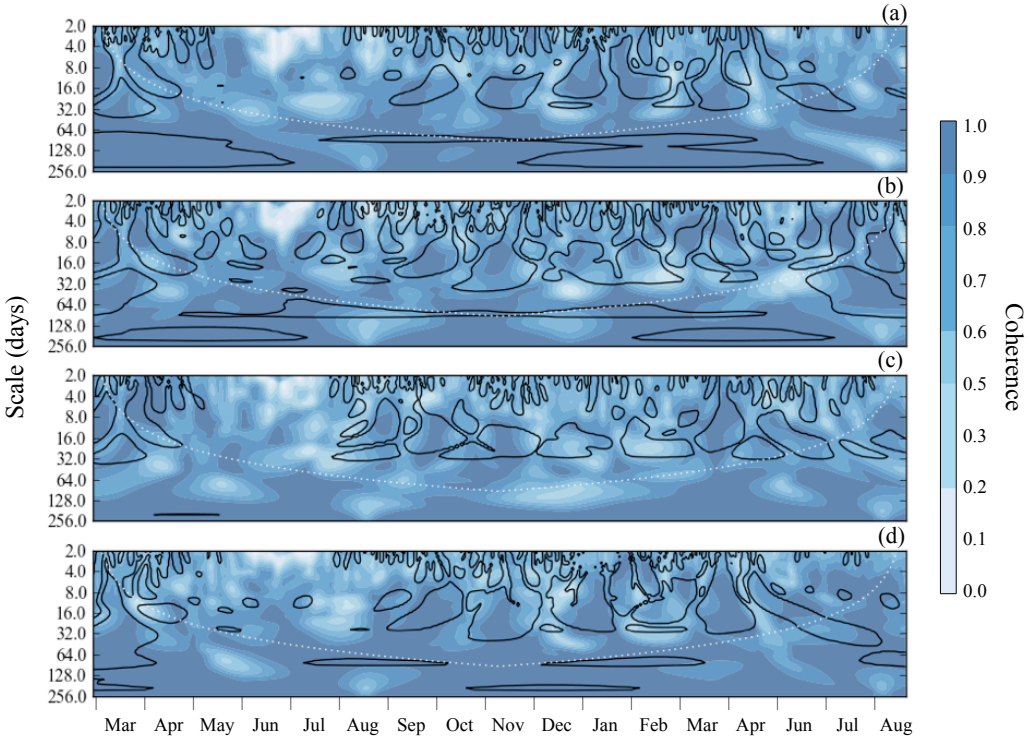

Figure 3.5: Cross-wavelet analysis of total backscatter and A) alongshore wind stress B) sea-surface temperature, C) fluorescence, and D) sea level. Coherence between each pair of series (color) is shown as a function of scale (y-axis) and time (x-axis). The black contour outlines regions significant at the 0.05 level. The white dotted line indicates the "cone of influence": values below the line (i.e., at higher scales) may be subject to edge effects.

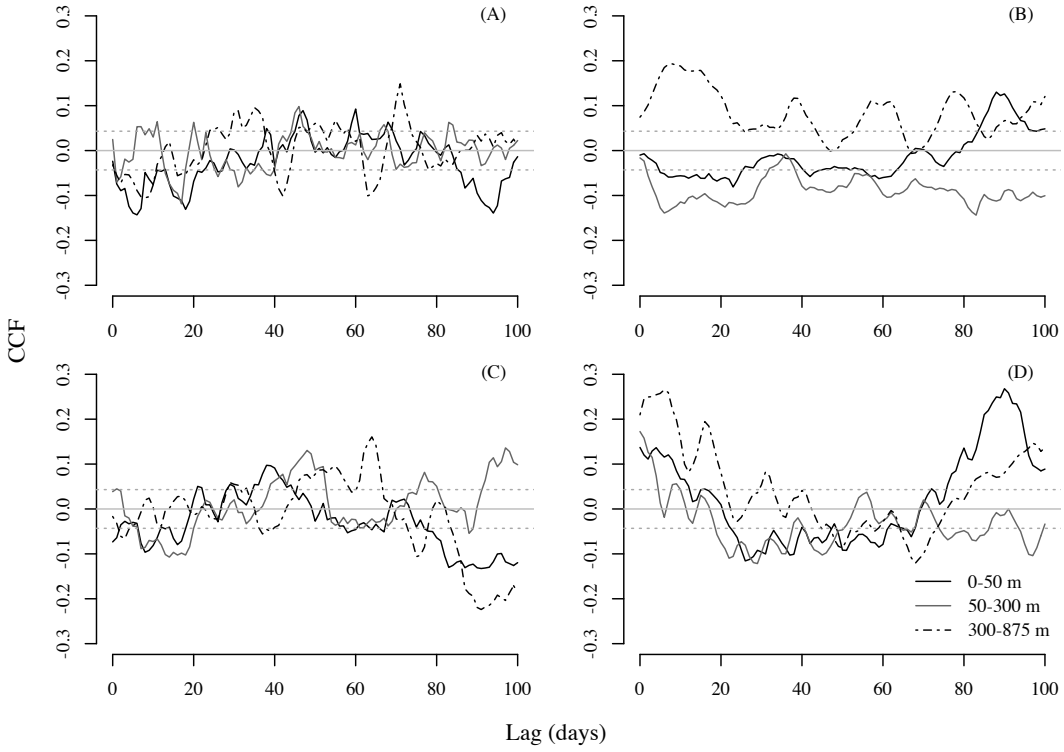

Figure 3.6: Cross-correlations between environment and backscatter in depth zones. Each plot shows lagged correlation of euphotic (black line), epipelagic (grey line), and mesopelagic (dashed line) backscatter with A) alongshore wind stress, B) SST, C) Fluorescence, and D) sea level.

Table 3.1: Parameter estimates, standard errors, and units for model of backscatter (dB re. 1 m^2 m^{-2}) in the upper 300 m of the water column: α_1 is the regression coefficient for wind stress, α_2 is the regression coefficient for sea level, and ϕ_h is the autoregressive coefficient at lag h.

Parameter	α_1	α_2	ϕ_1	ϕ_2	ϕ_3	ϕ_4	ϕ_5	ϕ_6	ϕ_7
Estimate	7.336	-8.170	0.657	-0.055	0.120	0.025	-0.018	-0.200	0.252
St. Error	2.036	1.447	0.050	0.062	0.062	0.066	0.064	0.062	0.051
Units	dB m^{-1}	dB m^{-1}	-	-	-	-	-	-	-

Cross-wavelet analysis by depth zone revealed similar patterns as the full-water-column analysis, but with slight differences by depth. A distinct "mesoscale" coherent band was only present in the mesopelagic (300-875 m) zone (Figure 3.7). This band was particularly well-defined in the cross-spectra of backscatter with wind stress and fluorescence. In the upper two depth zones, coherent energy was present at these scales (i.e., 8-32 days), but was not separated clearly from coherent regions at shorter scales. Notably, coherence between backscatter and sea level was spread across scales from 2-32 days in all three depth zones. Coherence at scales above 64 days was most obvious in the wind and temperature cross-spectra in the upper two depth zones (i.e. above 300 m).

For the regression model of micronekton in the upper 300 m of the water column, wind stress and sea level were significant ($p < 0.05$) predictors of backscatter above 300 m. The AICc procedure selected a model incorporating these covariates and seven past values of backscatter (Table 3.1). The model's one-step-ahead prediction errors were uncorrelated (all Ljung-Box p-values greater than 0.8), with an error variance of 1.57 (dB re. 1 m^2 $m^{-1})^2$. In the simple linear regression with no autoregressive terms, wind and sea level explained 8% of the variability. The addition of seven autoregressive terms improved the R^2 value to 53%.

3.4 Discussion

3.4.1 Response of micronekton to sea level

Of the variables examined, sea level had the strongest and most immediate correlation with acoustic backscatter. This correlation was present through the water column, and suggests that direct, kinematic effects are the most important physical

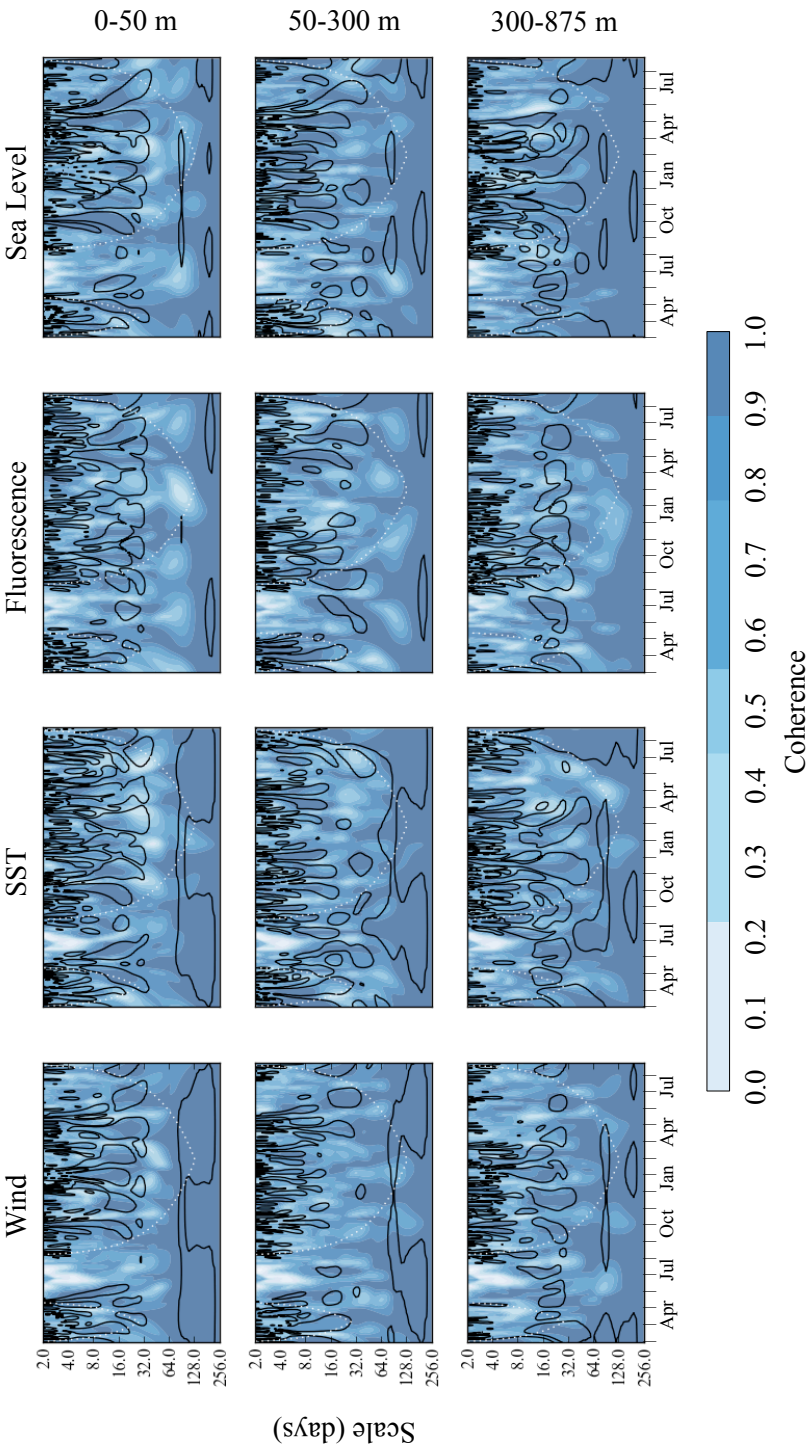

Figure 3.7: Cross-wavelet analysis of coherence between environmental series and backscatter in three depth zones. The depth zones are arranged in the rows, the environmental covariates in columns. Coherence (color) is plotted as a function of scale (y-axis) and time (x-axis). The black contour outlines regions significant at the 0.05 level. The white dotted line indicates the "cone of influence": values below the line (i.e., at higher scales) may be subject to edge effects.

processes affecting the density of micronekton on short time scales. Variation in coastal sea level is caused by a number of different processes, acting across a wide range of temporal scales. At the temporal scales considered here, these processes included atmospheric pressure, wind-driven upwelling, and coastally-trapped waves (Chelton and Enfield 1986).

Weather affects coastal sea level through two mechanisms. Changes in local atmospheric pressure force a static response in sea level, known as the "inverted barometer" effect, amounting to approximately 1.01 cm rise per 1 mbar drop in air pressure (Chelton and Enfield 1986). Wind affects coastal sea level through Ekman transport perpendicular to the coast. When winds are northerly in the California Current, the surface layer moves offshore, causing upwelling and lowering the coastal sea level. The reverse occurs when winds are from the south. Both the inverted barometer and wind effects cause near-immediate changes in sea level, varying on the order of 10-20 cm over a period of days with the passage of weather systems. Both effects were detectable during this study: alongshore wind stress was negatively correlated with sea level at zero lag, as was atmospheric pressure (R^2 = 0.57).

In addition to local meteorological forcing, coastal sea level varies with the passage of coastally trapped Kelvin waves. These waves propagate northward along the California coast. They may be excited locally by wind or pressure perturbations, or they may originate along the equator and propagate poleward after reaching the coast of South America (Enfield and Allen 1980, Lyman and Johnson 2008). Marinovic et al. (2002) found evidence that Kelvin waves moved southern species of zooplankton into Monterey Bay during the 1997-1998 El Niño. Clarke and Dottori (2008) also found that aggregate zooplankton biomass in the southern California Current was correlated with sea level at San Diego at a two-month lag. They attributed the correlation to enhanced primary production behind the waves, when the sea-level was lowest and the thermocline shallowest. They proposed that this facilitated upwelling and primary production, enabling zooplankton populations to grow.

The lagged correlation of zooplankton with sea level noted by Clarke and Dottori (2008) was at a scale of weeks to months. In contrast, the correlations observed here occurred at a scale of days to weeks, with peak correlation at 1-day lags. The near-immediate response of micronekton to sea level change, the consistency of

this response through the water column, and the days-to-weeks-scale coherence all suggest passive aggregation by fluid motion as the link between sea level and micronekton abundance. This aligns with the analysis in Chapter 2, which showed that the power spectrum of the backscatter time series was similar to that expected for the velocity of a turbulent fluid. The mechanism behind this fluid motion and aggregation is not clear. A large portion (63%) of variability in de-seasonalized sea level can be accounted for by the inverted barometer and wind stress effects. The most visible example from our time series occurred from 21-29 January 2010, when strong winds from the southeast and low atmospheric pressure (986.6 mbar) coincided with the highest sea level of the 18-month series. Total acoustic backscatter also reached its maximum during this time, after an abrupt thickening of the deep scattering layer (approximately 400 m deep) over the course of several hours on 21 January.

This event highlights the unclear link between sea level and pelagic animal biomass. Onshore Ekman transport could collect zooplankton and micronekton in the surface layers against the coast, but would not extend to the mesopelagic zone below 300m, where sea level and micronekton were also correlated. An internal Kelvin wave could extend this deep, but is unlikely to be generated by local wind forcing over a few days. Downwelling resulting from onshore Ekman transport could perhaps carry animals from the surface to deeper water, but Ekman upwelling/downwelling velocities in the California Current are on the order of 10 m d^{-1} (Huyer 1983, Münchow 2000), which would not explain the sudden thickening of a biological layer centered at -400 m. Offshore, zooplankton can be aggregated at depth by mesoscale eddies and jets (Huntley et al. 2000, Godø et al. 2012). If such a feature were to impinge on the shelf, it could potentially bring its collection of zooplankton and micronekton with it. Alongshore advection of a pre-existing aggregation of animals is another possibility. Flagg et al. (1994), in a long-term acoustic Doppler current profiler deployment in the Mid-Atlantic Bight, saw similar abrupt (day-scale) increases in backscatter associated with reversals in alongshore currents.

3.4.2 Response of micronekton to upwelling

The response of micronekton to upwelling events was less pronounced than the response to sea level, but still measurable. Upwelling causes several changes in the pelagic habitat. One is a shoaling of the oxycline near the coast, a plausible explanation for observed changes in micronekton depth distribution following upwelling events. An oxygen minimum zone (OMZ) is found between approximately -500 and -1000 m in Monterey Bay, and is associated with a decrease in animal density and changes in species assemblages (Lynn et al. 1982, Robison et al. 2010). The OMZ in eastern boundary currents rises during upwelling, changing the distribution of micronekton and fish (Escribano et al. 2000, Chan et al. 2008). The upper edge of the OMZ can be acoustically located using backscatter from these animals (Bertrand et al. 2010). At time lags less than one month following low SST, backscatter decreased in the mesopelagic zone and increased in the surface and epipelagic zones, while decreasing slightly overall. This is consistent with upward animal movement, to avoid the shoaling of the OMZ, and transport offshore with the surface layer.

The negative correlation between backscatter and fluorescence at lags less than 20 days is related to correlations of backscatter with sea level and temperature, since the upwelling events that precede phytoplankton blooms are also associated with lowered sea level and temperature. Decreased micronekton abundances following phytoplankton blooms are interpreted as a direct consequence of these physical processes, rather than an indirect response through increased phytoplankton production.

At longer time lags, there appeared to be a true depth-dependent response of micronekton in the three depth zones to increased productivity at the surface. Backscatter in the surface, migrating, and non-migrating depth zones was maximally correlated with fluorescence at lags of 38, 48, and 64 days. The 38-day lag in the surface layer matched the 38.8-day generation time predicted for copepods at 10° C (Huntley and Lopez 1992). If we assume that the fluorescence signal is at the center of each depth zone at its maximum correlation, then it took 10 days to travel 175 m from the surface zone to the center of the epipelagic zone, and 16 days to travel 412 m from the migrating to the non-migrating zone, corresponding to speeds of 17.5 and 25.8 m d^{-1}. These rates are faster than those of sinking phytoplankton

(up to 1.69 m d^{-1}, Bienfang 1980), and slower than the fecal pellets of krill (126-862 m d^{-1}, Fowler and Small 1972), midwater fish (1028 m d^{-1}, Robison and Bailey 1981), or larvacean houses (800 m d^{-1}, Robison 2005), but agree well with sinking rates of marine snow measured in Monterey Bay, which ranged from 16.29 to 25.46 m d^{-1}, depending on the size of the particles (Pilskaln et al. 1998). The timing of these correlations is consistent with a near-surface pulse of secondary production in zooplankton following upwelling events, which then propagates down the water column in the form of marine aggregates. The increase in strength of correlation observed deeper in the water column is more difficult to explain, but may be due to greater short-scale "noise" near the surface than at depth.

3.4.3 Backscatter species and biology

The largest constraint on our interpretation of observed relationships is the lack of information on species composition and relative abundance of backscattering organisms. Inferring the composition of mixed-species assemblages from acoustic data is not possible with a single acoustic frequency and no direct sampling. Based on the acoustic frequency (38 kHz), backscattering properties of common zooplankton and fish (Stanton et al. 1996, Horne and Clay 1998), and literature on the California Current (Barham 1956, Kalish et al. 1986), we attribute most backscatter to "micronekton" (Brodeur and Yamamura 2005). This broad category contains a variety of myctophid fishes, squid, crustaceans, and some gelatinous animals. Micronekton in the California Current are dominated by a relatively small number of species, including krill (*Euphausia pacifica* and *Thysanoessa spinifera*), *Sergestes similis*, a panaeid shrimp, and myctophid fishes (*Diaphus theta*, *Stenobrachius leucopsarus*, and *Tarletonbeania crenularis*) (Phillips et al. 2009). All of these animals have been associated with sound-scattering layers (Barham 1956, Kalish et al. 1986). Larger nekton are present as well, including macrourids (Yeh and Drazen 2011), Pacific hake (*Merluccius productus*) and, in recent years, Humboldt squid (*Dosidicus gigas*, see Field et al. 2007), though the relative contribution of these species to overall biomass and backscatter is likely to be small compared with the smaller but much more abundant micronektonic species. Dense surface aggregations were sometimes present, especially from February through April, probably representing surface-schooling krill (*Euphausia pacifica* or *Thysanoessa spinifera*, Smith and Adams 1988),

sardine (*Sardinops sagax*), or anchovy (*Engraulis mordax*, Cailliet et al. 1979). These aggregations make substantial contributions to water column biomass on a scale of minutes as they pass through the acoustic beam, but do not affect trends at scales of days or longer. When the acoustic threshold on 30 randomly-selected echograms was raised from -90 dB (the level used in our analysis) to -58.5 dB (the level used for fisheries surveys of hake, Wilson and Guttormsen 1997), an average of 77% of the backscatter was eliminated. This suggests that the majority of backscatter is attributable to smaller animals.

Deconvolving changes in backscatter into kinematic movement, population growth, somatic growth, and shifts in species composition is difficult. Small and medium-sized zooplankton populations typically trail phytoplankton abundance by approximately 30 days in temperate waters (Huntley and Lopez 1992), though these species are unlikely to be detected by DEIMOS unless densely aggregated. *Euphausia pacifica*, the dominant krill species in the California Current and Monterey Bay, appear to spawn mostly in the spring, with the peak abundance of adults in fall (Marinovic et al. 2002). *Sergestes similis* reproduces year-round with a springtime peak, and is most abundant over the continental slope during winter (Pearcy and Forss 1969, Omori and Gluck 1979). Myctophids in southern California were most abundant in winter (Paxton 1967). Other potentially important scattering organisms include the market squid (*Loligo opalescens*), most abundant in Monterey Bay from April through July (Fields 1965), and *Nanomia bijuga*, a physonect siphonophore, whose abundance peaks in late summer near 500 m depth (Barham 1963, Robison et al. 1998). The seasonal cycle of backscatter, peaking in fall and winter, appears consistent with the life-histories of the dominant micronekton taxa.

3.4.4 *Predictive ability of model*

None of the environmental covariates included in our analyses was a particularly powerful predictor of micronekton abundance. This could be in part because of spatial variability in the environmental variables and the fact that M1 and DEIMOS were separated by 15 km. Though conditions at the two locations were correlated, the relationships were noisy, and this spatial variability could have confounded our temporal measurements. Local hydrographic features may also have played a role. Both M1 and DEIMOS were located near the Davenport upwelling plume,

which trails south across the mouth of Monterey Bay from Point Año Nuevo. The Davenport plume is a persistent feature that is typically cool, nutrient-rich, and phytoplankton-poor (Pennington and Chavez 2000). These characteristics could complicate the classical wind-upwelling-phytoplankton chain of events, perhaps biasing SST and fluorescence low.

A more general explanation for the weak predictive power of the environmental covariates is the difference between the temporal scale of phytoplankton and micronekton population dynamics. Phytoplankton blooms appear and disappear on the scale of days. Populations of small zooplankton grow on a scale of weeks, while those of large zooplankton and micronekton (i.e., those acoustically detected by DEIMOS) take several months. There is some evidence some micronekton cue reproduction on upwelling events (Dorman et al. 2005), but their ontogenic growth integrates over multiple productivity pulses, presumably damping the signal of individual upwelling events. This interpretation is consistent with the regression model, whose autoregressive terms accounted for more variability than the external covariates. The "long memory" observed in the regression model has implications for mobile predators foraging on micronekton. We would predict foraging behavior to rely more on availability of prey than on environmental cues. The tendency of the mid-trophic levels to integrate variability in primary production also explains an interesting scale-dependence in the response of krill populations to sea surface temperature. Krill abundance in the California Current was found to be negatively correlated with sea surface temperature on inter-annual time scales (Jahncke et al. 2008), though we found it to be positively correlated with SST on seasonal and shorter time scales.

3.4.5 Conclusion

Our results show a complex relationship between the variability of animal biomass and the variability of their environment. Biomass density at any location varies as animals swim, drift with currents, grow somatically, interact with other species, and increase or decline as a population. The relative importance of these processes depends on the spatial and temporal scales over which they occur, as well as measurement resolution (Horne and Schneider 1994). At sub-seasonal time scales in Monterey Bay, the strongest coupling appeared to be passive aggregation of mi-

cronekton by fluid motion, though the exact nature of this fluid motion was not obvious. During upwelling events, the overall abundance of animals decreased and became concentrated near the surface, consistent with vertical swimming to avoid the shoaling OMZ and movement offshore with the Ekman layer. Approximately five weeks after upwelling events, backscatter increased in the surface layer, suggesting reproduction of small or medium-sized zooplankton. The upwelling signal then appeared to propagate down the water column at rates similar to those measured for sinking marine aggregates. Variability in animal density influenced by physical processes is distributed across a wide range of temporal scales. High-resolution, temporally-indexed observations of animal density such as those from DEIMOS allow animal variability to be measured and compared to other biological and physical processes at temporal scales not possible with other methods. Augmenting stationary acoustic measurements with direct sampling of the scattering organisms would allow the speculative explanations given here to be tested more rigorously. Ultimately, data and analysis such as those presented here could be used to augment fisheries and ecosystem assessments by adding an independent temporal dimension.

4.

SUMMARY AND CONCLUSIONS

4.1 Summary

Stationary acoustic instruments are capable of monitoring biological activity over a wide range of temporal scales. One sonar installation can record processes ranging from brief predator-prey interactions, to seasonal changes relevant to ecosystem management, to multi-year changes relevant to decadal cycles and global change.

The Deep Echo Integrating Marine Observatory System (DEIMOS), a scientific echosounder package, was deployed 875 m below the surface of Monterey Bay, California, at the MARS cabled observatory node from February 2009 to August 2010. DEIMOS recorded a high-resolution image of biomass distribution in the water column through time, forming a continuous record of the Bay's pelagic biology, from zooplankton to whales. To date, there have been relatively few ecological studies using stationary echosounders. Among this small number, the deployment of DEIMOS stands out for both its length (18 months) and oceanic location.

A dataset of this size and complexity presents significant challenges in its interpretation and quantification. To parsimoniously describe the distribution of animals in the water column, a suite of landscape metrics was developed and applied to the acoustic data through time. This suite of metrics included both landscape descriptors adapted to stationary acoustic data and a novel image-analysis based algorithm to detect and count backscattering layers in the water column. All metrics were tested for their sensitivity to input parameter values using a Monte Carlo-based approach and Latin hypercube sampling. Metrics were found to be reasonably insensitive to parameter values within the parameter ranges used.

The metric suite was then used to describe patterns of temporal variability in the vertical distribution of pelagic fauna at the DEIMOS site. The metric series revealed a strong seasonal cycle, with peak densities in the fall and winter, when a large, deep, non-migrating layer was present near 500 m depth. Density was lowest during the spring, when the deep layer disappeared and most backscatter was located near the surface. After these seasonal trends were removed, the metric series still displayed strong autocorrelation. The Fourier spectra of all series showed variance increasing as a power of temporal scale. In most of the series, the exponent of the power law relation (as a function of frequency) was close to the theoretical value of -5/3 for the velocity spectrum of a turbulent fluid, suggesting that most of the scattering organisms behaved as passive drifters. The spectra of the index of aggregation and number of layers had shallower slopes, indicating that animals swam actively to maintain their aggregations.

The acoustic data were also compared with oceanographic data from MBARI's M1 data buoy, located 15 km east-northeast of DEIMOS, to investigate the response of pelagic fauna to oceanic variability. At the seasonal scale, backscatter was lowest in spring, when upwelling was most active and primary production was highest. Backscatter was also correlated with upwelling at shorter time scales. Cross-wavelet transforms showed intermittent periods of coherence between the oceanographic and acoustic variables at scales between approximately 8 and 32 days, corresponding to the scale of upwelling variability. Backscatter decreased and moved higher in the water column following upwelling events. This movement is attributed to some combination of advection offshore and avoidance of the shoaling oxygen minimum zone. Of the oceanographic variables considered, backscatter was correlated best with sea level, with a significant positive correlation at one- to two-day lags.

The response of pelagic fauna to oceanographic variability differed with depth. Backscatter in the upper 50 m decreased immediately following upwelling, then increased at lags of 30-70 days, with a peak at 38 days. This matches the predicted generation time of a copepod at 10° C (Huntley and Lopez 1992). Similar relationships existed in the epipelagic (50-300 m) and mesopelagic (300-875 m) depth zones, but with lags of 48 and 64 days respectively. These increasing lags with depth imply that near-surface productivity propagated down the water column at speeds between 17.5 and 25.8 m d^{-1}, consistent with sinking speeds of marine snow mea-

sured in Monterey Bay (Pilskaln 1996) (Pilskaln et al. 1998).

4.2 Significance

Ocean Observatories will play an increasing role in marine science, monitoring changes at resolutions and to an extent not possible with ship-based sampling. The methods and results presented here will help lay the foundation for the use of acoustic instrumentation in ocean observatories. The use of scientific echosounders for long-term observations at depth is relatively new. Though analysis of longer-term time series is well established in physical oceanography, high-resolution temporal analyses of biological profiles from echosounders are rare. If stationary echosounders are widely deployed as part of future ocean observing networks, first-order descriptors of patterns and variability are needed for what will be an immense data stream. The metric suite developed in this thesis provides one objective means to quantify biomass in the water column. These metrics could be used for automatic quality control and flagging potential regions of bad data. They could also be used as objective descriptors of ecosystems for long-term monitoring, potentially shedding light on ocean health in the context of ongoing climate and ecosystem changes.

Methods and techniques developed in this study will be used by other researchers, particularly in the U.S. National Science Foundation's Ocean Observatories Initiative. Stationary acoustic data may also find uses in fisheries and ecosystem management. Stock assessments are typically based on once- or twice-yearly surveys of abundance and spatial distribution, and implicitly assume that temporal variation at other scales can be ignored. Stationary acoustics could add an independent temporal dimension to fisheries surveys, and may increase the understanding of factors influencing prey availability to predators.

Many of the central questions in oceanography and marine ecology relate to the link between ocean dynamics and biological processes. These questions are relevant in the California Current, since the effects of physics—discrete, seasonal wind-driven upwelling—propagate through the entire food web, including commercially important fisheries and protected species such as pinnipeds and whales. The continuous acoustic data from DEIMOS allowed us to better understand this connection by monitoring mid-trophic levels where primary productivity, fueled by upwelled nutrients, is converted to biomass that is then available to higher trophic

level predators, including humans. In the future, long-term acoustic deployments in other locations would enable comparisons of pelagic ecosystem dynamics in different regions and oceanographic regimes.

The scale-dependent temporal variability of animal populations has been studied relatively little. Many different definitions of "temporal variability" have been used, and not always with quantitative justification (Gaston and McArdle 1994). Though the number of ecological articles mentioning scale has grown exponentially over the past four decades, articles including the phrase "spatial scale" have been several times more common than those citing "temporal scale" (Schneider 2009, p.23). Put another way, temporal scale's recognition lags about a decade behind that of spatial scale.

A stationary echosounder's high-scope temporal observations make it possible to quantify temporal variability across a wide range of scales. In addition to documenting temporal changes in biomass, layer formation, and vertical migrations, the high-resolution, long-term data record allowed description of these same phenomena in the frequency domain, providing otherwise unavailable insight into scales of biological variability in an upwelling-driven eastern boundary system. I believe that stationary acoustics are a very promising approach in marine ecology, and hope that future studies will be able to extend and deepen these insights in Monterey Bay and elsewhere.

A.

ECHOGRAMS

This appendix includes echograms of acoustic data from the full deployment of DEIMOS. These patterns are described verbally and statistically in the second and third chapters, but I believe there is tremendous value in seeing them visually, all together. The metrics developed in this thesis are effective as summary descriptors, but do not capture all the detail apparent in these echograms. Our eyes are remarkably skilled at detecting patterns and trends—infuriatingly so, when you are trying to teach a dumb computer how to perform a simple task like counting the number of scattering layers. I hope these echograms, aside from being pretty, will give the reader a clearer sense of the submarine landscape in outer Monterey Bay, and perhaps provoke new questions.

Before plotting, external noise was estimated and subtracted using an automated, adaptive algorithm (De Robertis and Higginbottom 2007). Bad data regions were defined manually, and appear as vertical white stripes of missing data. Long gaps of missing data are noted where they occur. Vertical lines are drawn one day apart at midnight, Pacific Standard Time. Horizontal lines are spaced at 100 m intervals from the surface to the bottom. The colors represent the echo intensity, expressed as the mean volume backscattering strength S_v (MacLennan et al. 2002).

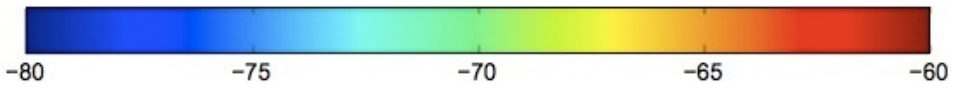

S_v (dB re. m^2 m^{-2})

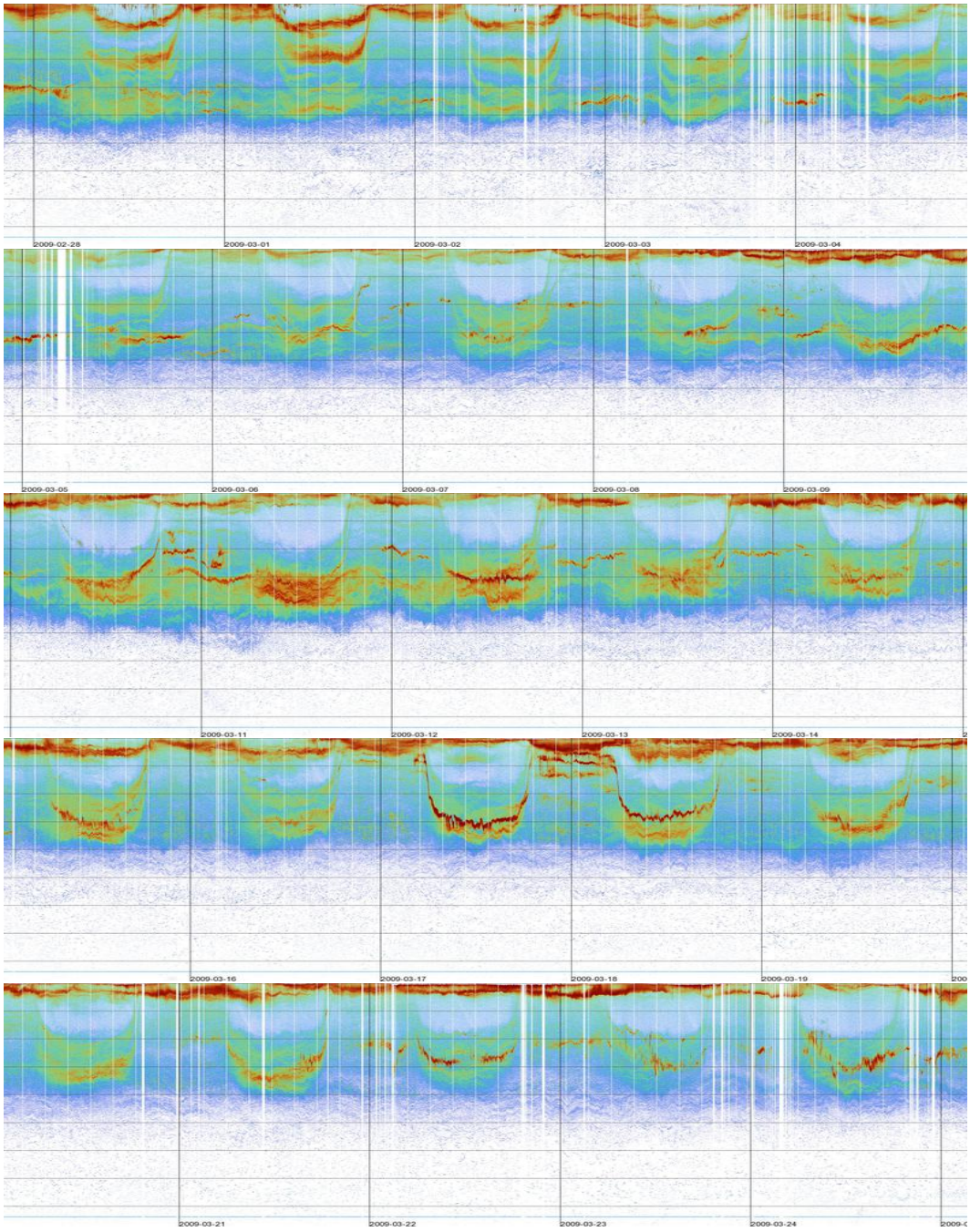
2009-02-28
2009-03-01
2009-03-02
2009-03-03
2009-03-04
2009-03-05
2009-03-06
2009-03-07
2009-03-08
2009-03-09
2009-03-11
2009-03-12
2009-03-13
2009-03-14
2009-03-16
2009-03-17
2009-03-18
2009-03-19
2009-03-21
2009-03-22
2009-03-23
2009-03-24

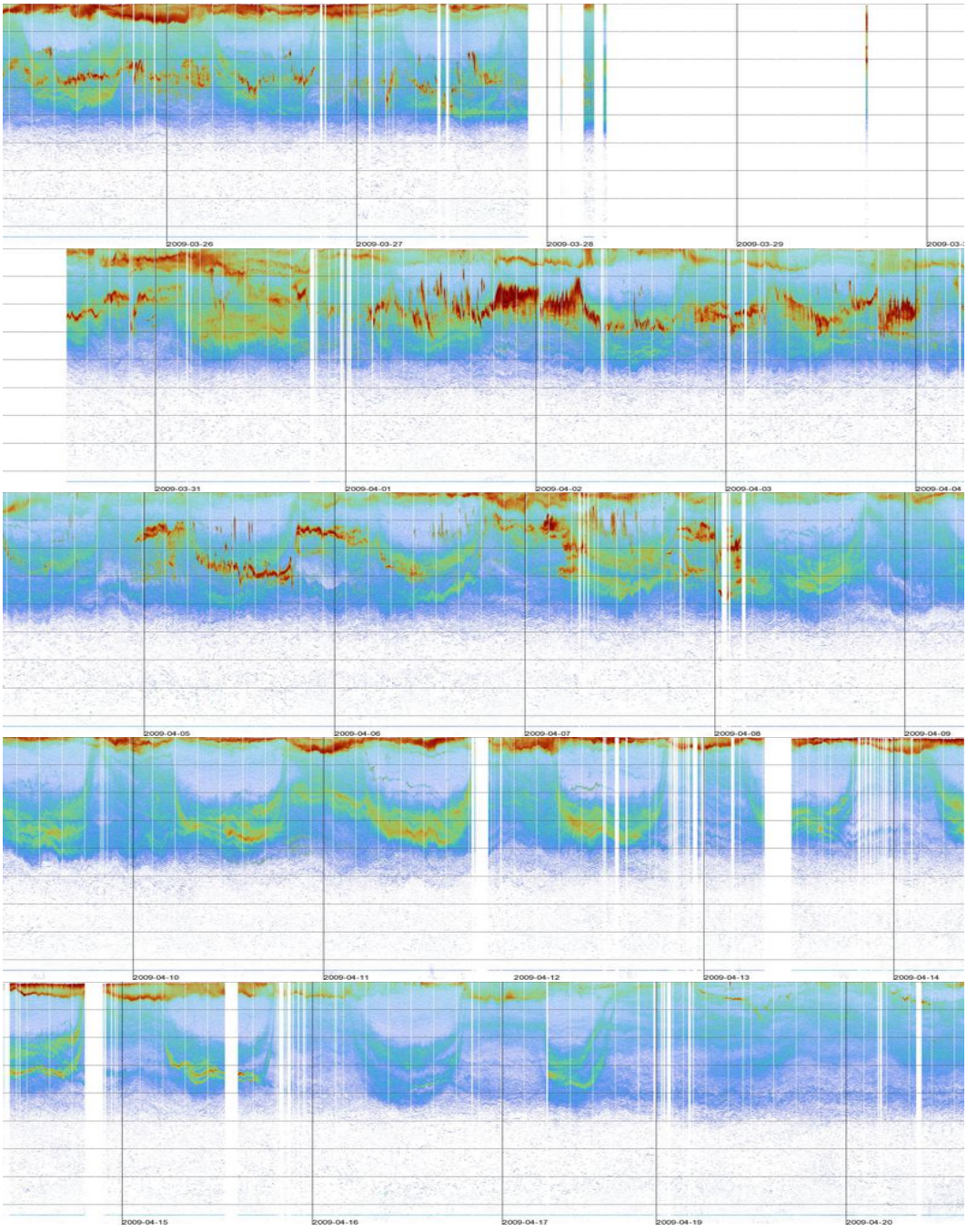
2009-03-26
2009-03-27
2009-03-28
2009-03-29
2009-03-31
2009-04-01
2009-04-02
2009-04-03
2009-04-04
2009-04-05
2009-04-06
2009-04-07
2009-04-08
2009-04-09
2009-04-10
2009-04-11
2009-04-12
2009-04-13
2009-04-14
2009-04-15
2009-04-16
2009-04-17
2009-04-19
2009-04-20

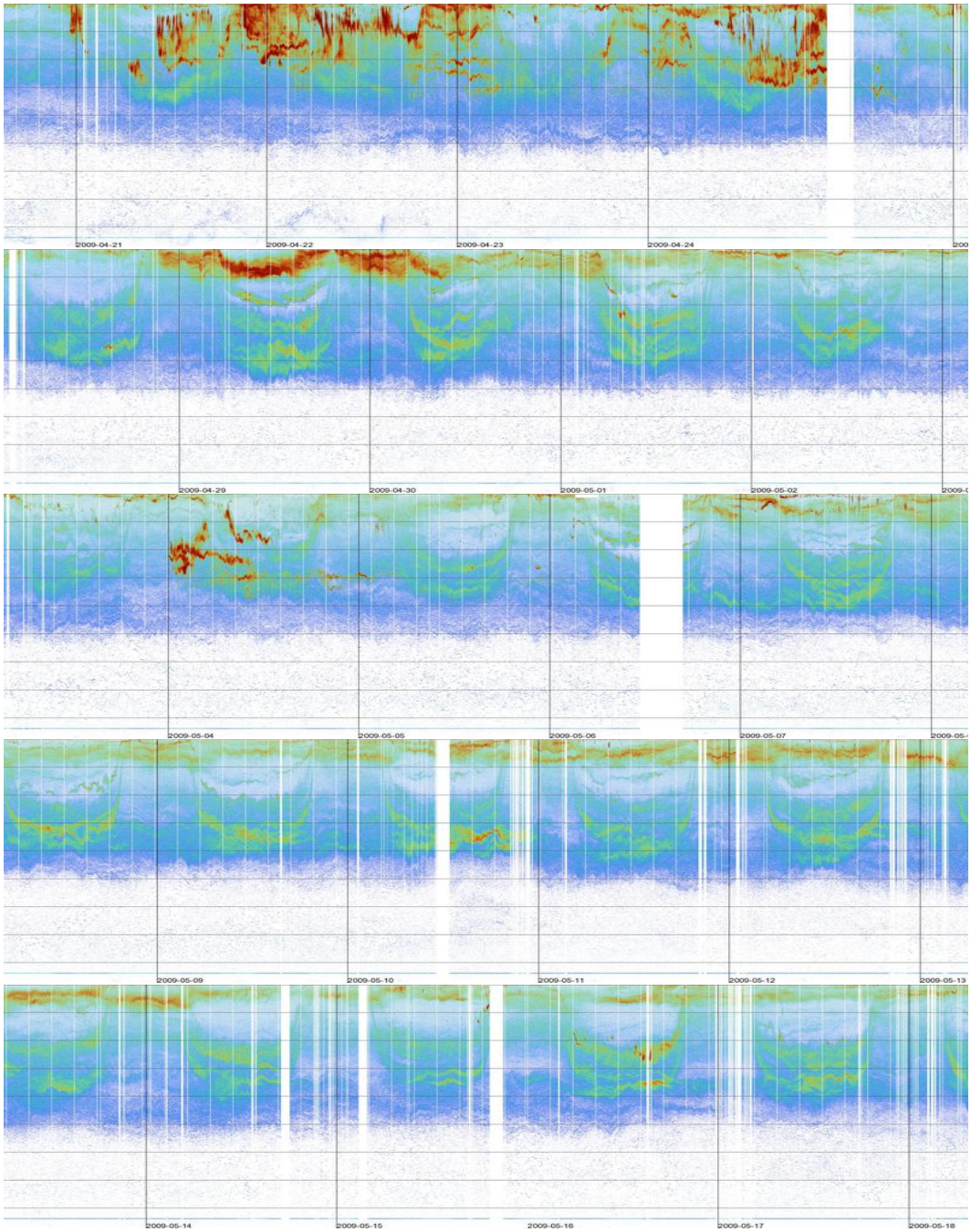
2009-04-21
2009-04-22
2009-04-23
2009-04-24
2009-04-29
2009-04-30
2009-05-01
2009-05-02
2009-05-04
2009-05-05
2009-05-06
2009-05-07
2009-05-09
2009-05-10
2009-05-11
2009-05-12
2009-05-13
2009-05-14
2009-05-15
2009-05-16
2009-05-17
2009-05-18

On 18 May 2009, another instrument on MARS's 48 V power line was recovered. Without a full load, electrical noise was apparently introduced into the power supply, saturating DEIMOS's receiver and rendering the data unusable. DEIMOS was shut down until 14 August, when another instrument was deployed, again putting a full load on the 48 V line and removing the noise.

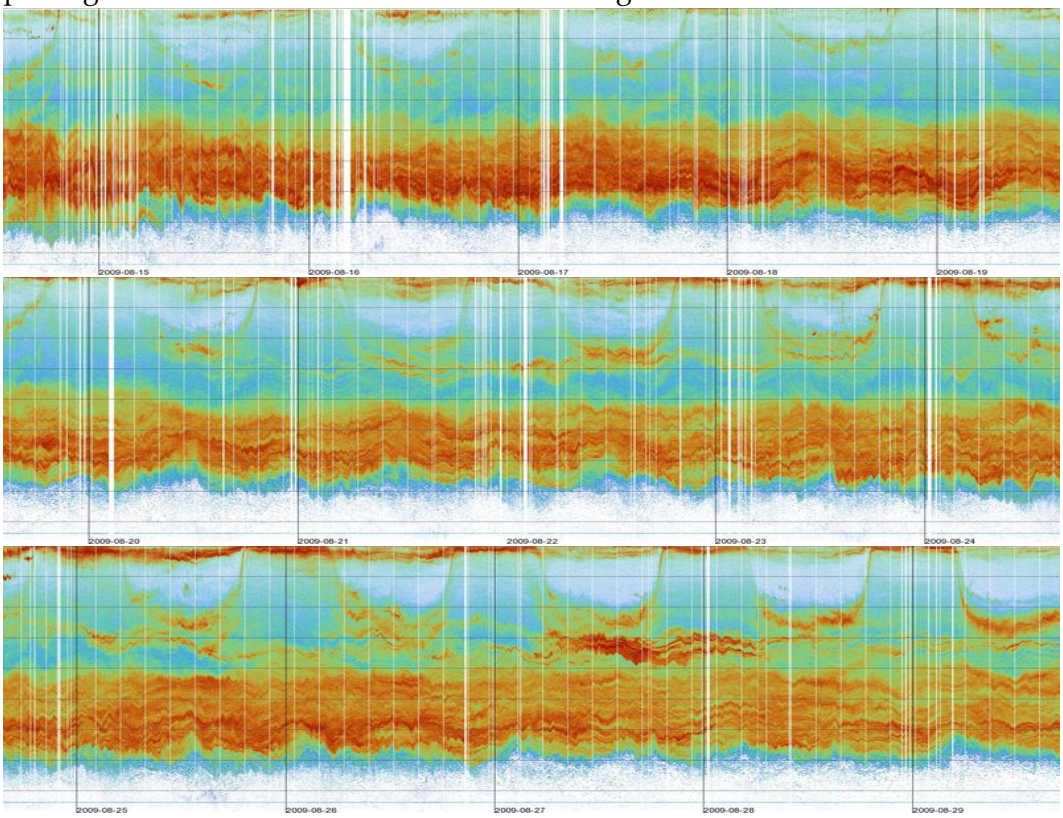

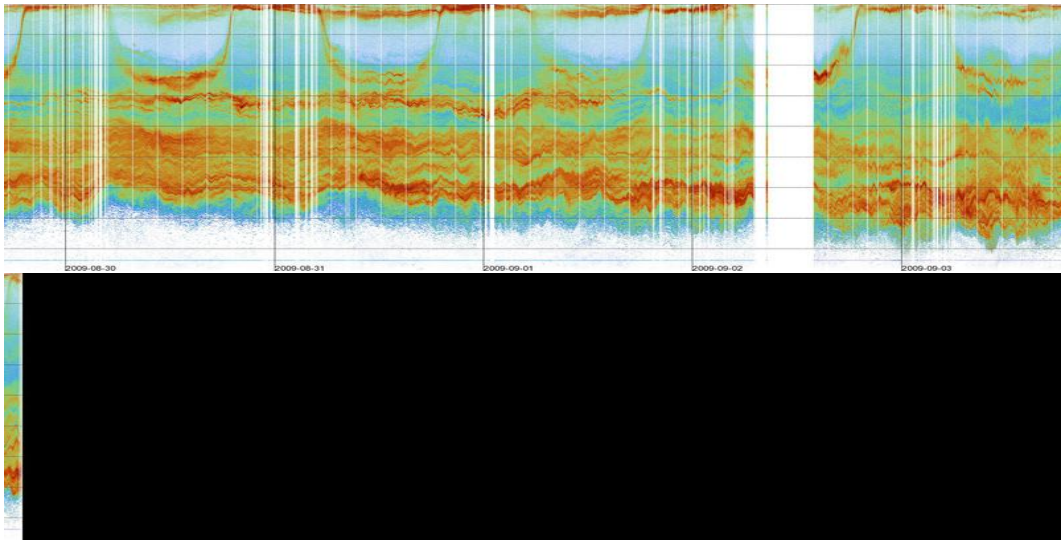

An unnoticed software crash on 3 September, 2009 halted data collection until 14 September when the system was restarted.

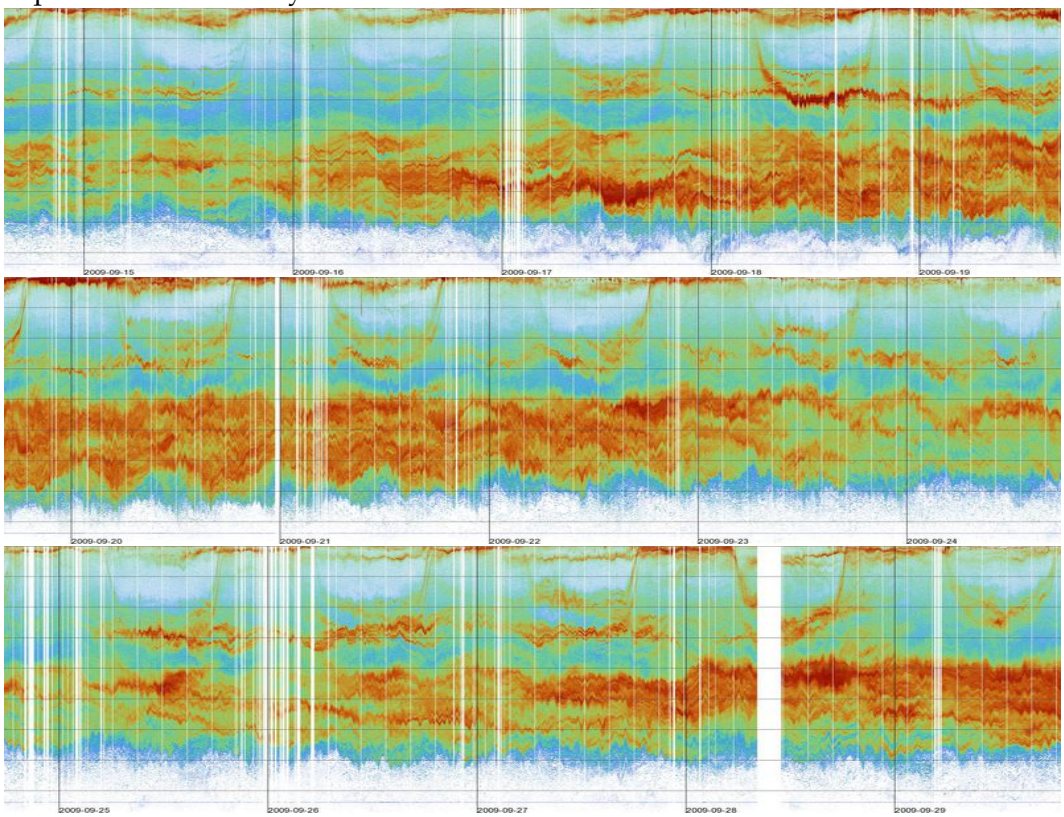

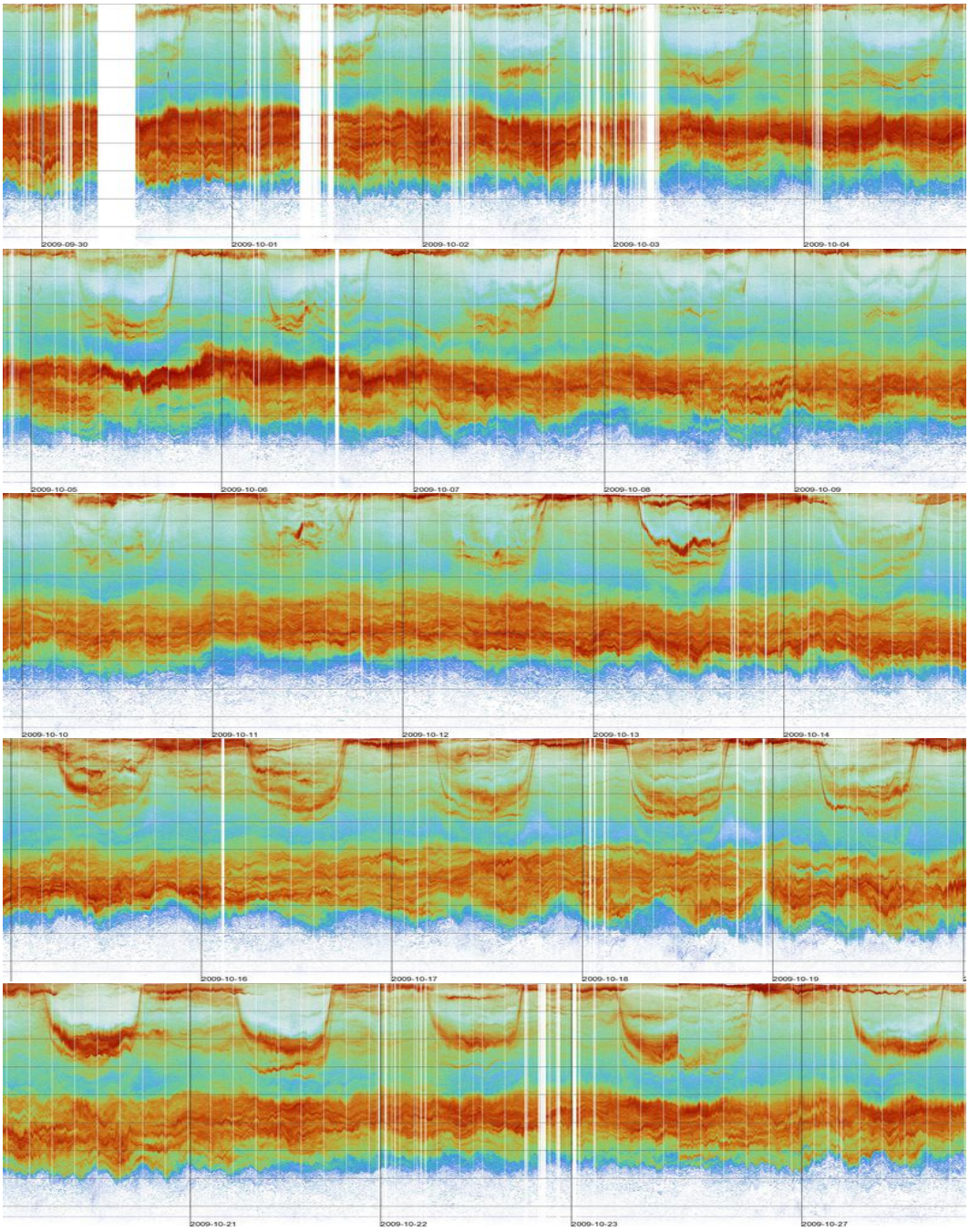
2009-09-30
2009-10-01
2009-10-02
2009-10-03
2009-10-04
2009-10-05
2009-10-06
2009-10-07
2009-10-08
2009-10-09
2009-10-10
2009-10-11
2009-10-12
2009-10-13
2009-10-14
2009-10-16
2009-10-17
2009-10-18
2009-10-19
2009-10-21
2009-10-22
2009-10-23
2009-10-27

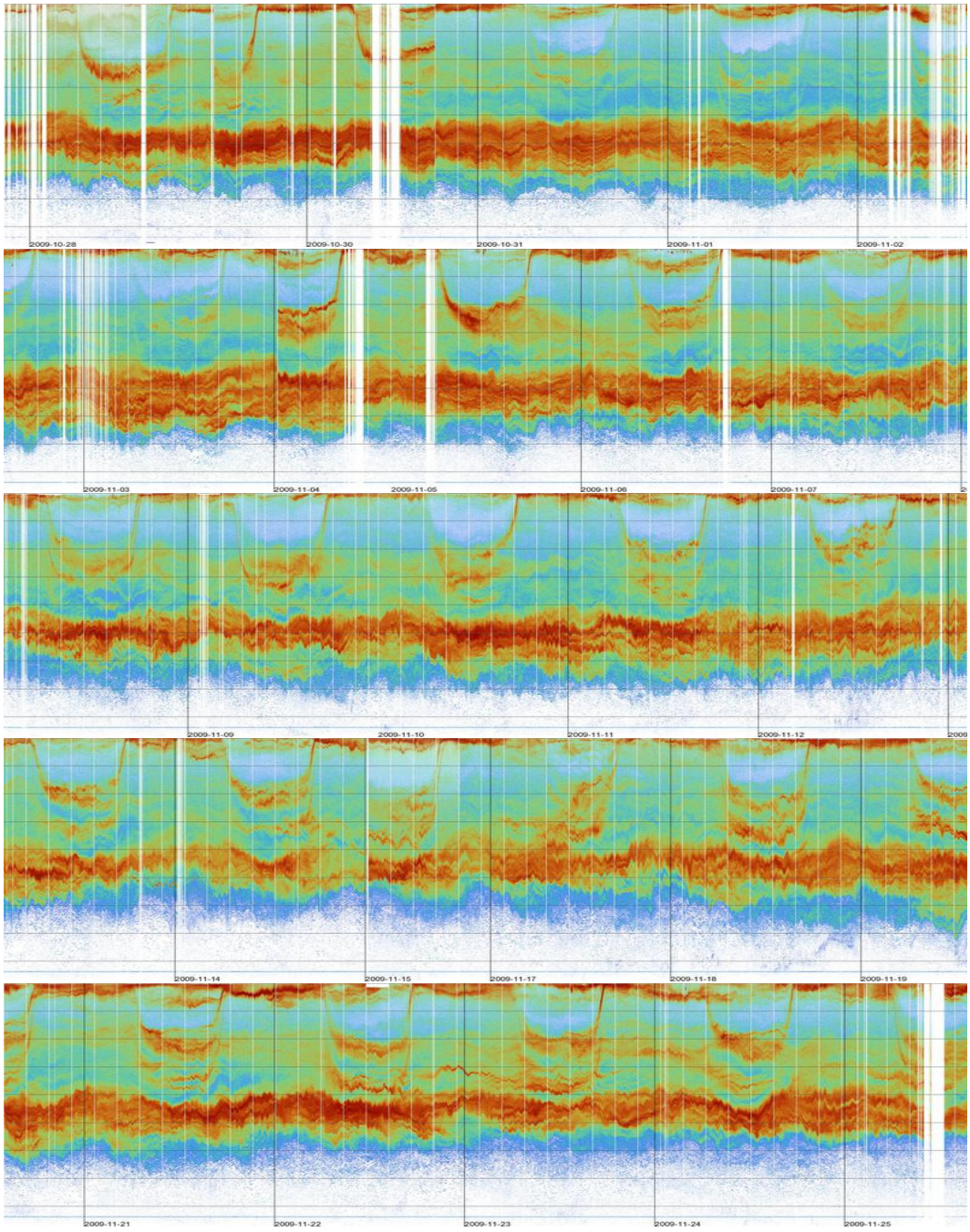
2009-10-28
2009-10-30
2009-10-31
2009-11-01
2009-11-02
2009-11-03
2009-11-04
2009-11-05
2009-11-06
2009-11-07
2009-11-09
2009-11-10
2009-11-11
2009-11-12
2009-11-14
2009-11-15
2009-11-17
2009-11-18
2009-11-19
2009-11-21
2009-11-22
2009-11-23
2009-11-24
2009-11-25

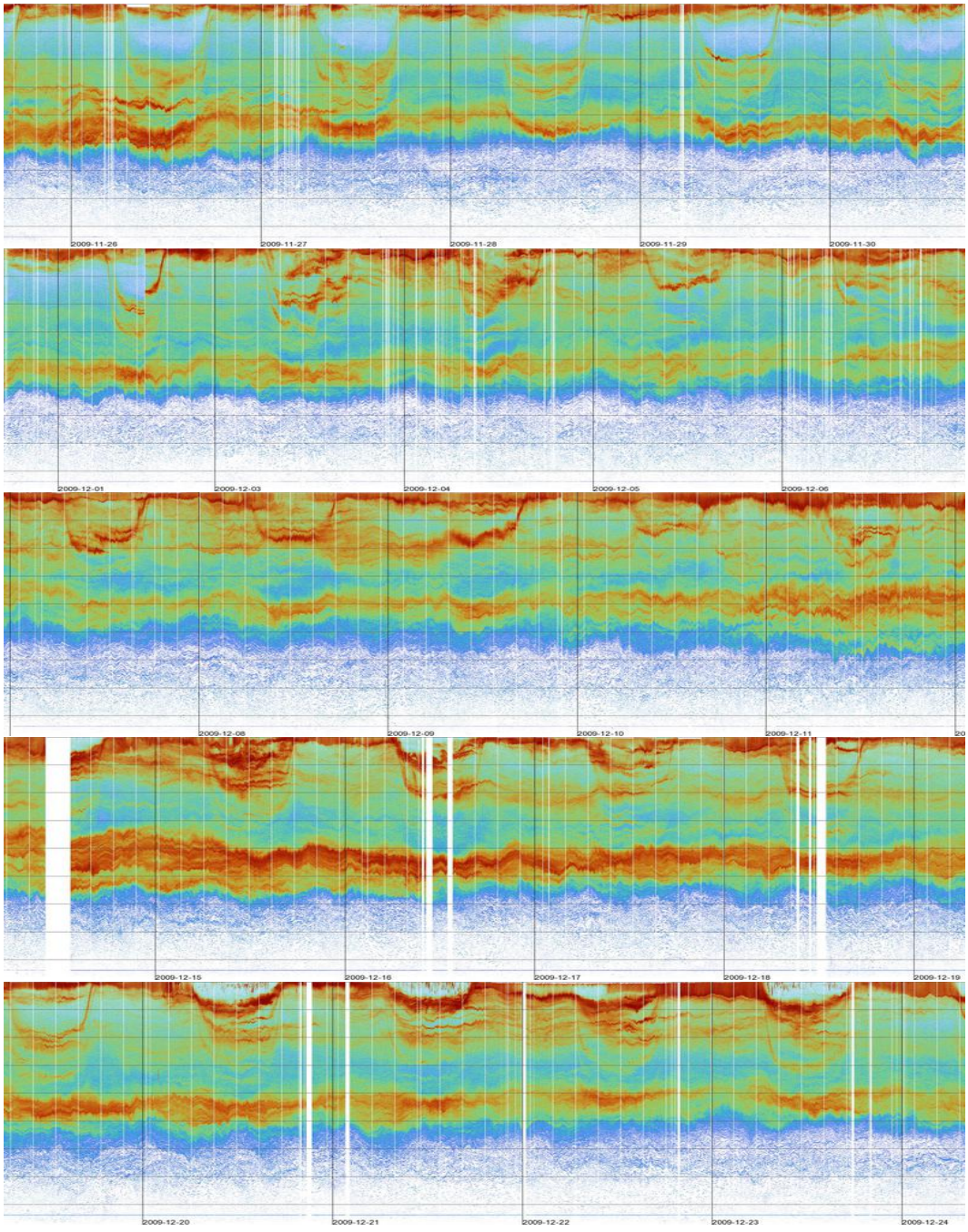
2009-11-26
2009-11-27
2009-11-28
2009-11-29
2009-11-30
2009-12-01
2009-12-03
2009-12-04
2009-12-05
2009-12-06
2009-12-08
2009-12-09
2009-12-10
2009-12-11
2009-12-15
2009-12-16
2009-12-17
2009-12-18
2009-12-19
2009-12-20
2009-12-21
2009-12-22
2009-12-23
2009-12-24

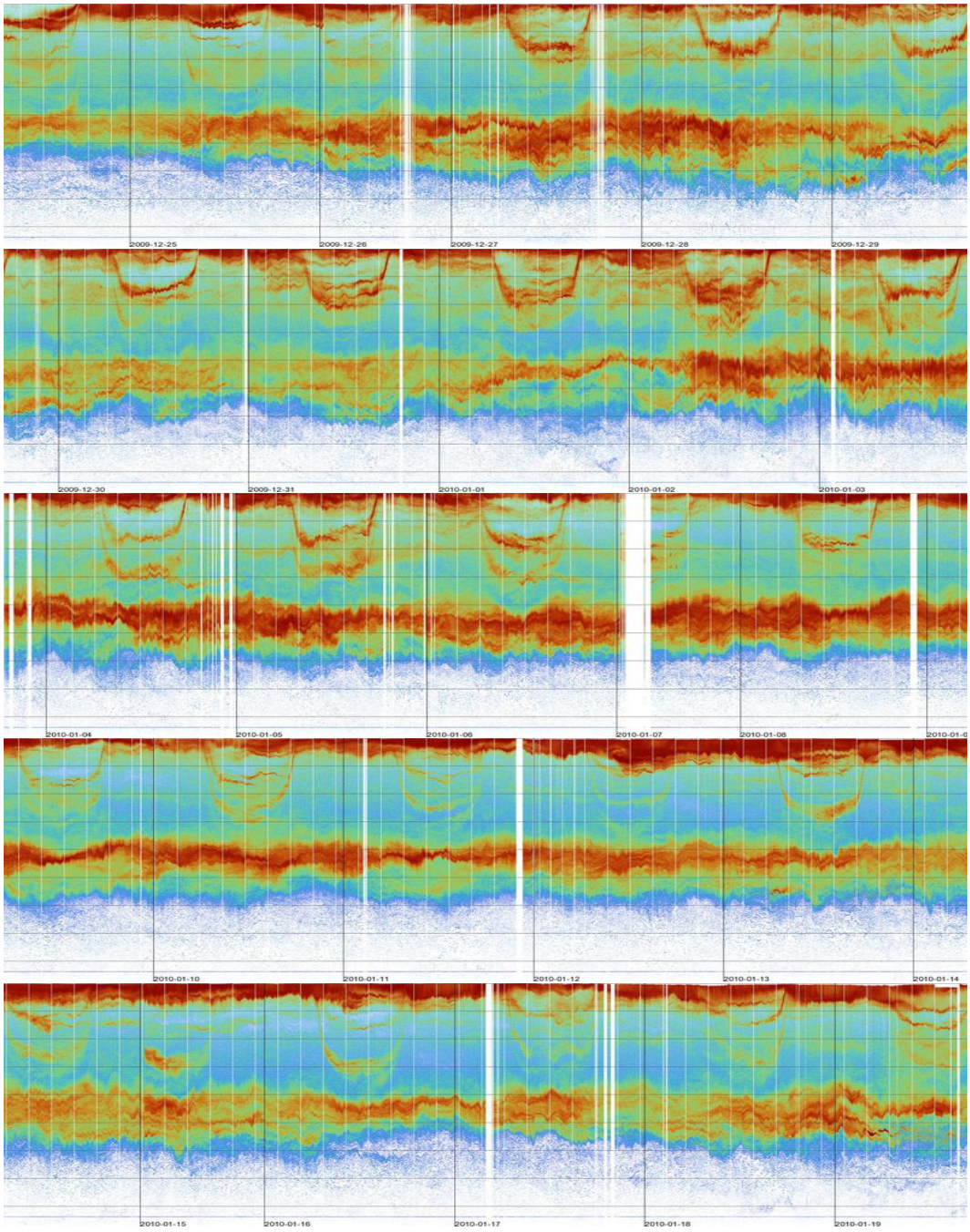
2009-12-25
2009-12-26
2009-12-27
2009-12-28
2009-12-29
2009-12-30
2009-12-31
2010-01-01
2010-01-02
2010-01-03
2010-01-04
2010-01-05
2010-01-06
2010-01-07
2010-01-08
2010-01-10
2010-01-11
2010-01-12
2010-01-13
2010-01-14
2010-01-15
2010-01-16
2010-01-17
2010-01-18
2010-01-19

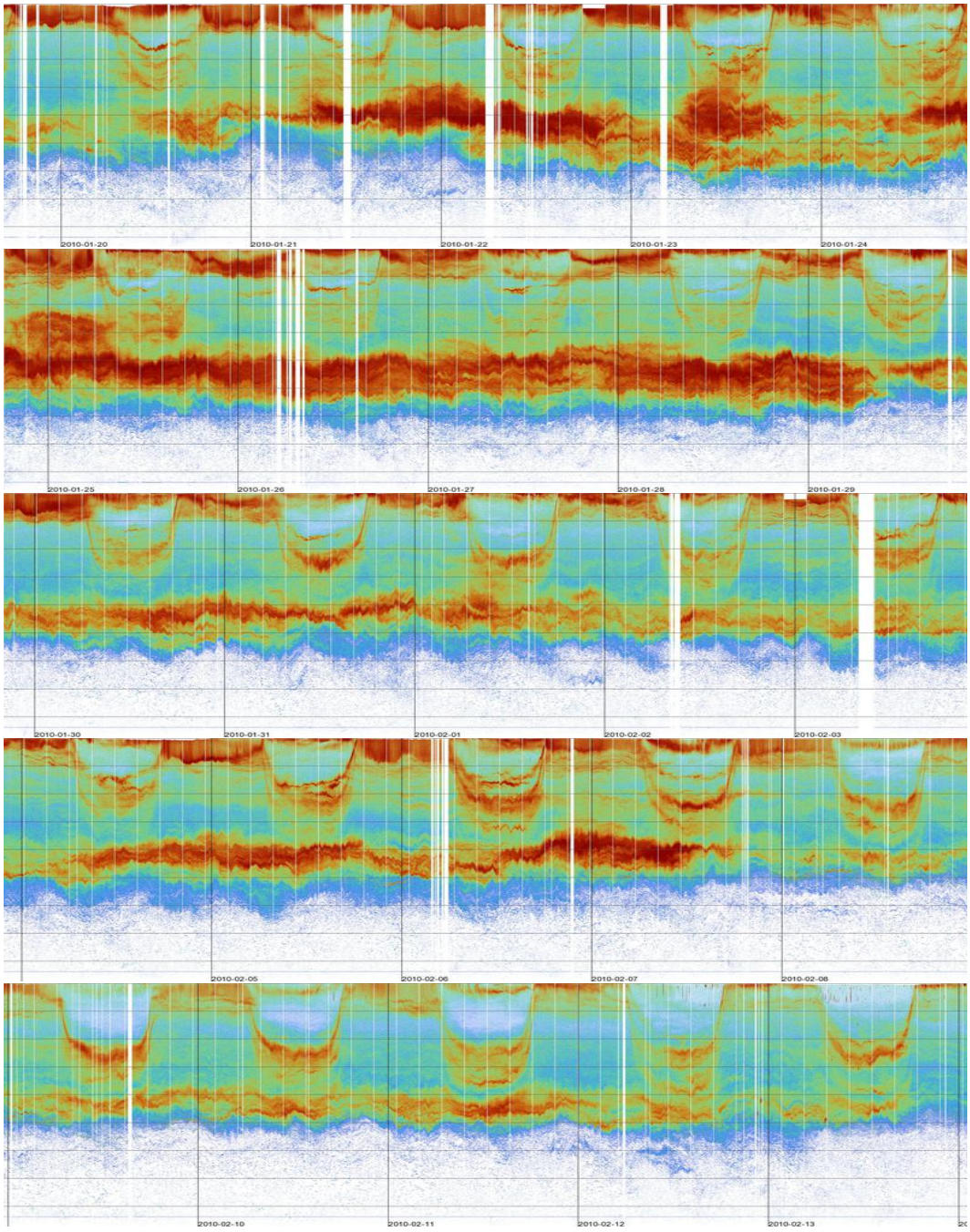
2010-01-20
2010-01-21
2010-01-22
2010-01-23
2010-01-24
2010-01-25
2010-01-26
2010-01-27
2010-01-28
2010-01-29
2010-01-30
2010-01-31
2010-02-01
2010-02-02
2010-02-03
2010-02-05
2010-02-06
2010-02-07
2010-02-08
2010-02-10
2010-02-11
2010-02-12
2010-02-13

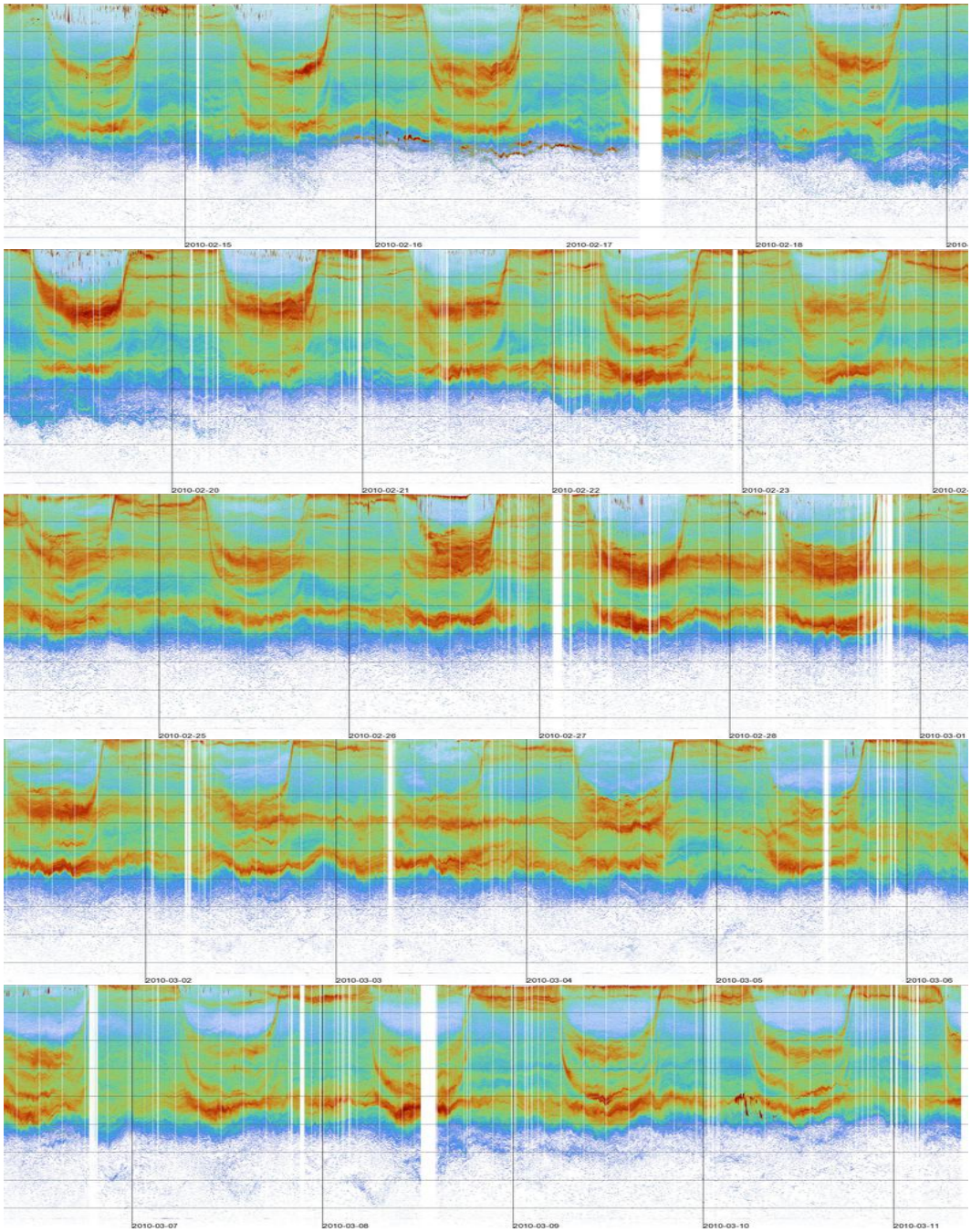
2010-02-15
2010-02-16
2010-02-17
2010-02-18
2010-02-20
2010-02-21
2010-02-22
2010-02-23
2010-02-25
2010-02-26
2010-02-27
2010-02-28
2010-03-01
2010-03-02
2010-03-03
2010-03-04
2010-03-05
2010-03-06
2010-03-07
2010-03-08
2010-03-09
2010-03-10
2010-03-11

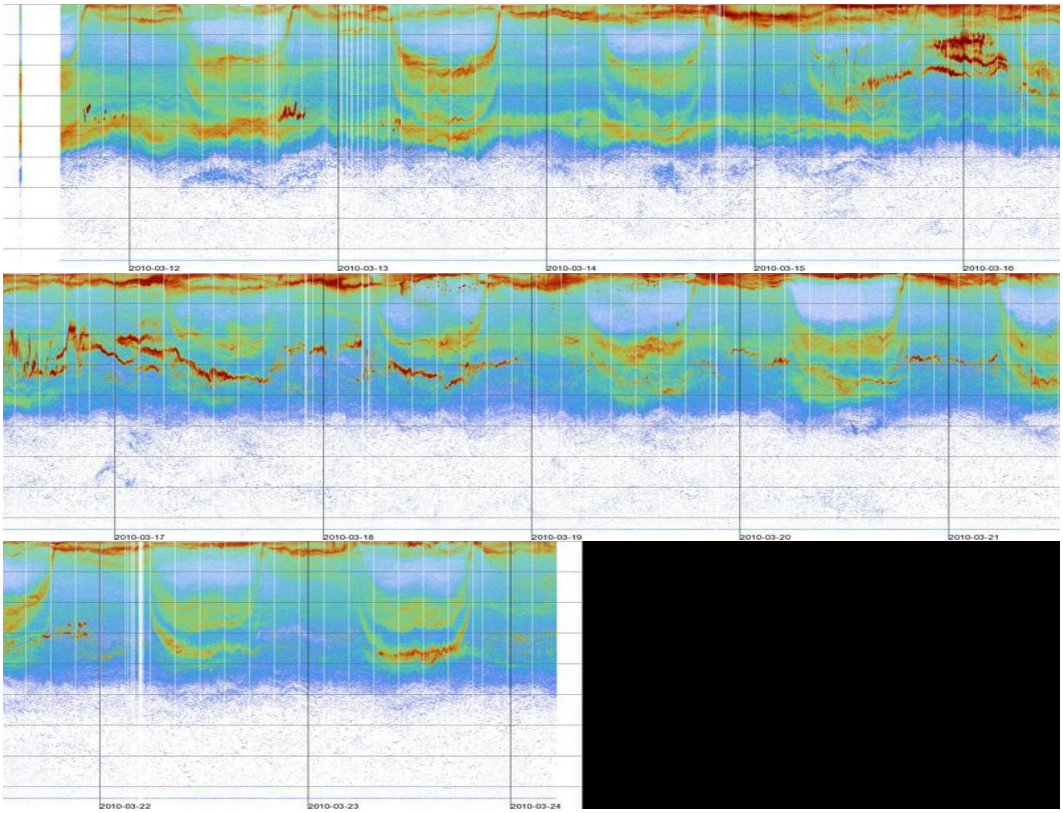

Recovery of another instrument from MARS on 24 March 2010 again caused elevated noise in DEIMOS's power supply until another instrument was redeployed on 3 April.

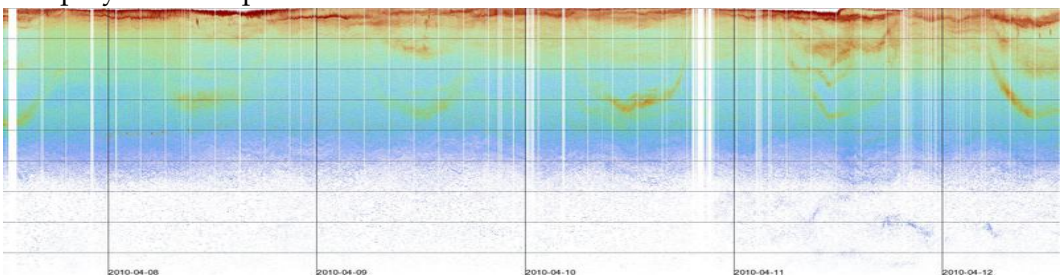

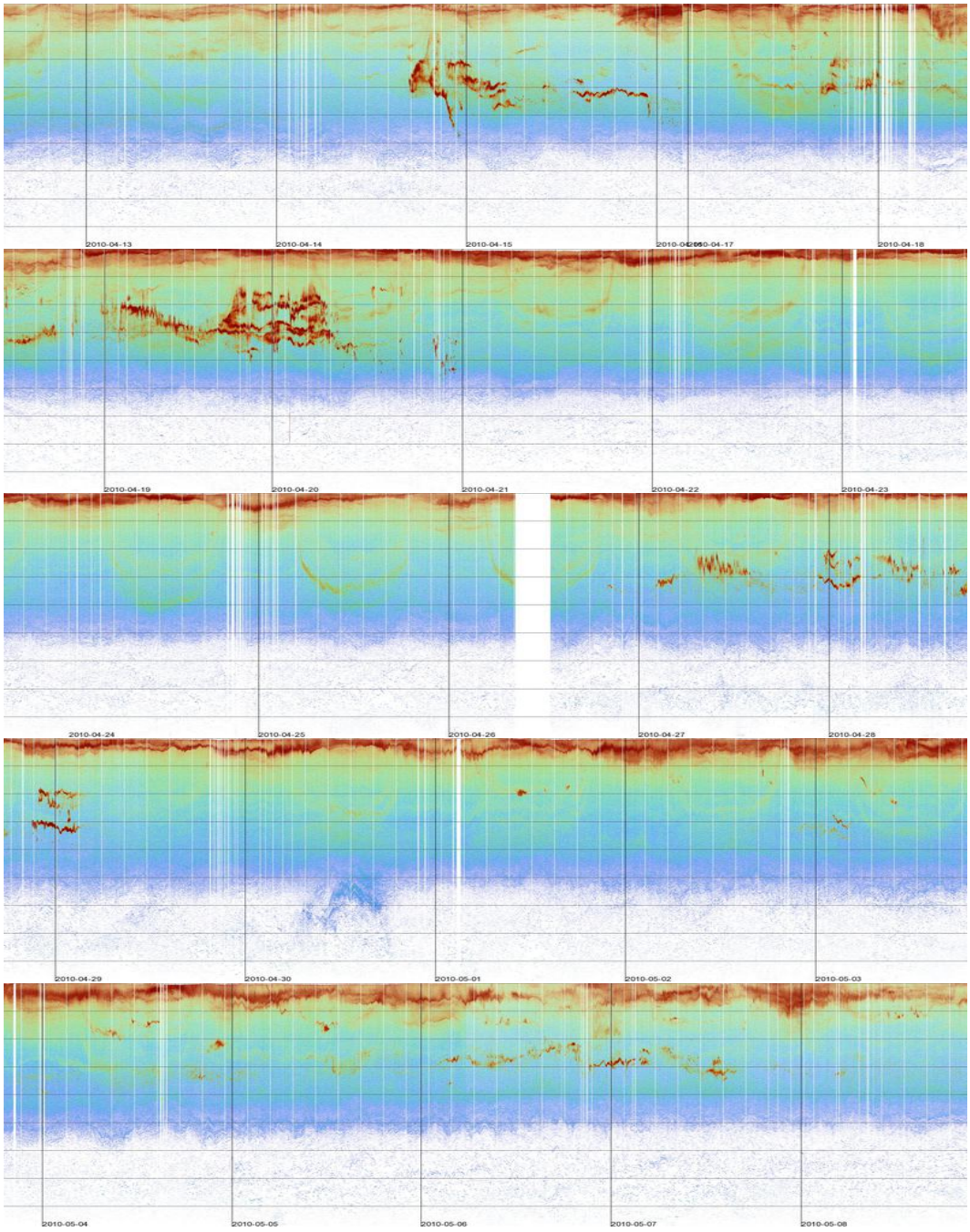
2010-04-13
2010-04-14
2010-04-15
2010-04-17
2010-04-18
2010-04-19
2010-04-20
2010-04-21
2010-04-22
2010-04-23
2010-04-24
2010-04-25
2010-04-26
2010-04-27
2010-04-28
2010-04-29
2010-04-30
2010-05-01
2010-05-02
2010-05-03
2010-05-04
2010-05-05
2010-05-06
2010-05-07
2010-05-08

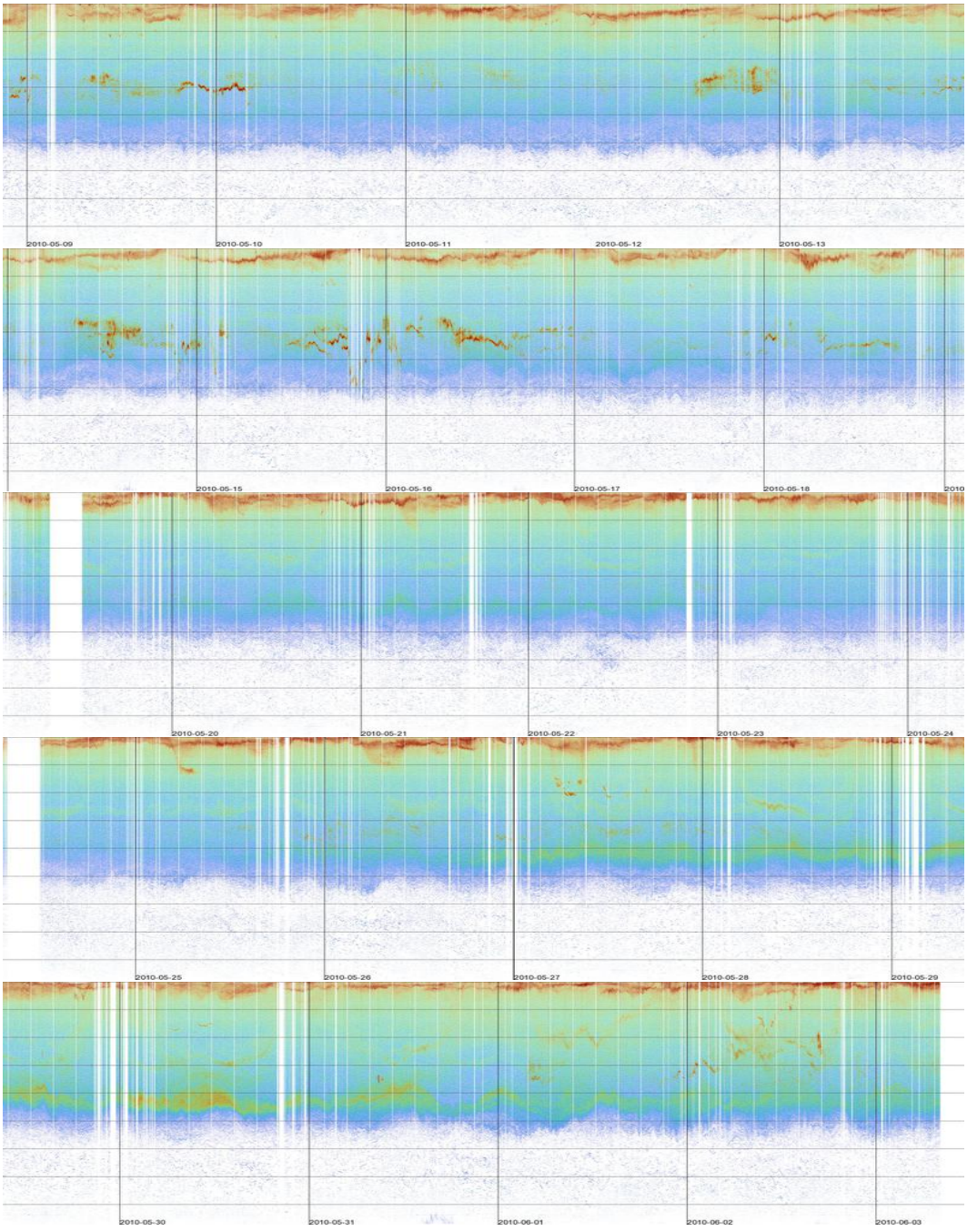
2010-05-09
2010-05-10
2010-05-11
2010-05-12
2010-05-13
2010-05-15
2010-05-16
2010-05-17
2010-05-18
2010-05-20
2010-05-21
2010-05-22
2010-05-23
2010-05-24
2010-05-25
2010-05-26
2010-05-27
2010-05-28
2010-05-29
2010-05-30
2010-05-31
2010-06-01
2010-06-02
2010-06-03

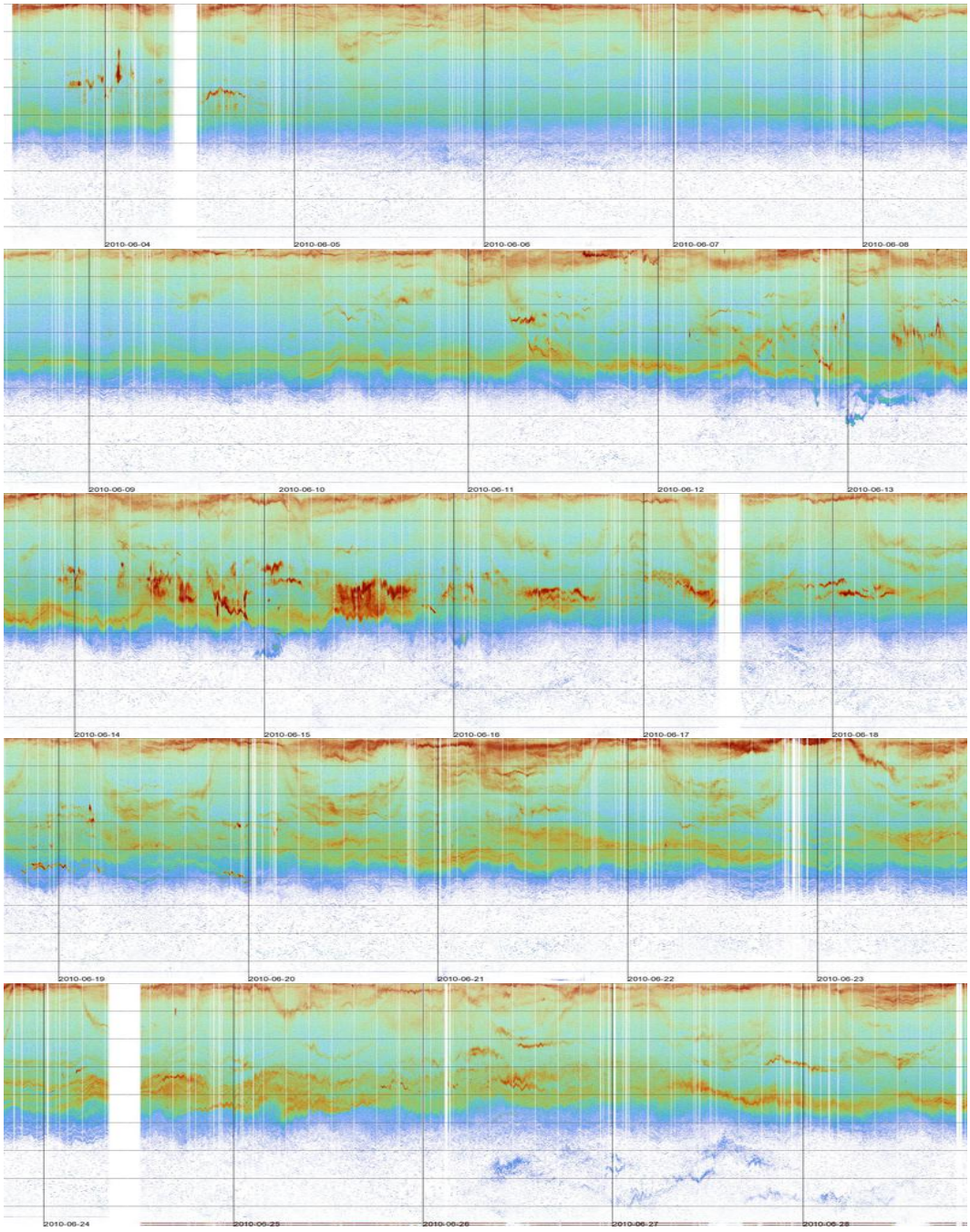
2010-06-04
2010-06-05
2010-06-06
2010-06-07
2010-06-08
2010-06-09
2010-06-10
2010-06-11
2010-06-12
2010-06-13
2010-06-14
2010-06-15
2010-06-16
2010-06-17
2010-06-18
2010-06-19
2010-06-20
2010-06-21
2010-06-22
2010-06-23
2010-06-24
2010-06-25
2010-06-26
2010-06-27
2010-06-28

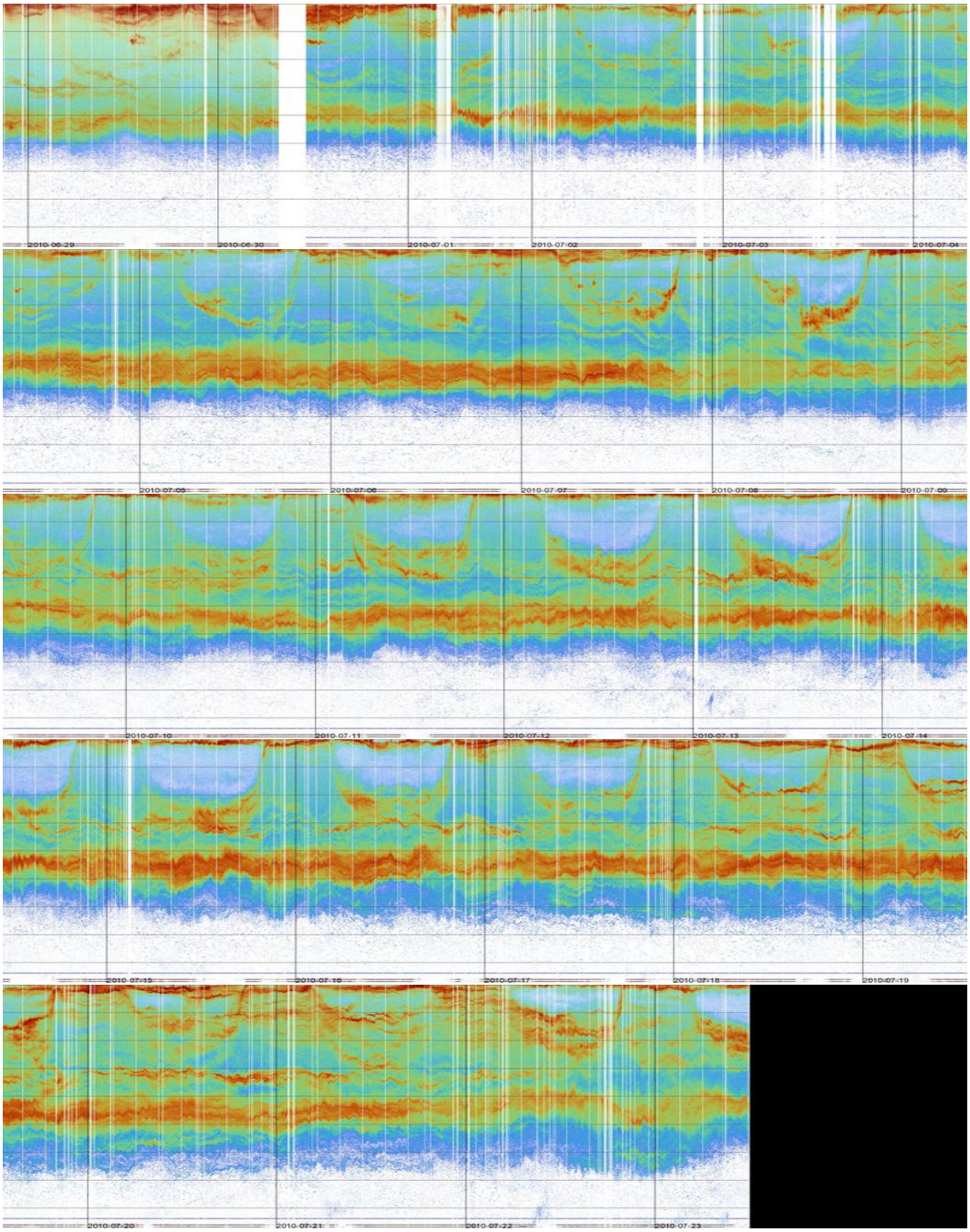

On 23 July 2010, burrowing rodents severed the shore side of MARS's cable, halting data collection until repairs were completed on 4 August.

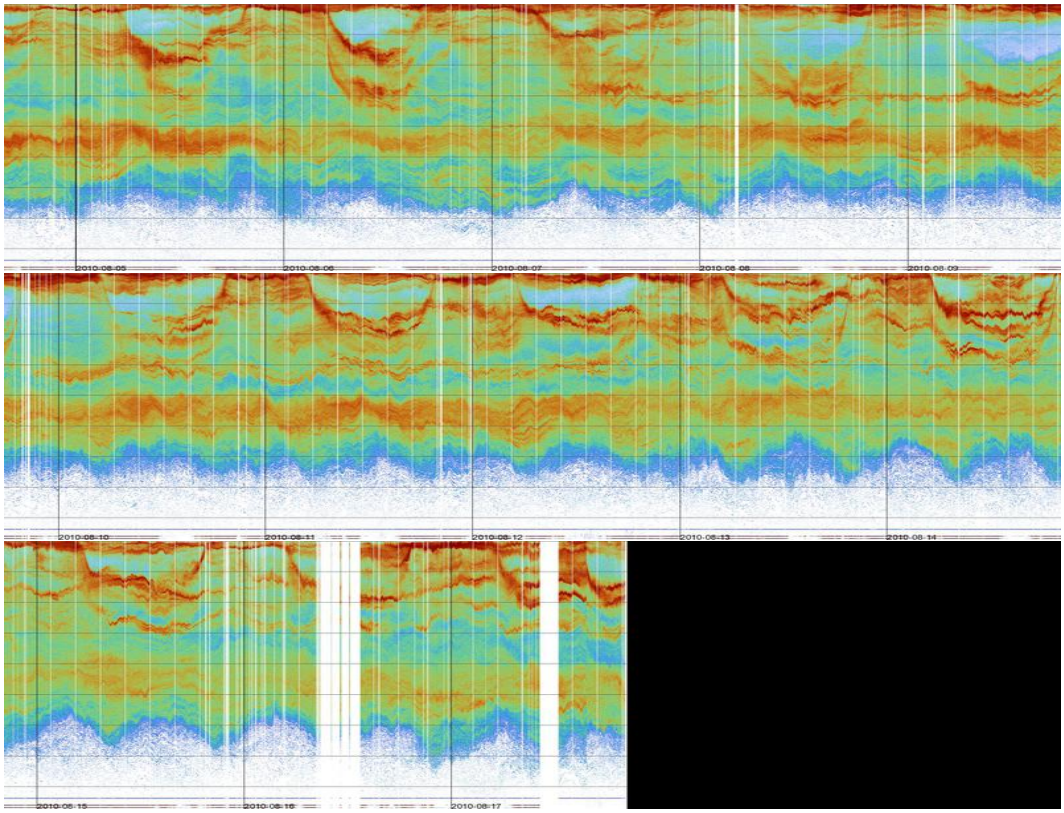

On 18 August 2010, at 11:12 Pacific Daylight Time, DEIMOS was shut down. A few minutes later, the ROV *Ventana* unplugged it from the MARS node, grasped it securely, and began to carry it back to the surface.

References

Akaike, H., 1974. A new look at the statistical model identification. *IEEE Transactions on Automatic Control* 19: 716–723.

Arrhenius, F., B. J. Benneheij, L. G. Rudstam, and D. Boisclair, 2000. Can stationary bottom split-beam hydroacoustics be used to measure fish swimming speed in situ? *Fisheries Research* 45: 31–41.

Bakun, A., 1973. Coastal upwelling indices: West Coast of North America 1946-95. Technical Report NMFS SSRF-693, U.S. Department of Commerce.

Barham, E., 1956. The ecology of sound scattering layers in the Monterey Bay area, California. Ph.D. thesis, Stanford University.

Barham, E., 1963. Siphonophores and the deep scattering layer. *Science* 140: 826–828.

Benoit-Bird, K. and W. Au, 2002. Energy: Converting from acoustic to biological resource units. *The Journal of the Acoustical Society of America* 111: 2070–2075.

Bergstad, O. A. and O.-R. Godø, 2003. The pilot project "Patterns and processes of the ecosystems of the northern Mid-Atlantic": aims, strategy and status. *Oceanologica Acta* 25: 219–226.

Bertrand, A., M. Ballón, and A. Chaigneau, 2010. Acoustic observation of living organisms reveals the upper limit of the oxygen minimum zone. *PLoS ONE* 5: e10330.

Bienfang, P. K., 1980. Phytoplankton sinking rates in oligotrophic waters off Hawaii, USA. *Marine Biology* 61: 69–77.

Bigelow, H. and M. Leslie, 1930. Reconnaissance of the waters and plankton of Monterey Bay, July 1928. *Bulletin of the Museum of Comparative Zoology* 70: 427–581.

Block, B. A., I. D. Jonsen, S. J. Jorgensen, A. J. Winship, S. A. Shaffer, S. J. Bograd, E. L. Hazen, D. G. Foley, G. A. Breed, A. L. Harrison, J. E. Ganong, A. Swithenbank, M. Castleton, H. Dewar, B. R. Mate, G. L. Shillinger, K. M. Schaefer, S. Benson, M. J. Weise, R. W. Henry, and D. P. Costa, 2011. Tracking apex marine predator movements in a dynamic ocean. *Nature* 475: 86–90.

Bolin, R. L. and D. P. Abbot, 1963. Studies on the marine climate and phytoplankton of the central coastal area of California, 1954-1960. *CalCOFI Reports* 9: 23–45.

Brinton, E. and A. Townsend, 2003. Decadal variability in abundances of the dominant euphausiid species in southern sectors of the California Current. *Deep-Sea Research II* 50: 2449–2472.

Brockwell, P. J. and R. A. Davis, 2002. Introduction to Time Series and Forecasting. Springer-Verlag, second edition.

Brodeur, R. and O. Yamamura, 2005. Micronekton of the North Pacific. *PICES Scientific Report* 30: 1–115.

Broenkow, W. and W. Smethie, 1978. Surface circulation and replacement of water in Monterey Bay. *Estuarine and Coastal Marine Science* 6: 583–590.

Cailliet, G., K. Karpov, and D. Ambrose, 1979. Pelagic assemblages as determined from purse seine and large midwater trawl catches in Monterey Bay and their affinities with the market squid *Loligo opalescens*. *CalCOFI Reports* 20: 21–30.

Čech, M. and J. Kubečka, 2002. Sinusoidal cycling swimming pattern of reservoir fishes. *Journal of Fish Biology* 61: 456–471.

Chan, F., J. Barth, J. Lubchenco, A. Kirincich, H. Weeks, W. Peterson, and B. Menge, 2008. Emergence of anoxia in the California Current Large Marine Ecosystem. *Science* 319: 920.

Chavez, F., J. Pennington, R. Herlien, H. Jannasch, G. Thurmond, and G. Friederich, 1997. Moorings and drifters for real-time interdisciplinary oceanography. *Journal of Atmospheric and Oceanic Technology* 14: 1199–1211.

Chelton, D. and D. Enfield, 1986. Ocean signals in tide guage records. *Journal of Geophysical Research* 91: 9081–9098.

Clarke, A. and M. Dottori, 2008. Planetary wave propagation off California and its effect on zooplankton. *Journal of Physical Oceanography* 38: 702–714.

Colebrook, J., 1977. Annual fluctuations in biomass of taxonomic groups of zooplankton in the California Current. *Fishery Bulletin* 75: 357–368.

Collins, C., J. Pennington, C. Castro, T. Rago, and F. P. Chavez, 2003. The California Current system off Monterey, California: physical and biological coupling. *Deep-Sea Research II* 50: 2389–2404.

Cooley, J. and J. Tukey, 1965. An algorithm for the machine calculation of complex Fourier series. *Mathematics of Computation* 19: 297–301.

Cornish, C., C. Bretherton, and D. B. Percival, 2006. Maximal overlap wavelet statistical analysis with application to atmospheric turbulence. *Boundary-Layer Meteorology* 119: 339–374.

Croll, D. A., B. B. Marinovic, S. Benson, and F. P. Chavez, 2005. From wind to whales: trophic links in a coastal upwelling system. *Marine Ecology Progress Series* 289: 117–130.

Daniell, P., 1946. Discussion on symposium on autocorrelation in time series. *Journal of the Royal Statistical Society, Series B* 8: 88–90.

De Robertis, A. and I. Higginbottom, 2007. A post-processing technique to estimate the signal-to-noise ratio and remove echosounder background noise. *ICES Journal of Marine Science* 64: 1282–1291.

Demer, D. and S. Conti, 2003. Validation of the stochastic distorted-wave Born approximation model with broad bandwidth total target strength measurements of Antarctic krill. *ICES Journal of Marine Science: Journal du Conseil* 60: 625–635.

Didrikas, T. and S. Hansson, 2008. Effects of light intensity on activity and pelagic dispersion of fish: studies with a seabed-mounted echosounder. *ICES Journal of Marine Science* 66: 388–395.

Dorman, J., S. Bollens, and A. Slaughter, 2005. Population biology of euphausiids off northern California and effects of short time-scale wind events on *Euphausia pacifica*. *Marine Ecology Progress Series* 288: 183–198.

Enfield, D. and J. Allen, 1980. On the structure and dynamics of monthly mean sea level anomalies along the Pacific coast of North and South America. *Journal of Physical Oceanography* 10: 557–578.

Escribano, R., V. Marín, and C. Irribarren, 2000. Distribution of *Euphausia mucronata* at the upwelling area of Peninsula Mejillones, northern Chile: the influence of the oxygen minimum layer. *Scientia Marina* 64: 69–77.

Field, J., K. Baltz, A. Phillips, and W. Walker, 2007. Range expansion and trophic interactions of the jumbo squid, *Dosidicus gigas*, in the California Current. *CalCOFI Reports* 48: 131 pp.

Fields, W. G., 1965. The structure, development, food relations, reproduction, and life history of the squid *Loligo opalescens* Berry. *Fishery Bulletin* 131: 108 pp.

Flagg, C., C. Wirick, and S. Smith, 1994. The interaction of phytoplankton, zooplankton and currents from 15 months of continuous data in the Mid-Atlantic Bight. *Deep-Sea Research II* 41: 411–435.

Foote, K. G., 1983. Linearity of fisheries acoustics, with addition theorems. *The Journal of the Acoustical Society of America* 73: 1932–1940.

Foote, K. G., H. Knudsen, G. Vestnes, D. N. MacLennan, and E. J. Simmonds, 1987. Calibration of acoustic instruments for fish density estimation: a practical guide. ICES Cooperative Research Report 144, International Council for the Exploration of the Sea.

Fowler, S. and L. Small, 1972. Sinking rates of euphausiid fecal pellets. *Limnology and Oceanography* pp. 293–296.

Gaston, K. J. and B. H. McArdle, 1994. The temporal variability of animal abundances: Measures, methods and patterns. *Philosophical Transactions of the Royal Society B* 345: 335–358.

Godø, O.-R., A. Samuelsen, G. J. Macaulay, R. Patel, S. S. Hjøllo, J. K. Horne, S. Kaartvedt, and J. A. Johannessen, 2012. Mesoscale eddies are oases for higher trophic marine life. *PLoS ONE* 7: e30161.

Goupillaud, P., A. Grossman, and J. Morlet, 1984. Cycle-octave and related transforms in seismic signal analysis. *Geoexploration* 23: 85–102.

Graham, W., J. Field, and D. Potts, 1992. Persistent "upwelling shadows" and their influence on zooplankton distributions. *Marine Biology* 114: 561–570.

Haury, L. R., J. A. McGowan, and P. H. Wiebe, 1978. Patterns and processes in the time-space scales of plankton distributions. In J. Steele, ed., *Spatial Pattern in Plankton Communities*, pp. 277–327. Plenum Press.

Holling, C. S., 1992. Cross-scale morphology, geometry, and dynamics of ecosystems. *Ecological Monographs* 62: 447–502.

Horne, J. K., 2000. Acoustic approaches to remote species identification: a review. *Fisheries Oceanography* 9: 356–371.

Horne, J. K. and C. Clay, 1998. Sonar systems and aquatic organisms: matching equipment and model parameters. *Canadian Journal of Fisheries and Aquatic Sciences* 55: 1296–1306.

Horne, J. K. and D. C. Schneider, 1994. Analysis of scale-dependent processes with dimensionless ratios. *Oikos* 70: 201–211.

Horne, J. K. and D. C. Schneider, 1995. Spatial variance in ecology. *Oikos* 74: 18–26.

Horne, J. K., S. S. Urmy, and D. H. Barbee, 2010. Using sonar to describe temporal patterns of oceanic organisms from the MARS Observatory. *OCEANS 2010* pp. 1–7.

Hosking, J., 1981. Fractional differencing. *Biometrika* 68: 165.

Huntley, M., A. Gonzalez, Y. Zhu, M. Zhou, and X. Irigoien, 2000. Zooplankton dynamics in a mesoscale eddy-jet system off California. *Marine Ecology Progress Series* 201: 165–178.

Huntley, M. E. and M. Lopez, 1992. Temperature-dependent production of marine copepods: a global synthesis. *The American Naturalist* 140: 201–242.

Hurvich, C. and C. Tsai, 1989. Regression and time series model selection in small samples. *Biometrika* 76: 297–307.

Huyer, A., 1983. Coastal upwelling in the California Current system. *Progress in Oceanography* 12: 259–284.

Jahncke, J., B. Saenz, C. Abraham, C. Rintoul, R. Bradley, and W. Sydeman, 2008. Ecosystem responses to short-term climate variability in the Gulf of the Farallones, California. *Progress in Oceanography* 77: 182–193.

Jones, E., T. Oliphant, P. Peterson, et al., 2001–2012. SciPy: Open source scientific tools for Python. http://www.scipy.org/.

Jones, R., 1980. Maximum likelihood fitting of ARMA models to time series with missing observations. *Technometrics* 22: 389–395.

Jurvelius, J. and T. Marjomaeki, 2004. Vertical distribution and swimming speed of pelagic fishes in winter and summer monitored in situ by acoustic target tracking. *Boreal Environment Research* 9: 277–284.

Kaartvedt, S., A. Røstad, T. A. Klevjer, and A. Staby, 2009. Use of bottom-mounted echo sounders in exploring behavior of mesopelagic fishes. *Marine Ecology Progress Series* 395: 109–118.

Kaiser, G., 1994. A Friendly Guide to Wavelets. Birkhauser.

Kalish, J., C. F. Greenlaw, W. G. Pearcy, and D. V. Holliday, 1986. The biological and acoustical structure of sound scattering layers off Oregon. *Deep-Sea Research I* 33: 631–653.

Kaltenberg, A. M., R. Emmett, and K. J. Benoit-Bird, 2010. Timing of forage fish seasonal appearance in the Columbia River plume and link to ocean conditions. *Marine Ecology Progress Series* 419: 171–184.

Keister, J. E. and P. T. Strub, 2008. Spatial and interannual variability in mesoscale circulation in the northern California Current System. *Journal of Geophysical Research* 113: C04015.

Keitt, T. H., 2008. Coherent ecological dynamics induced by large-scale disturbance. *Nature* 454: 331–334.

Lavaniegos, B. and M. Ohman, 2003. Long-term changes in pelagic tunicates of the California Current. *Deep-Sea Research I* 50: 2473–2498.

Lavaniegos, B. and M. Ohman, 2007. Coherence of long-term variations of zooplankton in two sectors of the California Current System. *Progress in Oceanography* 75: 42–69.

Legaard, K. R. and A. C. Thomas, 2008. Spatial patterns of intraseasonal variability of chlorophyll and sea surface temperature in the California Current. *Journal of Geophysical Research* 112: C09006.

Liang, X. S. and A. R. Robinson, 2009. Multiscale processes and nonlinear dynamics of the circulation and upwelling events off Monterey Bay. *Journal of Physical Oceanography* 39: 290–313.

Ljung, G. and G. Box, 1978. On a measure of lack of fit in time series models. *Biometrika* 65: 297–303.

Lyman, J. M. and G. C. Johnson, 2008. Equatorial Kelvin wave influences may reach the Bering Sea during 2002 to 2005. *Geophysical Research Letters* 35: L14607.

Lynn, R. J., K. A. Bliss, and L. E. Eber, 1982. Vertical and horizontal distributions of seasonal mean temperature, salinity, sigma-t, stability, dynamic height, oxygen and oxygen saturation in the California Current, 1950–1978. *CalCOFI Atlas* 30: 513 pp.

MacLennan, D. N., P. G. Fernandes, and J. Dalen, 2002. A consistent approach to definitions and symbols in fisheries acoustics. *ICES Journal of Marine Science* 59: 365–369.

Maraun, D. and J. Kurths, 2004. Cross wavelet analysis: significance testing and pitfalls. *Nonlinear Processes in Geophysics* 11: 505–514.

Marinovic, B. B., D. A. Croll, N. Gong, S. Benson, and F. P. Chavez, 2002. Effects of the 1997–1999 El Niño and La Niña events on zooplankton abundance and

euphausiid community composition within the Monterey Bay coastal upwelling system. *Progress in Oceanography* 54: 265–277.

McGowan, J., S. J. Bograd, R. J. Lynn, and A. Miller, 2003. The biological response to the 1977 regime shift in the California Current. *Deep-Sea Research II* 50: 2567–2582.

McManus, M., O. Cheriton, P. Drake, D. V. Holliday, C. Storlazzi, P. Donaghay, and C. F. Greenlaw, 2005. Effects of physical processes on structure and transport of thin zooplankton layers in the coastal ocean. *Marine Ecology Progress Series* 301: 199–215.

Mehner, T., 2006. Individual variability of diel vertical migrations in European vendace (*Coregonus albula*) explored by stationary vertical hydroacoustics. *Ecology of Freshwater Fish* 15: 146–153.

Ménard, F., F. Marsac, E. Bellier, and B. Cazelles, 2007. Climatic oscillations and tuna catch rates in the Indian Ocean: a wavelet approach to time series analysis. *Fisheries Oceanography* 16: 95–104.

Micheli, F., K. Cottingham, J. Bascompte, G. Eckert, J. Fischer, T. H. Keitt, B. Kendall, J. Klug, and J. Rusak, 1999. The dual nature of community variability. *Oikos* 85: 161–169.

Münchow, A., 2000. Wind stress curl forcing of the coastal ocean near Point Conception, California. *Journal of Physical Oceanography* 30: 1265–1280.

Omori, M. and D. Gluck, 1979. Life history and vertical migration of the pelagic shrimp *Sergestes similis* off the Southern California coast. *Fishery Bulletin* 77: 183–198.

Osgood, K. and D. M. Checkley, 1997. Seasonal variations in a deep aggregation of *Calanus pacificus* in the Santa Barbara Basin. *Marine Ecology Progress Series* 148: 59–69.

Pauly, D. and V. Christensen, 1995. Primary production required to sustain global fisheries. *Nature* 374: 255–257.

Paxton, J., 1967. A distributional analysis for the lanternfishes (family Myctophidae) of the San Pedro Basin, California. *Copeia* 1967: 422–440.

Pearcy, W. and C. Forss, 1969. The oceanic shrimp *Sergestes similis* off the Oregon coast. *Limnology and Oceanography* pp. 755–765.

Pennington, J. T. and F. P. Chavez, 2000. Seasonal fluctuations of temperature, salinity, nitrate, chlorophyll and primary production at station H3/M1 over 1989-1996 in Monterey Bay, California. *Deep-Sea Research II* 47: 947–973.

Percival, D. B., D. A. Rothrock, A. S. Thorndike, and T. Gneiting, 2008. The variance of mean sea-ice thickness: Effect of long-range dependence. *Journal of Geophysical Research* 113: C01004.

Phillips, A. J., R. D. Brodeur, and A. V. Suntsov, 2009. Micronekton community structure in the epipelagic zone of the northern California Current upwelling system. *Progress in Oceanography* 80: 74–92.

Pilskaln, C., C. Lehmann, J. Paduan, and M. Silver, 1998. Spatial and temporal dynamics in marine aggregate abundance, sinking rate and flux: Monterey Bay, central California. *Deep-Sea Research II* 45: 1803–1837.

Prchalová, M., V. Drastík, J. Kubečka, B. Sricharoendham, F. Schiemer, and J. Vijverberg, 2003. Acoustic study of fish and invertebrate behavior in a tropical reservoir. *Aquatic Living Resources* 16: 325–332.

Rebstock, G., 2003. Long-term change and stability in the California Current System: lessons from CalCOFI and other long-term data sets. *Deep-Sea Research II* 50: 2583–2594.

Robison, B. H., 2004. Deep pelagic biology. *Journal of Experimental Marine Biology and Ecology* 300: 253–272.

Robison, B. H., 2005. Giant larvacean houses: Rapid carbon transport to the deep sea floor. *Science* 308: 1609–1611.

Robison, B. H. and T. G. Bailey, 1981. Sinking rates and dissolution of midwater fish fecal matter. *Marine Biology* 65: 135–142.

Robison, B. H., K. R. Reisenbichler, R. E. Sherlock, J. M. Silguero, and F. P. Chavez, 1998. Seasonal abundance of the siphonophore, *Nanomia bijuga*, in Monterey Bay. *Deep-Sea Research II* 45: 1741–1751.

Robison, B. H., R. E. Sherlock, and K. R. Reisenbichler, 2010. The bathypelagic community of Monterey Canyon. *Deep-Sea Research II* 57: 1551–1556.

Rosenfeld, L., F. B. Schwing, N. Garfield, and D. Tracy, 1994. Bifurcated flow from an upwelling center: a cold water source for Monterey Bay. *Continental Shelf Research* 14: 931–964.

Ryan, J. P., F. P. Chavez, and J. Bellingham, 2005. Physical-biological coupling in Monterey Bay, California: topographic influences on phytoplankton ecology. *Marine Ecology Progress Series* 287: 23–32.

Schneider, D. C., 2009. Quantitative Ecology, chapter 11, pp. 211–224. Academic Press, second edition.

Schrader, G. C., 1981. Seasonal cycles of phytoplankton in relation to the hydrography of Monterey Bay. Moss Landing Marine Labratories Technical Publication 2, Moss Landing Marine Laboratories.

Schwing, F. B., M. O'Farrell, J. M. Steger, and K. Baltz, 1996. Coastal upwelling indices: West Coast of North America 1946-95. NOAA Technichal Memorandum NOAA-TM-NMFS-SWFSC-231, U.S. Department of Commerce.

Service, S., J. Rice, and F. P. Chavez, 1998. Relationship between physical and biological variables during the upwelling period in Monterey Bay, CA. *Deep-Sea Research II* 45: 1669–1685.

Simmonds, E. J. and R. Fryer, 1996. Which are better, random or systematic acoustic surveys? A simulation using North Sea herring as an example. *ICES Journal of Marine Science* 53: 39–50.

Skogsberg, T., 1936. Hydrography of Monterey Bay, California. Thermal conditions, 1929-1933. *Transactions of the American Philosophical Society* 29: i–152.

Skogsberg, T. and A. Phelps, 1946. Hydrography of Monterey Bay, California. Thermal conditions, part II (1934-1937). *Proceedings of the American Philosophical Society* 90: 350–386.

Smith, S. and P. Adams, 1988. Daytime surface swarms of *Thysanoessa spinifera* (Euphausiacea) in the Gulf of the Farallones, California. *Bulletin of Marine Science* 42: 76–84.

Stanton, T. K., D. Chu, and P. H. Wiebe, 1996. Acoustic scattering characteristics of several zooplankton groups. *ICES Journal of Marine Science* 53: 289–295.

Steele, J. H., 1978. Some comments on plankton patches. In J. H. Steele, ed., *Spatial Pattern in Plankton Communities*, pp. 1–21. Plenum Press.

Stommel, H., 1963. Varieties of oceanographic experience. *Science* 139: 572–576.

Torrence, C. and G. Compo, 1998. A practical guide to wavelet analysis. *Bulletin of the American Meteorological Society* 79: 61–78.

Trevorrow, M., 2005. The use of moored inverted echo sounders for monitoring meso-zooplankton and fish near the ocean surface. *Canadian Journal of Fisheries and Aquatic Sciences* 62: 1004–1018.

Wilson, C. and M. Guttormsen, 1997. Echo integration-trawl survey of Pacific whiting, *Merluccius productus*, off the west coasts of the United States and Canada during July-September 1995. NOAA Technical Memorandum NMFS-AFSC-74, U.S. Department of Commerce.

Wilson, J. A., 2006. Matching social and ecological systems in complex ocean fisheries. *Ecology and Society* 11.

Yeh, J. and J. Drazen, 2011. Baited-camera observations of deep-sea megafaunal scavenger ecology on the California slope. *Marine Ecology Progress Series* 424: 145–156.